One-dimensional turbomachinery models for pumped thermal energy storage systems

Akhilesh Singhal

Delft University of Technology

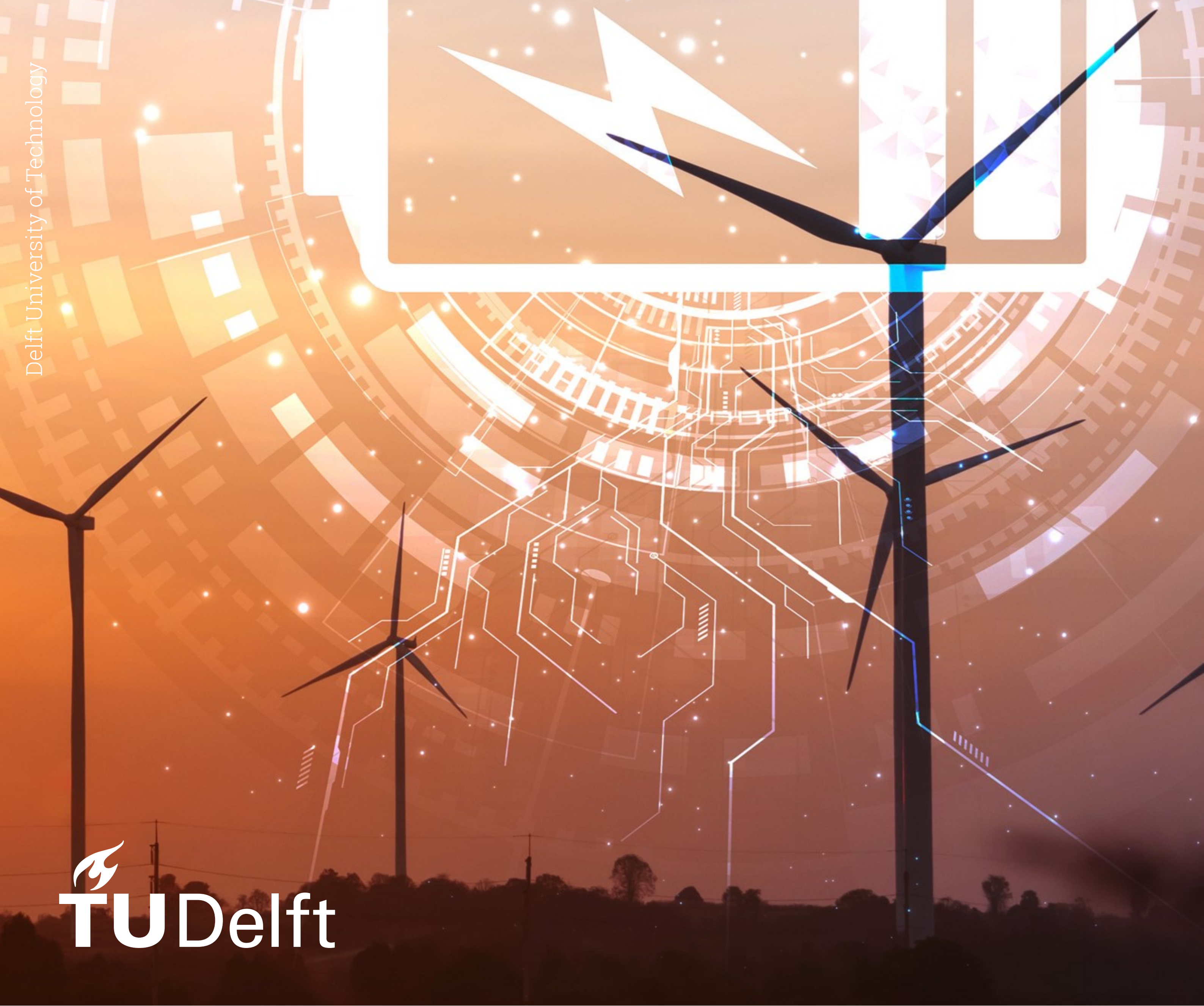

One-dimensional turbomachinery models for pumped thermal energy storage systems

by

Akhilesh Singhal

to obtain the degree of Master of Science
at the Delft University of Technology,
to be defended publicly on Tuesday October 24, 2023 at 3:00 PM.

Student number:	5549345	
Project duration:	November 2, 2022 – October 24, 2023	
Thesis committee:	Prof. dr. ir. Sikke Klein,	TU Delft, Supervisor
	Prof. dr. ir. Rene Pecnik,	TU Delft, Supervisor
	Prof. dr. ir. Kamel Hooman,	TU Delft, Committee
	Prof. dr. ir. Carlo de Servi,	TU Delft, Committee

An electronic version of this thesis is available at `http://repository.tudelft.nl/`.

Abstract

The rise in temperature attributed to human CO2 emissions and the escalating energy needs of society necessitates the development of clean energy production. Solar and wind energy, both renewable sources, have emerged as cost-effective alternatives to conventional fossil fuel systems. They now account for a substantial portion of the world's electricity generation [1]. However, their intermittent nature poses a challenge to their reliability. To overcome this, the implementation of grid-scale energy storage systems is crucial. Such systems can store excess energy produced during peak periods and release it during low-generation or high-demand periods, ensuring a stable and dependable power supply to the grid.

Pumped Thermal Energy Storage (PTES) is one such type of promising grid-scale storage solution based on the concept of storing electricity in the form of heat. These systems are not reliant on rare earth metals, are not restricted by geographical location, and are relatively economical over their lifetime. They employ a heat pump cycle for charging and a heat engine cycle during times of discharge. Often, in the thermodynamic modelling of PTES systems, a fixed value of turbomachinery efficiency is assumed. This approach holds well for the first estimate of performance, but for better accuracy and further analysis, meanline models could be used to arrive at the efficiency value and preliminary geometric design. Hence, this work presents a method for developing meanline models for centrifugal compressors and radial inflow turbines. Modelling techniques and guidelines from the literature are noted and presented here. The accuracy of these models is dependent mainly on the loss models used. Using suitable models selected from the literature, a fair agreement was found between the meanline model's prediction and experimental data from open literature, validating the methodology.

An essential function of energy storage is to provide load flexibility, meaning its charging and discharging cycles must adjust to match the net load curve. As a result, the turbomachinery would need to operate under off-design conditions to meet these demands. Therefore, this report introduces an approach to extend the PTES model by Radi [2] for off-design operation based on turbomachine performance.

Finally, a preliminary design for a 100 kW scale PTES system is performed, and the off-design response of this PTES system during charging and discharging cycles is examined in conjunction with the turbomachinery meanline models.

Acknowledgment

Over the past two years at TU Delft, my time has been profoundly enriching, pushing me beyond my familiar boundaries and into vibrant learning experiences. As I conclude this chapter of my journey at TU Delft, I reflect upon the myriad of experiences, learnings, and challenges it has brought me.

First and foremost, I am indebted to my supervisors, Prof. Sikke Klein and Prof. Rene Pecnik. Their insights and guidance played an invaluable role in refining the problem statement and critically analysing this thesis, enabling me to deliver quality work. They always stood beside me to check on my progress and nudge me along the right path.

I am grateful to Prof. Matteo Pini for always being approachable and available to discuss my queries regarding the aspects of turbomachinery design. I would also like to express my thanks to Matteo Majer, Evert Bunschoten and Andrea Giuffree for lending their patient ear and for their helpful discussions and advice. Moreover, I would like to extend my sincere regards to Prof. Kamel Hooman and Prof. Carlo de Servi for being a part of my thesis committee and evaluating my work.

Ali, my thesis sparring partner, thanks for being an excellent sounding board and for all those constructive discussions on energy storage. To everyone in the PE flex room, I will miss our deep technical debates and silly banter over coffee. You made this thesis journey unforgettable. To all who made my time at Delft special, I hope I reciprocated your friendship.

Special thanks to my family for standing by me through the highs and lows as I pursued this demanding degree. Your calls, advice (both solicited and unsolicited), and blessings have been the pillars of strength.

Akhilesh Singhal
October, 2023

Contents

Abstract ii

Acknowledgment iv

Nomenclature xii

1 Introduction 1
- 1.1 Types of energy storage 2
- 1.2 Thesis outline 3

2 Pumped Thermal Energy Storage 5
- 2.1 PTES 5
  - 2.1.1 Brayton PTES 5
  - 2.1.2 Rankine cycles 7

3 Turbomachinery for PTES systems 11
- 3.1 Types of compressor and expanders 11
- 3.2 Terms related to turbomachinery 12
- 3.3 Similitude theory and preliminary selection 12
- 3.4 Turbomachinery type for 100 kW PTES system 15
- 3.5 Turbomachinery models for PTES 15
- 3.6 Thesis objectives 17

4 Centrifugal compressor model 19
- 4.1 Compressor stations 20
- 4.2 Velocity triangles 20
  - 4.2.1 Work done in centrifugal compressors 22
- 4.3 Performance range 22
- 4.4 Meanline model for centrifugal compressors 24
  - 4.4.1 Meanline models in literature 24
- 4.5 Loss models 25
  - 4.5.1 Internal Loss models 26
  - 4.5.2 External loss models 29
- 4.6 Off design model 29
  - 4.6.1 Impeller inlet 30
  - 4.6.2 Impeller outlet 30
  - 4.6.3 Vaneless diffuser section 31
  - 4.6.4 Model validation 33
- 4.7 Compressor meanline design model 37
  - 4.7.1 Design of inlet section 37
  - 4.7.2 Design of the rotor outlet 37
  - 4.7.3 Design of the vaneless diffuser 40

5 Radial inflow turbine 43
- 5.1 Turbine stations 43
- 5.2 Velocity triangles 44

5.3 Turbine performance characteristics . . . 45
5.4 Meanline models in literature . . . 45
5.5 Loss models . . . 47
    5.5.1 Rotor loss models . . . 47
    5.5.2 Stator loss models . . . 50
5.6 Off design model . . . 50
    5.6.1 Nozzle section . . . 50
    5.6.2 Interspace region . . . 51
    5.6.3 Rotor section . . . 52
5.7 Validation case . . . 52
5.8 Turbine meanline design model . . . 55
    5.8.1 Rotor design . . . 56
    5.8.2 Stator design . . . 57

6 Design case for 100kW PTES system 59
6.1 PTES system design . . . 59
6.2 Turbomachinery for 100 kW case . . . 59
6.3 Compressor section . . . 60
    6.3.1 Compressor design . . . 60
    6.3.2 Compressor performance . . . 61
6.4 Turbine section . . . 62
    6.4.1 Turbine design . . . 62
    6.4.2 Turbine performance . . . 64
6.5 Off design characteristics of the PTES system . . . 65
    6.5.1 PTES charging . . . 65
    6.5.2 PTES discharging . . . 69
    6.5.3 PTES round trip efficiency . . . 70

7 Conclusions and Recommendations 73
7.1 Conclusions . . . 73
7.2 Recommendations . . . 74
    7.2.1 Compressor model . . . 74
    7.2.2 Turbine model . . . 74
    7.2.3 PTES Model . . . 74

References 76

A Data used for validation cases 81
A.1 Compressor Validation . . . 81
A.2 Turbine Validation . . . 82

B Steps to derive a relation for the compressor rotor blade angle 83

C Discrepancies in literature 85
C.1 Compressor meanline model . . . 85
C.2 Turbine meanline model . . . 85

List of Figures

1.1 Supply and demand curve showing the role of storage balancing renewable energy supply [5]. 2
1.2 Grid scale storage installations as of 2021, and future targets for a net zero scenario [6]. 2

2.1 Schematic of a PTES system with a hot store, and with the ambient as the low-temperature heat source [11]. 6
2.2 T-s diagram showing Brayton, Rankine and transcritical cycles [12]. 6
2.3 Brayton-based PTES systems as proposed by Isentropic Ltd. and Saipem [14]. 7
2.4 Rankine based PTES system [15]. 7
2.5 Charging and discharging cycles with subcritical (left) and transcritical Rankine cycles (right) [11]. 8
2.6 CHEST concept with waste heat integration provided by a low-temperature external heat source to reduce compression work during the charging process [9]. 8
2.7 PTES systems configurations examined by Gautam [10]. 10

3.1 Types of commercially available machines for PTES systems[15]. 11
3.2 Selection process for turbomachinery [15]. 12
3.3 Baljé diagram for single stage compressor [27]. 13
3.4 Baljé diagram for single stage turbine [27]. 14
3.5 Selection diagrams for turbomachines [22]. 14

4.1 A centrifugal compressor [23]. 19
4.2 Compressor stations naming conventions for this thesis. 20
4.3 Velocity triangles at impeller inlet and exit [23]. 21
4.4 Velocity triangle at impeller exit showing the effect of slip [23]. Here β_{2B} represents the blade angle at the rotor exit, and $c_{2u,\infty}$ denotes the tangential component of the velocity without slip. 21
4.5 Mollier diagram of a typical compressor. Points 1, 2 and 3 refer to the impeller inlet, impeller outlet and diffuser outlet respectively [22]. 23
4.6 Typical performance map for a compressor [22]. 23
4.7 Variation of critical flow angle with diffuser width [47]. 24
4.8 Skin friction correlation [23, 46]. 28
4.9 Compressor off-design calculation procedure. 30
4.10 Evaluation of static properties at impeller inlet. 30
4.11 Evaluation of properties at impeller outlet. 31
4.12 Comparison of meanline model vs experimental data of the Eckardt 'O' impeller 35
4.13 Comparison of meanline model vs experimental data of the Schiffmann impeller 36
4.14 Compressor meanline design procedure. 37
4.15 Variation of inlet tip Mach number vs meridional velocity. The red dot shows the selection point for minimisation. 38
4.16 Design procedure for compressor inlet. 38

4.17 Design procedure for compressor outlet. 39
4.18 β_{2b} values for $\eta_{tt} = 80$% and N_b= 22. 40

5.1 Radial inflow turbine [23]. 43
5.2 Radial inflow turbine stations and naming convention for this thesis. 44
5.3 Velocity triangles at rotor inlet and outlet [23]. Here, subscripts 1 and 2 refer to the rotor inlet and exit, respectively 44
5.4 Mollier diagram for radial infow turbines [23]. 45
5.5 Performance map of a high speed turbine [22]. 46
5.6 Rotor losses in a radial turbine [23]. 47
5.7 Optimal inflow conditions at the rotor inlet (”p” denotes the pressure surface, and ”s” represents the suction surface) [22]. 48
5.8 Turbine off-design flowchart. 50
5.9 Evaluation of thermodynamic properties in the nozzle section 51
5.10 Evaluation of properties in the interspace region. 52
5.11 Evaluation of properties at rotor exit. 53
5.12 Comparison of meanline model vs experimental data of the McLallin turbine. In the graphs, the design speed is 33262 rpm. 54
5.13 Flowchart for turbine design. 55
5.14 Flowchart for turbine rotor design. 56
5.15 Flowchart for turbine stator design. 57

6.1 PTES cycle based on inputs from table 6.1 with R1233zd(E) as the working fluid. 60
6.2 Specific speed versus the number of stages for the turbine based on inputs from table 6.1. The shaded areas represent the optimal range of specific speeds. . 60
6.3 Performance charts for a two-stage compressor configuration. The surge points for the first and second stages are marked by squares and diamonds. The rotating stall points are shown as triangles and stars for the first and second stages, respectively 63
6.4 Performance charts for a two-stage turbine configuration. 66
6.5 Charging cycle behaviour for varied compressor pressure ratios. 67
6.6 Charging cycle behaviour for varied compressor efficiencies. 67
6.7 Variation of compressor pressure ratio and efficiency on the COP. 68
6.8 Compressor outlet temperature and COP for varying mass flow cases. The solid lines represent the compressor outlet temperature, and the dashed line represents the COP. Also, the squares and diamonds represent the surge points for compressor stages 1 and 2, respectively. The circles represent the optimal operating point for each speed, and the crosses mark the corresponding COP. 68
6.9 Compressor power vs COP 69
6.10 Discharging cycle behaviour for varied turbine pressure ratios 70
6.11 Discharging cycle behaviour for varied turbine pressure ratios. 70
6.12 Dependence of the heat engine efficiency on the turbine mass flow rate. 71
6.13 Turbine power vs η_{HE}. 71
6.14 Variation of round trip efficiency for different charging and discharging power scenarios. 72

B.1 Parametric analysis rotor blade angle according to equation B.11. 84

List of Tables

1.1 Comparison of types of grid scale storage technologies [7, 10]. 3

3.1 Turbomachinery specific speed ranges for high efficiency [23]. 14

4.1 Validation cases for centrifugal compressor. 33
4.2 Tuning parameters used for the validation cases. 33
4.3 Input parameters for centrifugal compressor [23]. 37

5.1 Recommended range for input parameters for the radial inflow turbine [23, 78]. 55

6.1 PTES model inputs and results using R1233zd(E) as a working fluid. 59
6.2 Preliminary turbomachinery selection results based on specific speed. 61
6.3 Design variables for the compressor design 61
6.4 Results for compressor design. 62
6.5 Design variables for the turbine design 64
6.6 Results for turbine design. 65

A.1 Data of centrifugal compressors for validation cases. 81
A.2 Turbine data used for validation cases 82

Nomenclature

Abbreviations

1D	One Dimensional
CAES	Compressed Air Energy Storage
CFD	Computational Fluid Dynamics
CHEST	Compressed Heat Energy Storage
COP	Coefficient of Performance
DLR	German Aerospace Center
HE	Heat Engine
HP	Heat Pump
IEA	International Energy Agency
ORC	Organic Rankine cycles
PCM	Phase Change Material
PSH	Pumped Storage Hydropower
PTES	Pumped Thermal Energy Storage
RTE	Round Trip Efficiency
RIT	Radial Inflow Turbine
TES	Thermo-Electric Storage

Greek Letters

Ω	Rotational Speed
ψ	Work Coefficient
α	Absolute flow angle
β	Relative flow angle, pressure ratio
Π	Pressure ratio
ρ	Density
γ	Heat capacity ratio
η	Efficiency
Φ	Flow factor
Ψ	Work Factor
ϵ,τ	Clearance
ϕ	Flow Coefficient
ω	Angular velocity
ω_s	Specific Speed
ε	Wake fraction
ξ	Meridional velocity ratio
σ	Slip Factor
μ	Dynamic Viscosity

Symbols

Z	Number of blades
u	Peripheral speed
c	Absolute velocity
w	Relative velocity
P	Pressure, Power
Re	Reynolds number
Ma	Mach number
h	Enthalpy
s	Entropy
T	Temperature
r	Radius
L	Length
D	Diameter
A	Area
b	Width
I	Rothalpy
W	Work
Q	Heat
$\dot{m}$	Mass flowrate
t	Thickness
N_b	Number of Blades
k_s	Roughness
c_f	Friction Factor

Subscripts

0	Total conditions
is	Isentropic
θ	tangential
tr	Total relative
t	Tip, tangential
tt	Total-to-total
ts	Total-to-static
ss	Static-to-static
a	Axial
b	Backface, Blade
r	Radial
h	Hub
z	Axial direction
s	Shroud, Entropy
m	Meridional
opt	Optimal
hyd	Hydraulic
cl	Clearance

1

Introduction

As extreme weather events become more frequent and global temperature records are broken year after year, the critical need for immediate climate action and innovation has become increasingly apparent. To address the effects of human activity, the Paris Agreement was signed by 194 countries, with the aim of limiting the global temperature increase to 1.5°C. To achieve this goal, countries must reduce their carbon emissions by 43% by the year 2030 [3].

Power generation is responsible for a third of global carbon emissions [4]. Established renewable technologies, such as solar and wind, have the potential to significantly reduce these emissions by providing clean energy. As their costs decrease each year and are supported by favourable policies, their share in power generation capacity has more than doubled in the past decade, rising from 1157 GW in 2012 to 3258 GW in 2022 [1].

However, the intermittent nature of these technologies is a significant limitation. Reliance on weather patterns and other natural events often leads to a mismatch between power generation and consumption rates, which can threaten grid stability. This remains a bottleneck in the adoption of a fully renewable grid, particularly when compared to the reliable performance of conventional fossil fuel-based power plants.

To effectively integrate renewable energy, grid-scale storage systems are necessary to balance supply and demand. Figure 1.1 depicts the typical hourly variation of energy demand. Traditionally, base-load services are provided by nuclear and coal power plants, while load-following and peaking services are provided by natural gas and hydroelectric power plants. This figure further illustrates how energy storage and renewables can replicate this pattern. Hydropower can serve as a steady base load. While solar and wind are inherently variable, to match the demand curve (red), stored energy can be deployed (purple) and replenished during times of surplus production (orange).

A pivotal component for transitioning to a zero-carbon energy system is a storage solution that's scalable, efficient, and viable on a grid scale. According to the net zero scenarios outlined by IEA, grid-scale storage capacities would have to ramp up significantly from 16 GW in 2021 to 680 GW by 2030 [6]. The scale of these numbers is better appreciated by figure 1.2, highlighting the substantial effort required over the next seven years to remain on target.

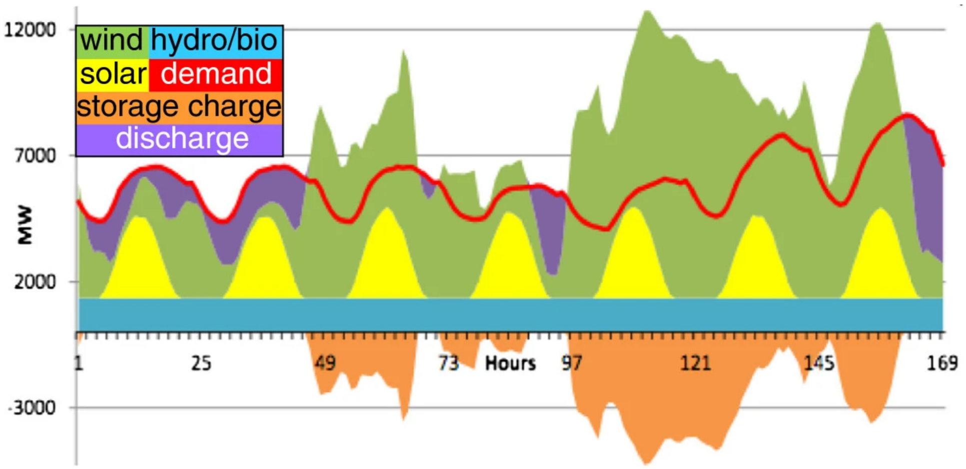

Figure 1.1: Supply and demand curve showing the role of storage balancing renewable energy supply [5].

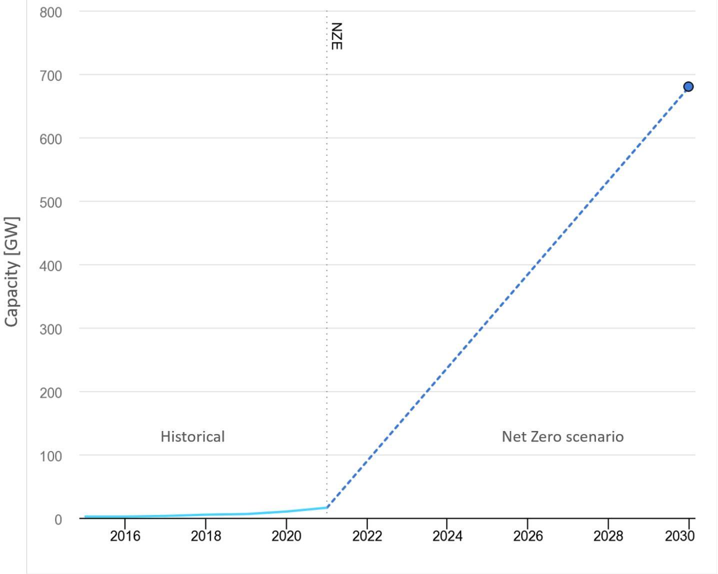

Figure 1.2: Grid scale storage installations as of 2021, and future targets for a net zero scenario [6].

1.1. Types of energy storage

Based on the findings of Bowden et al. [7], various types of energy storage can be classified as detailed in table 1.1. Pumped Storage Hydropower (PSH) systems have been a popular grid storage choice due to their strong round-trip efficiencies, economic feasibility, and technological maturity. However, their implementation is limited by geographic constraints. While Compressed Air Energy Storage (CAES) is an appealing option in terms of efficiency and cost, it too is limited by geography. Alternatively, Chemical and electrochemical technologies are geographically independent and score well across comparison metrics, despite being relatively costly. The main disadvantage of these technologies is their reliance on rare earth materials.

Thermal Energy Storage (TES) technologies have the capability to store energy for several hours, making them suitable for addressing daily peak capacity needs. Most importantly, they are not bound by geographical constraints nor require rare earth materials and are lower in cost compared to other grid-scale technology options, further enhancing their appeal. This technology works on the principle of storing excess energy in the form of heat during charging and extracting the heat at a later period during discharging. Pumped Thermal Energy Storage

(PTES) and Liquid Air Energy Storage (LAES) are two thermodynamic cycles to store electricity in the form of thermal energy, employing earth-abundant materials that are kept in large insulated tanks [8].

PTES, in particular, uses a heat pump to store electricity as heat in a thermal storage medium, which is later discharged using a heat engine. In addition, waste heat sources can be utilised to improve their operational efficiency [9]. These characteristics make PTES an attractive solution for addressing the intermittency issue posed by renewables. The following section will discuss the different types of PTES technologies in more detail.

Table 1.1: Comparison of types of grid scale storage technologies [7, 10].

Storage types	Mechanical		Chemical	Electro-chemical		Electro-thermal
Technology	PSH	CAES	H_2 production and fuel cells	Li-ion	Flow battery	TES
Development Stage	Commercialised	Initial commercialization	Pilot stage	Commercialised	Initial commercialization	Initial commercialization
Power output [MW]	100-5000	1-400	10^{-6} - 50	0.1-50	1-200	0.1-300
Power Cost [$/kW]	1504-2422	973-1259	2793-3488	1410-1950	2000-2440	1700-1800
Energy Cost [$/kWh]	150-242	97-126	279-349	350-490	500-610	20-60
Discharge Duration	Several hours to days	Several hours to days	Several hours to months	Minutes to few hours	Several hours	Several hours
Round Trip efficiency	60-90%	40-80%	20-70%	85-90%	55-85%	30-60%
Energy Density [Watt-hour/litre]	0.2-2	3-12	500-3000	200-600	16-60	50-500
Lifetime [years]	40	30	30	10	15	30
Suitable scale	>100 MWh		>100 MWh	<10 MWh		>10MWh
Loaction	Geographically dependent	Geographically dependent	Geographically independent	Geographically independent	Geographically independent	Geographically independent

1.2. Thesis outline

The structure of this thesis is organized as follows:

- **Chapter 2** briefly discusses different PTES configurations and modelling approaches in the literature.
- **Chapter 3** discusses selection guidelines for compressors and expanders appropriate for a 100 kW scale system, as well as modelling techniques. This chapter also introduces the objectives of the thesis, with subsequent chapters aiming to address them.
- **Chapters 4 and 5** present the methodology behind the compressor and turbine meanline models used in this thesis. First, loss models from the current literature are identified and introduced. Then using the developed off-design meanline models, the model predictions are compared with experimental cases from open literature. Subsequently, a design approach for each turbomachine is presented using guidelines from the literature and the previously identified loss models.
- In **Chapter 6**, in the context of a 100 kW PTES system, a compressor and turbine are designed using the methodologies discussed in the earlier chapters. The results from the design process are then used to analyse the PTES system's performance under off-design, specifically during its charging and discharging modes.
- **Chapter 7** will finally conclude the thesis and provide recommendations for future work.

2

Pumped Thermal Energy Storage

2.1. PTES

Pumped Thermal Energy Storage (PTES) is a system that uses electricity produced by the grid and stores it in the form of thermal energy by heating solid media, phase change materials (PCM) or high thermal capacity liquids. This thermal energy can later be retrieved by running a heat engine exploiting the temperature difference between this heat source and a low-temperature sink. In periods of excess electricity, a heat pump is used to transfer heat from a cold to a hot reservoir, increasing their temperature difference as shown in figure 2.1. During times of demand, the heat engine cycle is used to produce power by expanding the hot fluid through an expander. As shown in table 1.1, this type of technology allows for the storage of electricity with a high energy and power density, low cost, and reasonable round trip efficiency in comparison to other grid-scale technologies. As this technology is not limited by geographical constraints or the need for rare earth elements, it is an appealing energy storage solution. The ideal round-trip efficiency of such a system is given by the following equation [11]

$$\eta_{RTE} = \frac{W_{out}}{W_{in}} = COP_{HP} \times \eta_{HE}. \tag{2.1}$$

They can also serve as a way of providing heat instead of electricity, thus serving as a key balancing tool for networks for places requiring both heat and electricity. Based on the thermodynamic state of the working fluid, PTES systems can be classified as (i) Brayton and (ii) Rankine cycles.

2.1.1. Brayton PTES

In a Brayton cycle, the working fluid operates in a single gas phase throughout the cycle operation at temperatures usually above 200 °C [13]. A Brayton PTES system consists of using a heat pump using a reverse Brayton cycle during charging and a Brayton heat engine for discharging, as shown in figure 2.3.

Monoatomic gasses such as Argon are normally used for Brayton cycles as they have a high heat capacity ratio [15]. Moreover, fluids with high molecular weight are favoured as their higher densities result in more compact turbomachinery and component dimensions. Typically inorganic fluids such CO_2, Ar, N_2 are used, as they have high thermal stability [16]. In literature, supercritical CO_2 cycles for Brayton PTES systems have been proposed by multiple

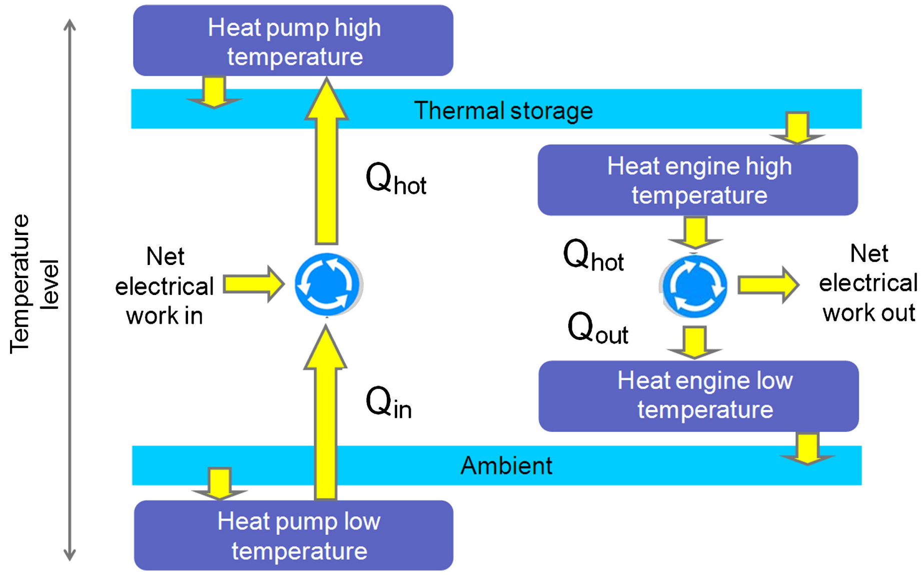
Heat pump high temperature
Thermal storage
Q_hot
Heat engine high temperature
Temperature level
Net electrical work in
Q_hot
Q_out
Net electrical work out
Q_in
Heat engine low temperature
Ambient
Heat pump low temperature

Figure 2.1: Schematic of a PTES system with a hot store, and with the ambient as the low-temperature heat source [11].

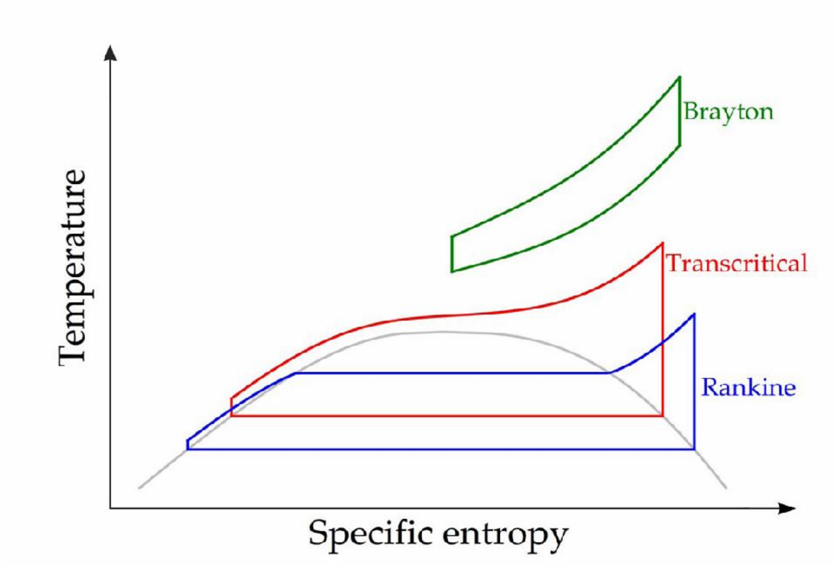

Figure 2.2: T-s diagram showing Brayton, Rankine and transcritical cycles [12].

authors [17, 16, 18]. Using supercritical CO_2 is advantageous as it has a low critical pressure (7.38 MPa), is chemically inert, has high thermal stability and is cheap. Under supercritical conditions, it has a high density, which translates to cost reductions from compact turbomachinery and related auxiliary equipment. However, near the critical point, there is a significant variation in the fluid thermodynamic properties, which requires special considerations in the equipment design.

Solid media are often used for thermal storage purposes due to their stability at elevated temperatures, broad operational temperature range, high volumetric heat capacity, and affordability as stated in [19].

However, the need for high-pressure tanks can significantly escalate costs as the working fluid would have to pass through the storage media. The use of solid media inherently introduces

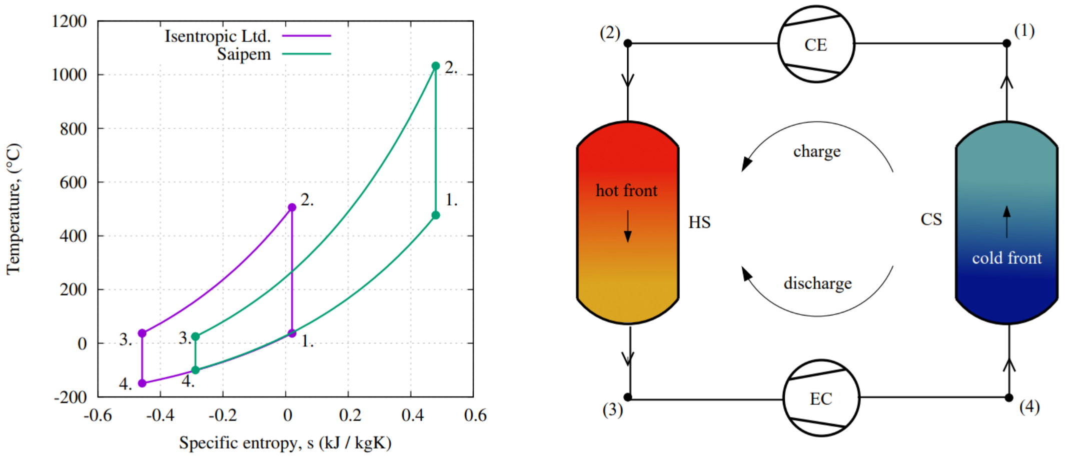
1200
1000
800
600
400
200
0
-200
Temperature, (°C)
-0.6
-0.4
-0.2
0
0.2
0.4
0.6
Specific entropy, s (kJ / kgK)
Isentropic Ltd.
Saipem
1.
2.
3.
4.
1.
2.
3.
4.
(2)
(1)
(3)
(4)
CE
EC
hot front
HS
CS
cold front
charge
discharge

(a) Temperature-entropy diagram for an ideal Brayton cycle.

(b) Schematic of a Brayton cycle employing solid media for thermal storage (as thermoclines).

Figure 2.3: Brayton-based PTES systems as proposed by Isentropic Ltd. and Saipem [14].

a thermal gradient within the storage tank, which can lead to incomplete charging and discharging of the thermal storage. This can necessitate a larger-than-ideal storage capacity to achieve the desired capacity. Additionally, a thermal gradient implies fluctuations in the fluid's exit temperature from the tank, which could influence the thermodynamic cycle [19].

2.1.2. Rankine cycles

A Rankine-based PTES system consists of a standard refrigeration cycle when operating as a heat pump during charging and a Rankine cycle when operating as a heat engine for discharge, as shown in figure 2.4.

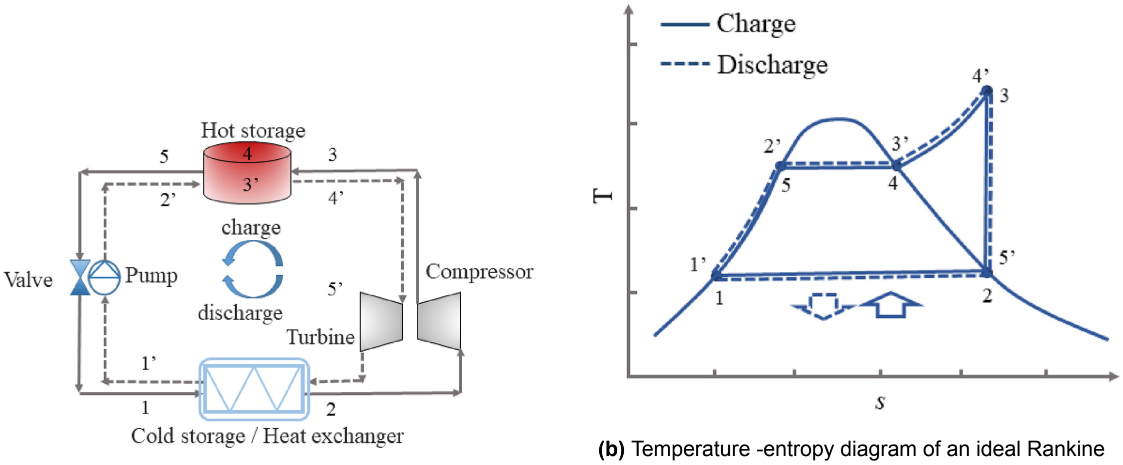
Hot storage
4
3'
5
3
2'
4'
charge
discharge
Valve
Pump
Compressor
5'
Turbine
1'
1
2
Cold storage / Heat exchanger
Charge
Discharge
T
s
4'
3
2'
3'
5
4
1'
5'
1
2

(a) Schematic of a Rankine cycle.

(b) Temperature -entropy diagram of an ideal Rankine cycle.

Figure 2.4: Rankine based PTES system [15].

Figure 2.5 depicts the evolution of the hot thermal store temperature during both the charging and discharging modes. The heat transfer to the hot store is constrained by the pinch temperature, represented as ΔT_{min}. While operating in a transcritical mode, sensible heat storage can be used entirely to receive the heat. However, in sub-critical Rankine PTES, utilizing sensible heat storage for the hot store is not ideal. To minimise exergy loss, a phase change material should be used to transfer heat within the two-phase region, and sensible heat storage in the

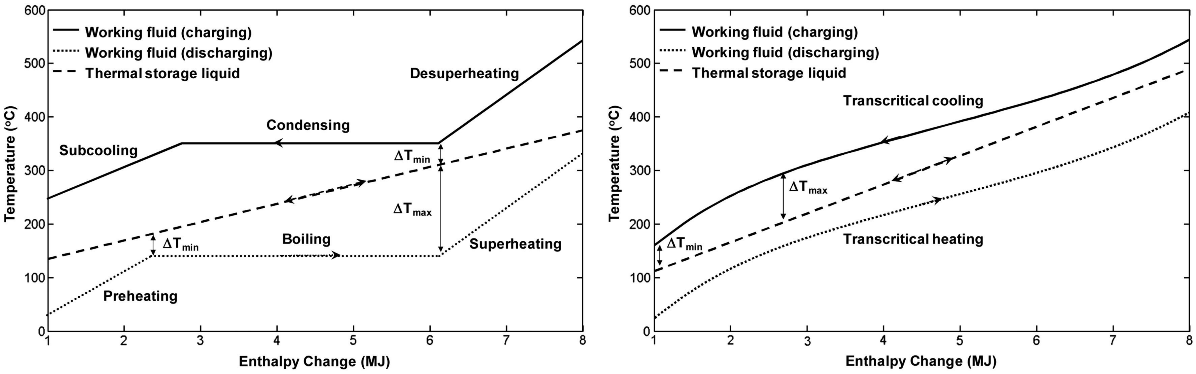

Figure 2.5: Charging and discharging cycles with subcritical (left) and transcritical Rankine cycles (right) [11].

vapour-only region.

Furthermore, these Rankine-based PTES systems can integrate with waste heat sources, enhancing the Coefficient of Performance (COP) of the heat pump. This can potentially lead to round trip efficiencies exceeding 100% [9]. This can be achieved using suitable refrigerants, as in the case of Organic Rankine cycles (ORCs).

Steinmann [9], proposed a subcritical Rankine PTES concept utilising waste heat referred to as Compressed Heat Energy Storage (CHEST), as shown in figure 2.6. The name derives from waste heat being compressed and stored at a high temperature. This concept utilises only a hot store; and during the discharging cycle, the condensation heat is rejected to the ambient. The CHEST configuration combines both sensible and latent heat storage for the hot temperature store to minimise exergy losses. Without waste heat integration, the roundtrip efficiency is approximated at 70% [9]. In a later work by the author [20], integration of a low-grade waste source increased the round trip efficiency to 125%.

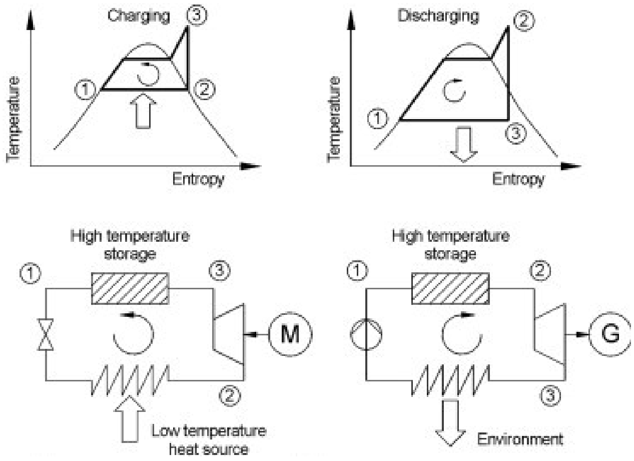

Figure 2.6: CHEST concept with waste heat integration provided by a low-temperature external heat source to reduce compression work during the charging process [9].

Gautam [10] in his work analysed the CHEST layout developed by DLR [9, 20]. Using R1233zd(E) as a working fluid, sunflower oil as sensible heat storage, and a hypothetical PCM, he analysed two configurations for the case of a waste heat source of 80°C and a heat input of 1 MW:

- Case I: A subcritical Rankine cycle using latent heat and sensible storage, depicted in figure 2.7a.

- Case II: A transcritical Rankine cycle is used during charging, while a subcritical cycle is employed during the discharging phase, employing sensible heat storage. Since charging and discharging operations don't occur simultaneously, a common heat exchanger was used for heat exchange in the liquid phase, as shown in figure 2.7b.

On comparing the results, the round trip efficiency of Case I was 118%, and for Case II 91%. Case II was chosen as a better layout to pursue as

- PCMs are associated with complex heat transfer modelling and high costs.
- The PCM would be exposed to the pressure of the working fluid, whereas sensible heat mediums can be stored at ambient as they utilise indirect heat exchange.
- The use of a single heat exchanger would lead to a reduction in the equipment cost.

Radi [2], in his work, provided a detailed approach for the thermodynamic cycle design of PTES systems and a comprehensive framework for optimal fluid cycle selection at different waste and storage temperatures. In addition, reduced-order models of scroll compressors and turbines were used along with the thermodynamic cycle to obtain an integrated model for the case of small-scale PTES systems.

In this thesis, for the case of a 100 kW system, the approach based on Radi [2] is used to design the PTES thermodynamic cycles. For the model inputs, working fluid and storage media, the same selections are made as Gautam [10] and are explained further in section 6.1.

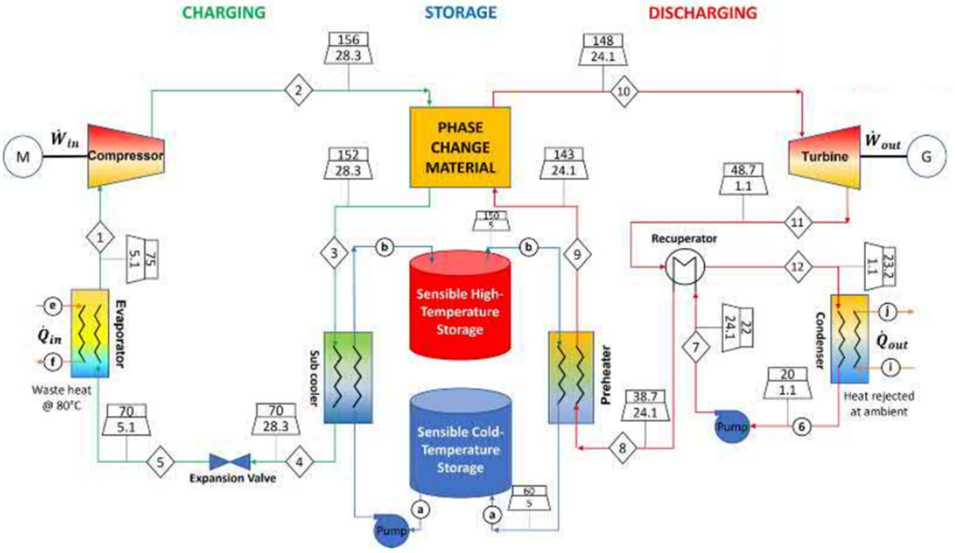
CHARGING
STORAGE
DISCHARGING
156
28.3
148
24.1
2
10
M
$\dot{W}_{in}$
Compressor
PHASE CHANGE MATERIAL
Turbine
$\dot{W}_{out}$
G
152
28.3
143
24.1
48.7
1.1
150
5
11
1
75
5.1
3
b
b
9
Recuperator
12
23.2
1.1
e
$\dot{Q}_{in}$
f
Evaporator
Waste heat @ 80°C
Sensible High-Temperature Storage
Sub cooler
Preheater
22
24.1
7
Condenser
j
$\dot{Q}_{out}$
i
Heat rejected at ambient
70
5.1
70
28.3
Sensible Cold-Temperature Storage
38.7
24.1
20
1.1
8
Pump
6
5
Expansion Valve
4
a
a
60
5
Pump

(a) Case I: system with latent and sensible heat storage.

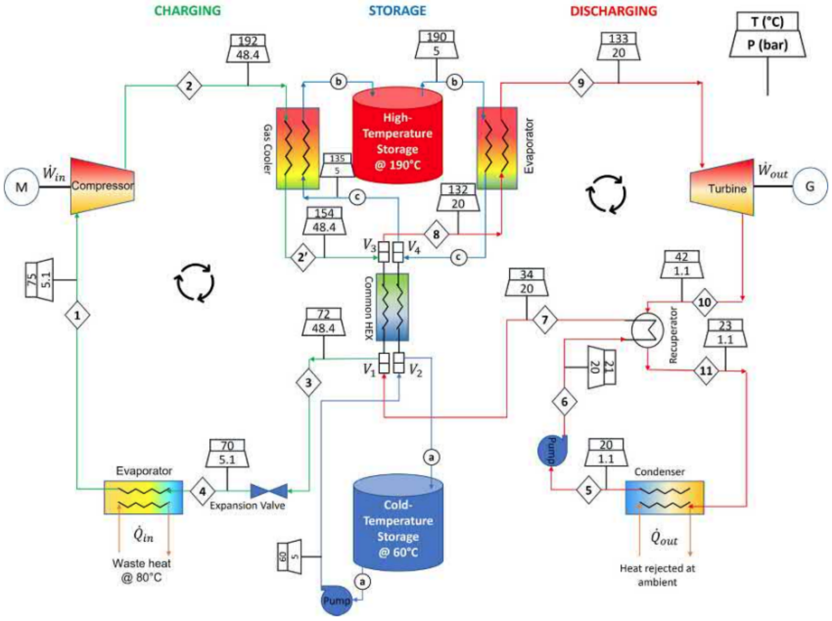
CHARGING
STORAGE
DISCHARGING
T (°C)
P (bar)
192
48.4
190
5
133
20
2
b
b
9
Gas Cooler
High-Temperature Storage @ 190°C
Evaporator
M
$\dot{W}_{in}$
Compressor
135
5
c
132
20
Turbine
$\dot{W}_{out}$
G
154
48.4
8
V_3
V_4
2'
c
75
5.1
1
Common HEX
42
1.1
34
20
10
7
Recuperator
72
48.4
23
1.1
V_1
V_2
21
20
11
3
6
a
70
5.1
Pump
20
1.1
Evaporator
4
Expansion Valve
$\dot{Q}_{in}$
Waste heat @ 80°C
Cold-Temperature Storage @ 60°C
5
Condenser
$\dot{Q}_{out}$
Heat rejected at ambient
60
5
a
Pump

(b) Case II: system with sensible heat storage.

Figure 2.7: PTES systems configurations examined by Gautam [10].

3

Turbomachinery for PTES systems

3.1. Types of compressor and expanders

Compressors and expanders can be categorized into two main types: volumetric and turbomachines, as shown in Figure 3.1. Volumetric machines operate based on the principle of altering the volume of the working fluid using a movable chamber. They operate in a cyclic manner with a fixed volume ratio and can compress or expand fluids depending on the direction of operation. On the other hand, turbomachines facilitate energy transfer between blade rows and the working fluid that flows continuously.

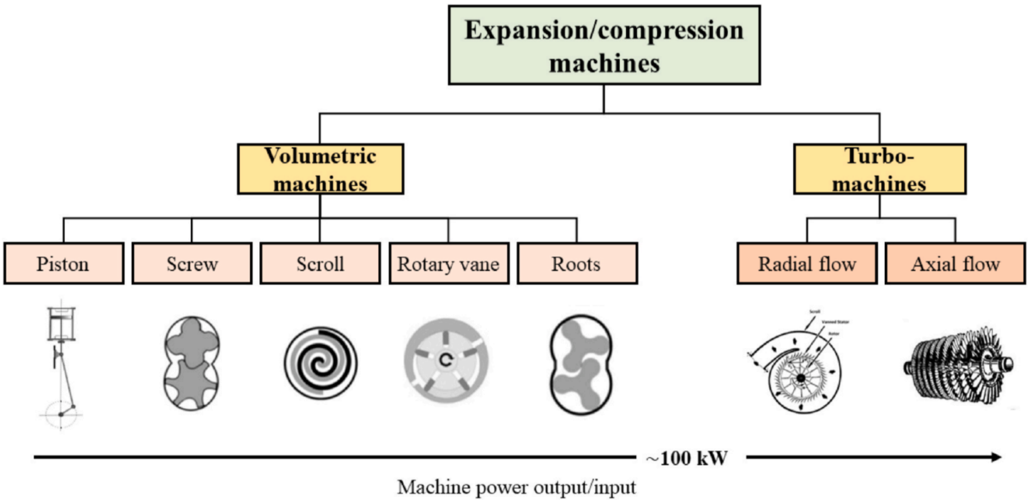
Expansion/compression machines
Volumetric machines
Turbo-machines
Piston
Screw
Scroll
Rotary vane
Roots
Radial flow
Axial flow
~100 kW
Machine power output/input

Figure 3.1: Types of commercially available machines for PTES systems[15].

The selection process for turbomachinery should be guided by various factors, including the system's power and operating conditions such as the properties of the working fluid, volume flow rate, pressure ratio, and inlet conditions [21]. Other important technological constraints, such as project costs, the system's ability to tolerate oil traces, the wet expansion, and compactness, should also be considered when selecting [15]. Figure 3.2, shows the selection procedure for the turbomachinery.

In general, volumetric machines can handle fluids of high density, along with high pressure and expansion ratios. Such machines are generally suitable for small-scale applications below the MW range but are limited to handling low flow rates in the order of 100 liters/s [15]. On the

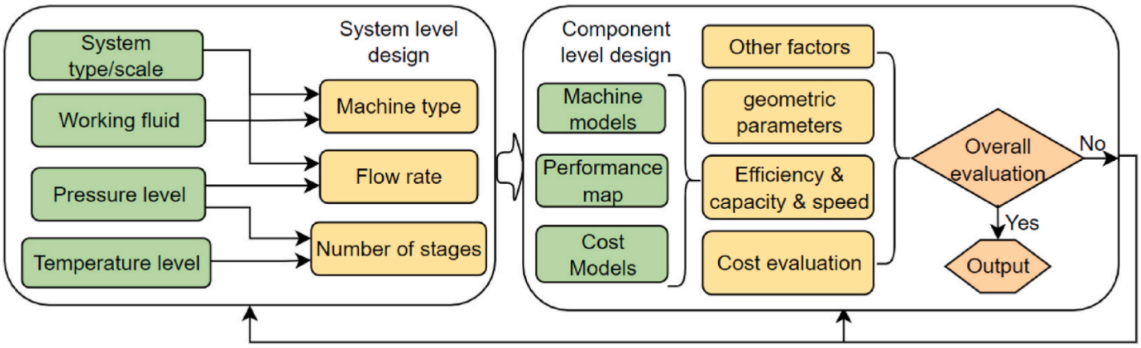
System type/scale
Working fluid
Pressure level
Temperature level
System level design
Machine type
Flow rate
Number of stages
Component level design
Machine models
Performance map
Cost Models
Other factors
geometric parameters
Efficiency & capacity & speed
Cost evaluation
Overall evaluation
No
Yes
Output

Figure 3.2: Selection process for turbomachinery [15].

other hand, Turbomachines are more suited to handling power applications greater than 50 kW, up to the MW range and exhibit the capacity to handle higher volume flow rates with high efficiencies [21]. Therefore, turbomachines are preferred for a PTES system scaled at 100 kW. Turbomachines can be further categorized into axial and radial types, as shown in figure 3.1.

3.2. Terms related to turbomachinery

Three dimensionless quantities are normally used for defining the design parameters of turbomachines [22], namely:

- Flow coefficient (ϕ): This is defined as the ratio of the meridional component of the absolute velocity (C_m), to the peripheral speed (U), and is given by

$$\phi = \frac{C_m}{U}. \tag{3.1}$$

- Work coefficient (ψ): Defined as the ratio of the enthalpy change per stage to the square of the peripheral speed, and is given as

$$\psi = \frac{\Delta h_{stage}}{U^2}. \tag{3.2}$$

- Degree of reaction (R): Defined as the ratio of enthalpy change in the rotor to the overall enthalpy per stage, given by

$$R = \frac{\Delta h_{rotor}}{\Delta h_{stage}}. \tag{3.3}$$

3.3. Similitude theory and preliminary selection

The similitude theory is widely used for the selection and preliminary design of turbomachines. This theory involves utilizing dimensional analysis to describe a physical phenomenon by utilizing a group of dimensionless numbers. In the case of turbomachines, efficiency η can be expressed through four dimensionless parameters [23], given by

$$\eta = f(\Phi, \Psi, Re, M_u), \tag{3.4}$$

where the flow factor is given as

$$\Phi = \frac{\dot{V}}{\omega D^3}, \tag{3.5}$$

and the work factor is

$$\Psi = \frac{\Delta h}{\omega^2 D^2}. \tag{3.6}$$

In the above equations, Re and M_u represent the Reynolds and peripheral Mach numbers, respectively. Turbomachines generally exhibit completely turbulent flows, ie. Reynolds numbers (symbol) greater than 10^6. In such a scenario, the effect of the Reynolds number on the efficiency can be ignored [23]. It is also important to note that in certain scenarios where the fluid behaves in an incompressible manner, the effect of Mach number can be ignored from the efficiency [23]. However, since this thesis deals with compressible fluids, its effect is not negligible.

Balje [24, 25] developed a set of selection diagrams for single-stage turbomachines based on specific speed ω_s and specific diameter D_s as shown in figures 3.3 and 3.4. The expressions for for ω_s and D_s are given as:

$$\omega_s = \frac{\Phi^{1/2}}{\Psi^{3/4}} = \frac{\omega V^{1/2}}{\Delta h^{3/4}}, \tag{3.7}$$

and

$$D_s = \frac{\Psi^{1/4}}{\Phi^{1/2}} = \frac{D \Delta h^{1/4}}{V^{1/2}}. \tag{3.8}$$

This approach, however, assumes the effect of peripheral Mach number on the specific speed is negligible as the flow is incompressible. Despite this limitation, Balje charts provide an estimate of the turbomachinery efficiency at an initial stage [23, 26]. Using these charts, a range of optimal specific speeds is identified as shown in table 3.1.

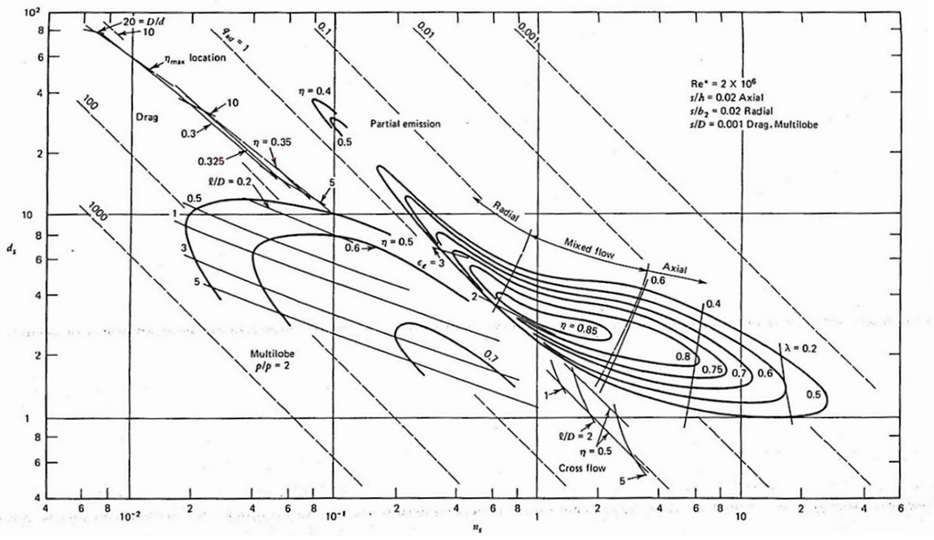

Figure 3.3: Baljé diagram for single stage compressor [27].

A rough guide to turbomachinery selection is also given by a Cordier line as shown in figure 3.5a (Balje maps are an extension of the Cordier line). These maps were developed using statistical data from existing turbomachines and indicate the optimal specific diameter for a given specific speed. Rewriting the specific speed and specific diameter in terms of the work and flow factors, figure 3.5b can be obtained. As the work factor is proportional to the pressure ratio, and the flow factor is proportional to the flow rate, this figure shows that there is a

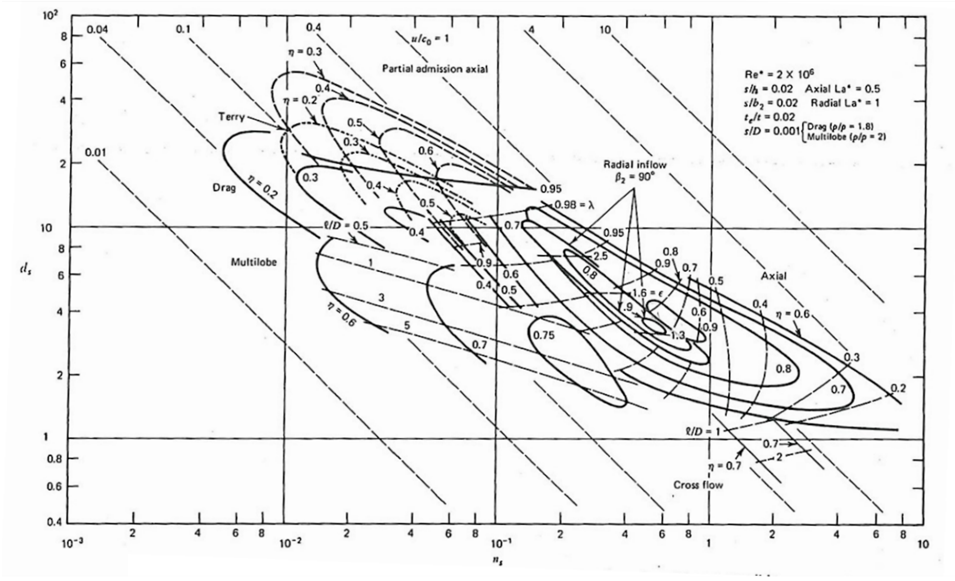

Figure 3.4: Baljé diagram for single stage turbine [27].

Table 3.1: Turbomachinery specific speed ranges for high efficiency [23].

Turbomachine type	Specific speed range
Axial compressor	1.5-2.5
Radial compressor	0.4-1.0
Axial turbine	0.6-1.2
Radial turbine	0.6-1.2

distinction in the range of operation of axial and radial types of machines. Hence axial-type of machines are suited for high mass flow rates and stage low-pressure ratios, and the converse holds for radial machines.

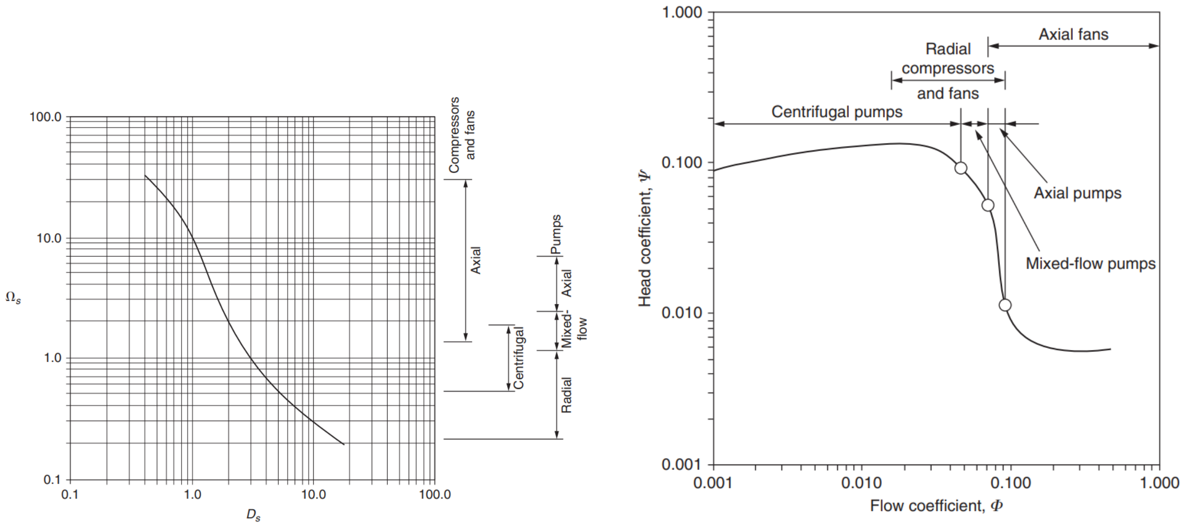

(a) Cordier line for turbomachines [23].

(b) In this figure, ψ and ϕ were defined using the definitions of work factor Ψ and Φ respectively.

Figure 3.5: Selection diagrams for turbomachines [22].

3.4. Turbomachinery type for 100 kW PTES system

The following distinguishing features can be made for axial and radial types of turbomachinery:

- As discussed in the previous section, axial machines are suited for high flow rates, whereas radial machines are more appropriate for lower flow rates. Moreover, if an axial-type machine is designed for low volume flow rates, the blades of the machine become very small, resulting in a significant loss of clearance due to the high relative clearance between the blade tip and the casing. As a result, the efficiency of the machine is reduced [21].
- Radial machines are less affected by blade shape variations and are robust under high-loading conditions. This characteristic is particularly important in Organic Rankine Cycle (ORC) applications where high-density fluids are used [21].
- Radial machines benefit from the centrifugal effect, enabling them to achieve high pressure ratios or manage significant expansion ratios [22]. In contrast, axial turbomachines need multiple stages to reach comparable pressure ratios. Axial compressors typically have low pressure ratios per stage of around 1.2 [28], whereas centrifugal compressors can reach up to pressure ratios of 5 in a single stage [29]. Radial turbines can operate for expansion ratios normally up to 6 [30], and also up to expansion ratios up to 100 [31], whereas an axial turbine can allow an expansion ratio of up to 2-3:1 [21].
- Radial machines are flexible to operating conditions making them suited for applications requiring large variations in flow rate and pressure ratios such as environmental control systems [32].
- Radial turbomachines tend to be more compact and cheaper compared to their axial counterparts [21].

As will be shown later in chapter 6, for the 100 kW scale PTES system, high-pressure ratios of approximately 9 and 20 are required for the compressor and turbine respectively. Given the high-pressure ratio requirements, radial turbomachines are more suitable. Therefore, a centrifugal compressor and a radial turbine have been selected, which will be discussed in detail in the following chapters.

3.5. Turbomachinery models for PTES

In the process of modelling PTES systems, it is usually assumed that the performance of associated turbomachinery remains the same and does not vary based on operating conditions. Several authors [33, 9, 34], use a constant value for turbomachinery polytropic efficiency based on typical industry available options in their models in their PTES models.

Alternatively, Gonzalez [35] adopted an empirical approach for studying a CAES system under a dynamic state. In this approach, turbine and compressor models were created using lookup tables of mass flow rate and efficiency for a specific pressure ratio. The lookup table data was made using performance maps of existing turbomachinery and then scaled for the conditions based on the methodology proposed by [36]. The accuracy of this method depends on the amount of experimental data points available, and hence, a good empirical model requires a large set of data to cover the entire operating range accurately.

Another approach for estimating the performance and conducting preliminary design of turbomachinery is through one-dimensional meanline models. This approach views each part of the machine, such as the diffuser, impeller, and stator, as distinct control volumes. The method then calculates the inlet and exit thermodynamic properties using empirical and physics-based loss models [23]. These models offer reasonable accuracy and demonstrate good agreement with CFD and experimental data, with low to medium computational expense [15], making them suitable for PTES system modelling. Additionally, they provide a starting point for preliminary design, considering the inlet conditions and pressure ratio demands, setting the stage for the subsequent steps in the design process.

Finally, Computational Fluid Dynamics (CFD) is a powerful tool used for predicting turbomachinery performance and aiding in its design. Turbomachinery flow is typically three-dimensional and unsteady in nature, and CFD allows for numerical simulations of these complex flow behaviours by solving the governing equations for fluid flow. These simulations provide insights into flow patterns, pressure distributions, and temperature distributions, which can be used to assess the suitability of a given design with high accuracy [15, 37].

However, it is important to note that CFD simulations are computationally expensive, and are often employed for detailed turbomachinery design after arriving at an optimal design using preliminary design tools [22].

In the literature, meanline models, CFD studies, and experimental data are often compared together to assess their validity. For instance, Giuffre et al. [38] compared their compressor meanline model predictions with experimental reference cases as a variation study, and then for their design case compared the meanline predictions with CFD simulation results to assess their respective accuracy.

Similarly, Monje [39] compared compressor meanline models and CFD results with experimental data of supercritical CO_2 centrifugal compressors from SANDIA Laboratory. In the case of radial turbines for ORC applications, Servi et al. [40] conducted a CFD study using a geometry derived from meanline models. However, CFD modelling may be unsuitable due to its high computational cost when it comes to modelling PTES systems.

The following chapters will discuss meanline methods for the chosen turbomachinery. Also, the Coolprop fluid library [41] is utilized to obtain thermodynamic properties.

3.6. Thesis objectives

The primary objective of this thesis is to model a PTES system tailored for a power output scale of 100 kW. Working at these scales of operation, it is more suitable to use turbomachinery for the compressor and expander models.

Turbomachines, in the context of energy storage systems, must also accommodate off-design operations to provide load-balancing. As a result, evaluating the off-design performance characteristics of the selected turbomachines is vital. However, the operational ranges of turbomachines inherently set bounds on the PTES system's functioning. With this understanding, the following research objectives and goals are formulated.

Thesis Objective 1:

"Development of mean line models for a Centrifugal Compressor and a Radial Turbine for sub and transcritical Rankine cycles"

Goals:

1. Development of meanline models for turbomachinery design
2. Development of off-design meanline models
3. Validation of the off-design models against experimental data available in the literature.

Thesis Objective 2:

"To model the off-design characteristics of a 100 kW PTES system"

Goals:

1. Design turbomachines for the application of a 100 kW size PTES system
2. Sensitivity study of PTES system based on off-design turbomachinery performance
3. PTES round trip efficiency under varying charging and discharging scenarios.

4

Centrifugal compressor model

Centrifugal compressors are commonly used across various industries due to their compactness and high efficiency. However, the complex and three-dimensional nature of the flow across the compressor makes accurate modelling challenging. While high-fidelity tools such as CFD can offer insight into compressor performance, they are computationally expensive and unsuitable for the initial design phases. As a viable alternative, one-dimensional meanline tools offer a compromise by providing reasonable agreement with CFD and experimental data [42]. This tool can obtain preliminary geometric design and performance estimates, which can be further refined through CFD studies and experiments. Given their satisfactory accuracy and low computational needs, one-dimensional meanline models are particularly well-suited for PTES system modelling [15] and are explained in the following sections.

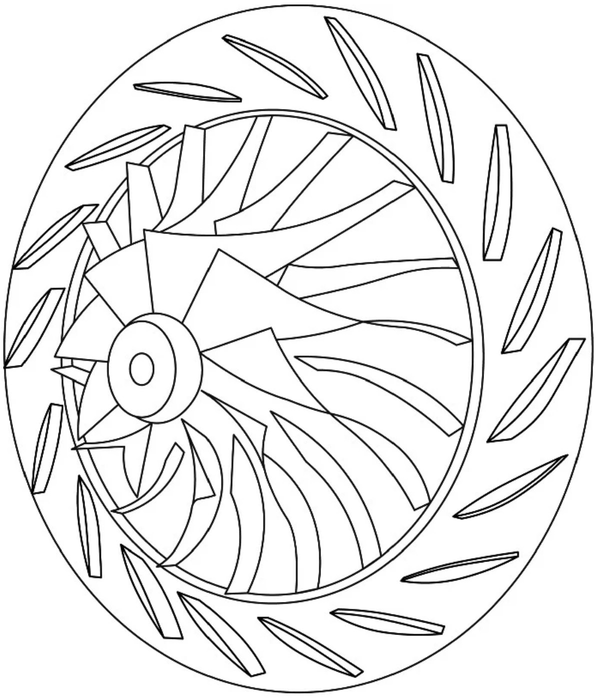

Figure 4.1: A centrifugal compressor [23].

4.1. Compressor stations

Centrifugal compressors typically consist of a rotating impeller and a volute. Optionally, inlet guide vanes can be used to broaden the compressor's operational range. Additionally, vaned diffusers can enhance the pressure ratio, but this may reduce the operational range. However, this thesis does not account for these components or the volute. The subsequent figure outlines the naming conventions used throughout this work.

- 1-2: Impeller
- 2-3: Vaneless diffuser

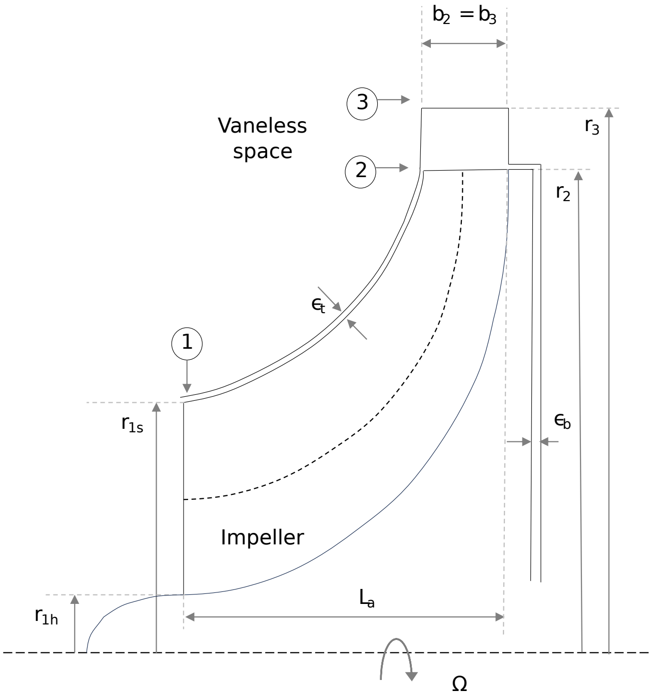

Figure 4.2: Compressor stations naming conventions for this thesis.

4.2. Velocity triangles

The velocity triangles at the inlet and outlet of the rotor are shown in figure 4.3. Using the velocity triangles, the flow angles and velocity components can be found. At the impeller inlet, the flow enters with an angle α_1. As the impeller is rotating with a velocity u_1, the rotating frame of reference is considered, and it enters with relative velocity w_1. Here, relative velocity is defined as

$$\vec{w} = \vec{c} - \vec{u}. \tag{4.1}$$

In the case of centrifugal compressors, the flow at the impeller exit is partly deflected due to the effects of slip, which can impact the compressor's overall performance. Due to this effect, the relative velocity at the impeller exit will deviate from that of perfectly guided flow, and this variance is termed 'slip'. Ideally, the flow should leave the impeller along the blade outlet angle β_{2b}, but due to slip, it exits at an angle β_2 as shown in figure 4.4.

Dixon and Hall [22] described this phenomenon using the relative eddy concept. They explained that if a frictionless fluid enters the impeller without spin, it should also leave without

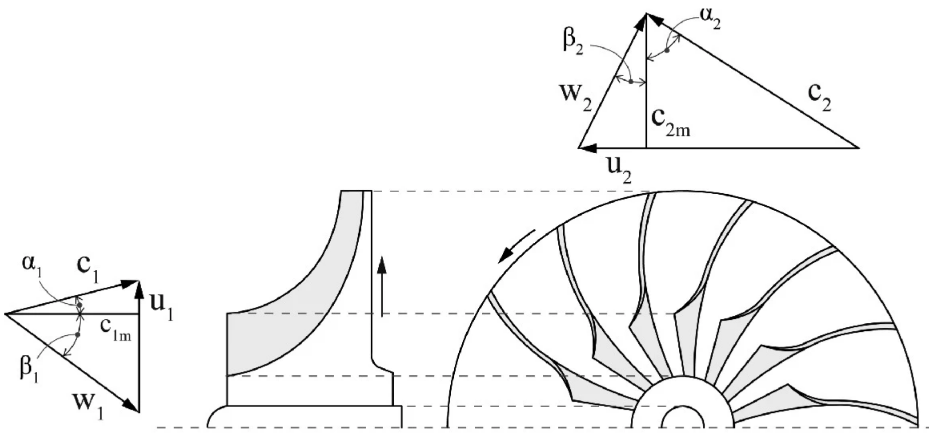

Figure 4.3: Velocity triangles at impeller inlet and exit [23].

any spin. However, because the impeller has angular momentum, the flow acquires an opposite momentum inside the impeller, referred to as the relative eddy. Superimposing this over a through flow explains the net effect of slip. Casey [43] outlines four contributions to this slip effect:

- Primarily, it is the relative eddy concept mentioned above.
- Difference in velocities between the suction surface and pressure surface near the trailing edge causes a deviation in the flow angle towards the suction side.
- The trailing edge cannot support a pressure difference as there is a condition of zero-loading at the trailing edge, which means the flow will not follow the trailing edge angle.
- Flow recirculation occurs between a vane channel's pressure and suction sides.

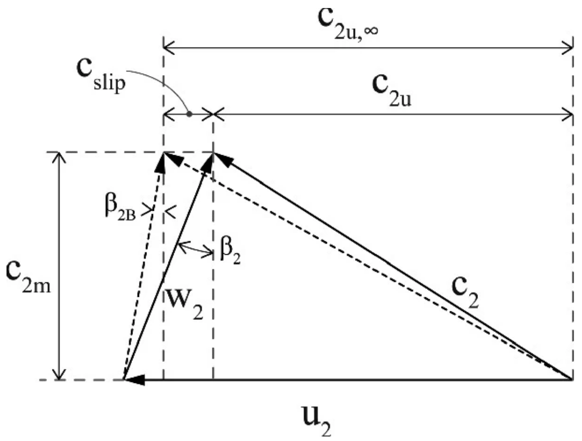

Figure 4.4: Velocity triangle at impeller exit showing the effect of slip [23]. Here β_{2B} represents the blade angle at the rotor exit, and $c_{2u,\infty}$ denotes the tangential component of the velocity without slip.

In the literature, numerous slip relations are present. Stanitz [44] introduced a relation for the slip factor as

$$\sigma = 1 - \frac{0.63\pi}{N_b}. \tag{4.2}$$

He observed that the slip velocity wasn't dependent on the blade angle, denoted as β_{2b}, but was influenced by the blade pitch.

Wiesner [45] proposed a slip factor by reviewing various relations for slip factors compared to the results from experimental tests, and proposed the following relation:

$$\sigma = 1 - \frac{\sqrt{cos(\beta_{2b})}}{N_b^{0.7}}, \tag{4.3}$$

which is applicable up to a certain solidity limit given as

$$\left(\frac{r_1}{r_2}\right)_{lim} = e^{\left(\frac{-8.16cos\beta_{2b}}{N_b}\right)}. \tag{4.4}$$

4.2.1. Work done in centrifugal compressors

In the impeller, the specific work imparted is given by the Euler equation: [22]

$$W = h_{02} - h_{01} = u_2c_{2\theta} - u_1c_{1\theta}, \tag{4.5}$$

which can also be written as

$$W = h_{02} - h_{01} = h_2 - h_1 + \frac{1}{2}(c_2^2 - c_1^2). \tag{4.6}$$

From the steady flow equation [22], the compressor work is given by

$$W = \frac{1}{2}\left((c_2^2 - c_1^2) + (u_2^2 - u_1^2) + (w_1^2 - w_2^2)\right). \tag{4.7}$$

Now, equating equations (4.6) and (4.7), we get

$$I = h_1 + \frac{1}{2}(w_1^2 - u_1^2) = h_2 + \frac{1}{2}(w_2^2 - u_2^2), \tag{4.8}$$

where I is known as rothalpy and is constant across the impeller stage. After evaluating the velocity triangles, the Mollier diagram can be drawn as shown in figure 4.5.

4.3. Performance range

Figure 4.6 depicts the performance map for a centrifugal compressor, bounded by two lines: the surge/stall line and the choke line.

- Surge/Stall line: The surge/stall line demarcates the flow rate below which the compressor undergoes unstable operation [22]. Surge is a flow condition in centrifugal compressors, characterized by the entire compressor system becoming unstable. This instability leads to abrupt in both the inlet and outlet conditions, causing fluctuations in the overall mass flow over time. Typically, surge incidents occur when the performance curve exhibits either zero or positive slope. In this study, the surge point is identified point where the slope of the pressure ratio curve reaches zero.

  Another significant factor contributing to the compressor instability is the rotating stall [43, 46]. Rotating stall is characterized by a cyclic and unsteady flow pattern, featuring alternating high and low-pressure zones rotating in the direction of the impeller rotation at subsynchronous speeds. In vaneless centrifugal compressors, the rotating stall usually results from boundary layer separation on the diffuser wall, leading to reverse flow [43].

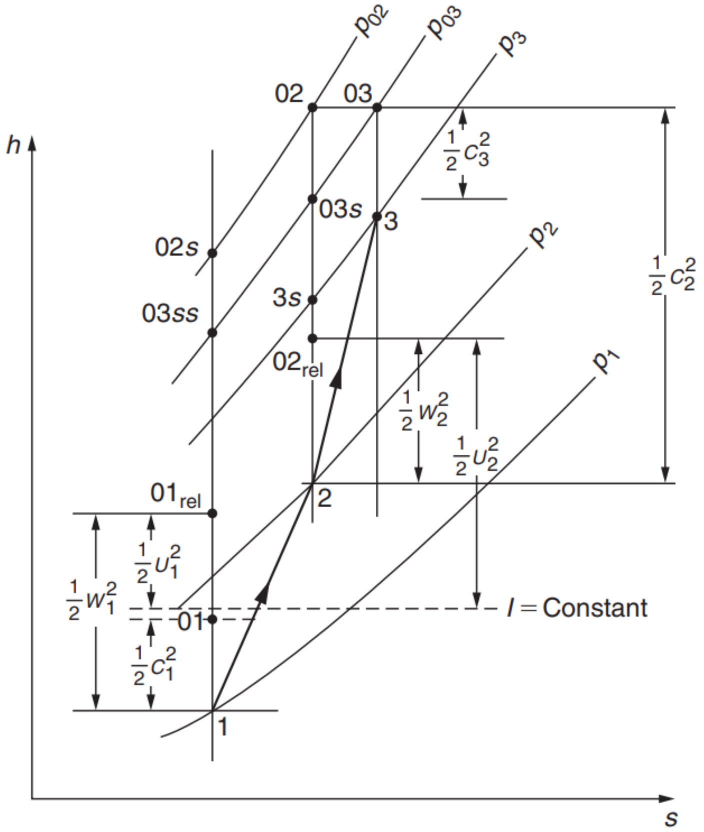
h
s
p_{02}
p_{03}
p_3
p_2
p_1
02
03
$\frac{1}{2}c_3^2$
03s
3
02s
03ss
3s
02_{rel}
$\frac{1}{2}c_2^2$
$\frac{1}{2}w_2^2$
$\frac{1}{2}U_2^2$
01_{rel}
2
$\frac{1}{2}U_1^2$
$\frac{1}{2}w_1^2$
01
$I = \text{Constant}$
$\frac{1}{2}c_1^2$
1

Figure 4.5: Mollier diagram of a typical compressor. Points 1, 2 and 3 refer to the impeller inlet, impeller outlet and diffuser outlet respectively [22].

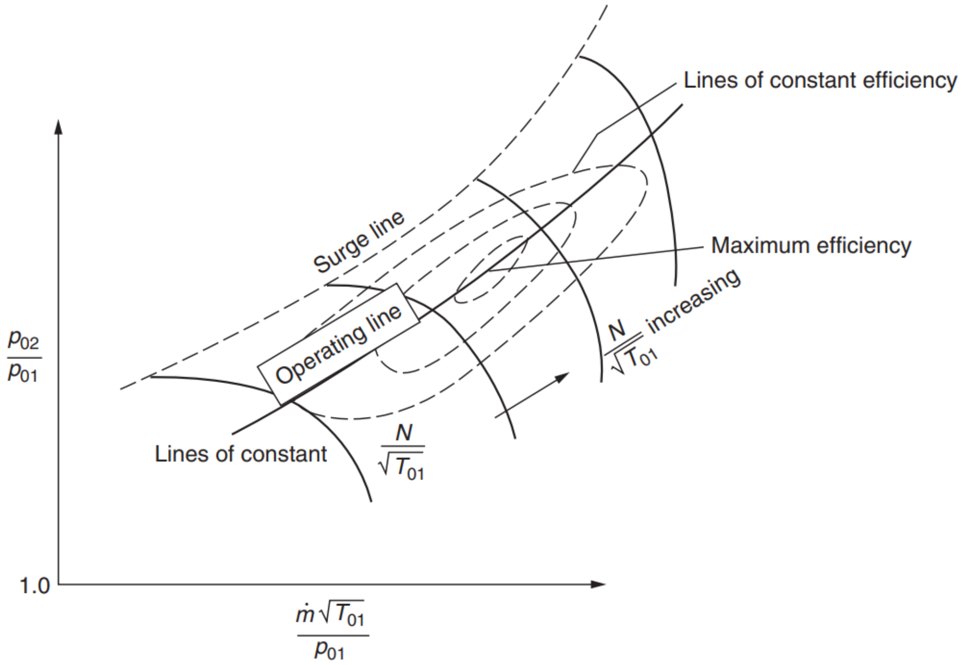

Figure 4.6: Typical performance map for a compressor [22].

For the meanline model, the estimation of rotating stall can be achieved using the methodology outlined by Van den Braembussche [47], which is based on the research conducted by Senoo et al. [48], as depicted in figure 4.7. In the compressor at a constant speed, the absolute flow angle leaving the impeller (α_2), increases as the flow rate decreases. As shown in Figure 4.7, rotating stall is likely to occur if the value of α_2 surpasses the critical stall angle, denoted as α_{2c}. Giuffre et al.'s meanline model [38] also employs a similar approach to assess rotating stall.

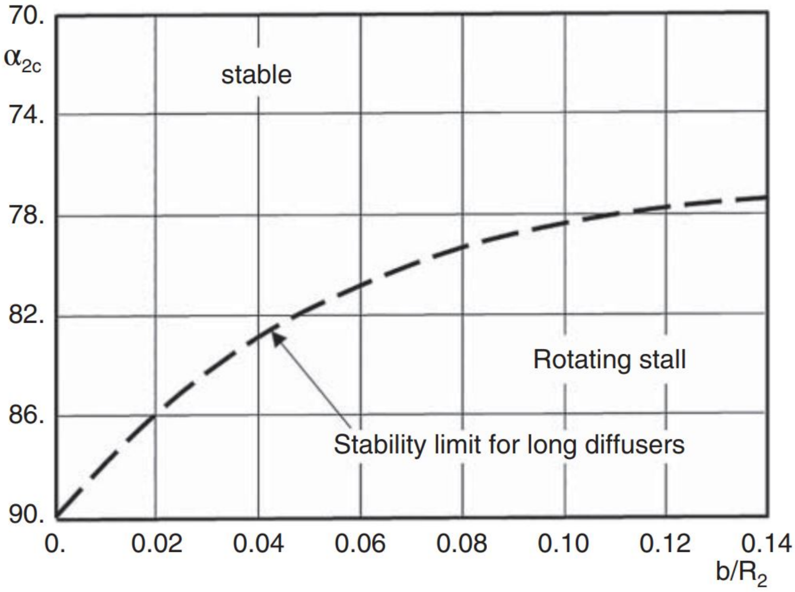

Figure 4.7: Variation of critical flow angle with diffuser width [47].

- Choke line: The maximum flow rate that a compressor can handle happens when the Mach number at one of the stations reaches unity. Choking may occur at any station in the compressor, depending on the flow velocity and the local speed of sound at that particular station [38].

Once the surge and choking limits are known for a given rotational speed, the compressor performance map can be drawn at various speeds.

4.4. Meanline model for centrifugal compressors

According to Monje [39], a one-dimensional model is a numerical tool that calculates the thermo-fluid dynamic state of the fluid at the interface between the various components of the turbomachinery being analyzed. In a meanline model, it is assumed that the flow conditions are steady and uniform over certain flow cross-sections. This approach entails modelling each compressor component separately in the flow direction, with each section defined by an inlet and discharge surface. Depending on the specific component being modelled, different loss correlations are applied between these surfaces.

4.4.1. Meanline models in literature

The procedure for one-dimensional meanline design has been detailed in multiple textbooks such as Aungier [46], Japikse [37], Whitfield and Baines [49], Gambini and Vellini [23].

Japikse [37] proposed that the exit flow of the impeller can be split into two zones, namely an isentropic core flow (jet) and a non-isentropic distorted flow (wake), where the losses occur.

However, the ratio of wake and jet is unknown a priori to the design of the impeller, and a suitable guess would be needed. An alternative approach is the ”one-zone” model described by Aungier [46], where no distinction is made at the impeller exit, and entropy generation due to this is accounted for by using loss models.

In their textbook, Gambini and Vellini [23] provide a comprehensive approach to the design of compressors, with complete relations for all the loss models used. In addition, loss relations based on total pressure and enthalpy are presented in detail.

Monje [39], while designing compressors for supercritical CO_2, followed the one zone modelling approach by Aungier [46], citing the uncertainty of assuming the wake fraction.

Schiffmann and Favrat [50, 51] developed a meanline model for a centrifugal compressor using R134a refrigerant and validated it against experimental data. Although this work includes multi-objective optimization to maximize compressor efficiency and operating range, the details of the modelling approach and loss models are limited. Nevertheless, the experimental data within this study aids in validating the meanline model.

Meroni et al. [52] presented a detailed meanline model for a radial compressor for a heat pump application. The authors optimized the compressor design, in conjunction with the heat pump model, to maximize both compressor efficiency and coefficient of performance (COP) of the heat pump, assigning equal weights to both objectives. Meroni cited a combination of compressor loss models used by various authors, which gave good agreement against experimental data for air, R134a and supercritical CO_2, in a bid to establish a generic fluid compressor design model. This work serves as a valuable reference for loss model combinations and meanline modelling approaches.

Giuffre et al. [38] investigated the impact of size and working fluid on the efficiency, operating range, and axial thrust of high-speed centrifugal compressors. They developed a meanline model validated against experimental data from Eckardt impellers O and B [53, 54, 55] for air and Schiffmann and Favrat [50, 51] for R134a. They also conducted a design optimization, aiming to maximize efficiency and operating range. This work provides comprehensive details on loss models and the experimental cases used for validation.

As shown later in section 6, refrigerant R1233zd(E) was chosen as the working fluid for the compressor, and hence, the validation of the meanline model for another refrigerant is valuable. In meanline model validation results for the Schiffmann impeller using refrigerant R134a, both authors [38] and [52] obtained good agreement for the pressure ratio at off-design conditions. While validating efficiency at off design, Guiffre obtained a good agreement as more than the experimental data fell with the $\pm$ 5% uncertainty band predicted by the model. Meroni obtained a higher deviation of 8% deviation, and similar deviations were obtained by Schiffmann and Favart as well. The loss models employed in these studies are nearly identical, except for the skin friction model. Thus, the loss modelling strategies used in both studies hold value for the design of R1233zd(E) compressors.

4.5. Loss models

Loss models are used as a substitute to account for the complex fluid flow inside the compressor. Based on previous experimental data and observations, these models are semi-empirical in nature. In literature, numerous relations and combinations of loss models have been studied. These losses can be expressed as total pressure or total enthalpy losses.

Among the most cited works in the literature on loss models is of Oh et al. [56]. They conducted a study examining literature loss models from open literature. They identified the optimal combination of loss models that closely matched experimental data for Eckardt impellers O, A, and B [53, 54, 55].

More recently, Zhang et al. [57] reviewed numerous loss relations in literature and evaluated their suitability to 8 experimental cases from open literature. They proposed splitting the loss model choice based on the inlet Mach number and specific speed into three groups and proposed combinations that would be most suitable for each group.

Pressure-based loss models, primarily by Aungier [46], are another approach and were followed by Monje [39], Spazzoli [58], among others.

Botha et al. [59] and Solaesa [60] have conducted studies comparing the pressure and enthalpy-based models. This thesis uses enthalpy-based loss models as they are more commonly used in literature and agree well with experimental results.

Giuffre [38], and Meroni [52] both proposed loss combinations and validated them against experimental data from open literature, serving as a good base for this thesis work. Hence, in this work, loss models by Giuffre et al. [38] are used.

4.5.1. Internal Loss models

These losses occur in the fluid flow across the stator, rotor, and entire turbomachinery stage and impact the thermodynamic state of the fluid during compression and expansion processes [23]. The following losses are considered in the impeller and are detailed below.

- Incidence loss (Δh_{inc}): These losses arise due to the incidence angle between the relative velocity and the blade angle at the impeller inlet. The incidence will be minimal at the design point and increase at other flow conditions. The incidence loss by Galvas et al. [61] is used and is given as

$$\Delta h_{inc} = \frac{(w_1 \sin|\beta_1 - \beta_{1,opt}|)^2}{2}, \tag{4.9}$$

  where $\beta_{1,opt}$ is calculated as [62, 49]

$$\beta_{1,opt} = \tan^{-1}\left(\frac{\pi D_{1m}}{\pi D_{1m} - N_b t_b}\tan\beta_{1b,m}\right). \tag{4.10}$$

- Frictional Loss (Δh_{sf}): Loss attributed to the viscous shear forces exerted by fluid over the impeller surfaces. The frictional loss given by Jansen [63] is used as,

$$\Delta h_{sf} = 2c_f \frac{L_{hyd}}{D_{hyd}}\bar{W}^2, \tag{4.11}$$

  where the hydraulic diameter (D_{hyd}) and length (L_{hyd}) are given by

$$D_{hyd} = \frac{2r_2}{\dfrac{N_b}{\pi\cos\beta_{2b}} + \dfrac{2r_2}{b_2}} + \frac{2r_{1s}}{\dfrac{2}{1 - r_{1h}/r_{1s}}} + \frac{2N_b}{\pi(1 + r_{1h}/r_{1s})} + \sqrt{(1 + \tan^2\beta_{1bs}\left(1 + \frac{(r_{1h}/r_{1s})^2}{2}\right)}, \tag{4.12}$$

  and

$$L_{hyd} = \frac{\pi}{8}(2r_2 - (r_{1s} + r_{1h}) - b_2 + 2L_z)\left(\frac{2}{\dfrac{(\cos\beta_{1s} + \cos\beta_{1h})}{2} + \cos\beta_{2b}}\right). \tag{4.13}$$

For $\bar{W}$, the weighted average approach by Aungier [46] is used

$$\bar{W} = \frac{c_{1s} + c_2 + w_{1s} + 2w_{1h} + 3w_2}{8}. \tag{4.14}$$

To calculate the skin friction coefficient c_f, the set relations described in Gambini and Vellini [23] are used and mentioned here. These relations are defined using a Reynolds number based on the hydraulic diameter as

$$Re_D = \frac{\rho_1 w_{1,mid} D_{hyd}}{\mu_1}. \tag{4.15}$$

- When the flow is laminar (Re_D<2000), the skin friction coefficient is

$$f_{sf} = \frac{16}{Re_D}. \tag{4.16}$$

- When the flow is turbulent, (Re_D>4000), first the skin friction coefficient for smooth (f_{ts}) and fully rough walls (f_{tr}) are evaluated as:

$$\frac{1}{\sqrt{f_{ts}}} = -4\,\mathsf{log}_{10}\left(\frac{1.255}{Re_D\sqrt{f_{ts}}}\right), \tag{4.17}$$

  and

$$\frac{1}{\sqrt{f_{tr}}} = -4\,\mathsf{log}_{10}\left(\frac{k_s}{3.71 D_{hyd}}\right), \tag{4.18}$$

  where ks is the surface roughness. Now, using the following Reynolds number

$$Re_e = (Re_D - 2000)\frac{k_s}{D_{hyd}}, \tag{4.19}$$

  the weighted average of the skin friction coefficient is calculated as

$$\begin{aligned} f_{sf} = f_t = f_{ts}, \quad &\text{when} \quad \mathrm{Re}_e < 60 \\ f_{sf} = f_t = f_{ts} + (f_{tr} - f_{ts})\left(1 - \frac{60}{Re_e}\right), \quad &\text{when } \mathrm{Re}_e \geq 60. \end{aligned} \tag{4.20}$$

- For values of Re_D between 2000 and 4000, the skin friction coefficient in the transitional region is approximated by

$$f_{sf} = f_{l,(\mathrm{Re}_D=2000)} - \left(f_{l,(\mathrm{Re}_D=2000)} - f_{t,(\mathrm{Re}_D=4000)}\right)\left(\frac{\mathrm{Re}_D}{2000} - 1\right). \tag{4.21}$$

Using the above relations, figure 4.8 can be plotted as shown below.

- Blade loading loss (Δh_{bl}): This loss takes into account the secondary flow (generated by 3D flow effects in the rotor) effects due to the pressure gradient across the rotor suction and pressure faces. The relation by Coppage [64] is used

$$\Delta h_{bl} = 0.05 D_f^2 u_2^2, \tag{4.22}$$

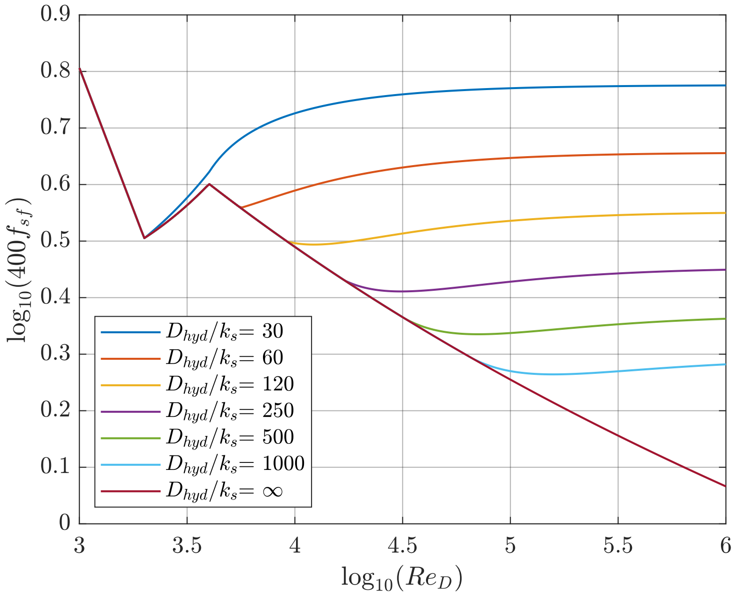

Figure 4.8: Skin friction correlation [23, 46].

where

$$D_f = 1 - \frac{w_2}{w_{1s}} + \frac{\dfrac{0.75\Delta h_{tt} w_2}{u_2^2 w_{1s}}}{\dfrac{N_{b,eff}}{\pi} + 2\dfrac{D_{1s}}{D_2}}. \tag{4.23}$$

- Mixing loss ($\Delta h_{mix,impeller}$): Loss that takes place downstream of the rotor exit where the wake mixes with the channel flow. To calculate this the relation by Johnston and Dean [65] is used, and is given by

  $$\Delta h_{mix} = \frac{1}{1+\tan^2\alpha_2}\left(\frac{1-\varepsilon_{wake}-b^*}{1-\varepsilon_{wake}}\right)^2 \frac{c_2^2}{2}, \tag{4.24}$$

  where ε_{wake} is the wake area fraction, and b^* denotes the rotor exit width ratio to the diffuser's inlet width, which is equal to 1.

  According to Giuffre [38], the value of ϵ_{wake} should be adjusted to reproduce the efficiency decay close to the choke point. They suggest setting ϵ_{wake} to a minimum of 0.2 and increasing it in a geometric progression from 0.2 to 0.65, starting at 80% of the choking flowrate. Therefore, to evaluate the mixing loss at a specific point, one must first perform a mass flowrate sweep until the choke point and then calculate the value of ϵ_{wake} according to the geometric progression. In section 4.6.4, for the model validation, ϵ_{min} and ϵ_{max} act as tuning parameters as the wake fraction is unknown beforehand.

- Clearance loss (Δh_{cl}): Losses due to the mixing of flows due to the mechanical clearance between the rotor and the casing. The following relation by Jansen [63] is used as

  $$\Delta h_{cl} = \frac{0.6\varepsilon_t c_{2\theta}}{b_2}\sqrt{\frac{4\pi c_{2\theta} c_{1m}(r_{1s}^2 - r_{1h}^2)}{(r_2 - r_{1s})(1+\rho_2/\rho_1)}}. \tag{4.25}$$

4.5.2. External loss models

These loss mechanisms contribute to an increase in external work input without resulting in a total pressure rise [38]. The following external loss mechanisms are considered:

- Disc Friction loss (Δh_{df}): This loss is associated with the shear stresses exerted between the fluid in the clearance gap between the impeller backface and casing. The relation by Daily and Nece [66] is used to model this loss as:

$$\begin{aligned} &\Delta h_{df} = K_f \left(\frac{\rho_1 + \rho_2}{2}\right) \frac{r_2^2 u_2^3}{4\dot{m}} \\ &\text{if } Re_{df} = \frac{\rho_2 r_2 u_2}{\mu_2} < 3 \cdot 10^5 \quad K_f = \frac{3.7\,(\epsilon_b/b_2)^{0.1}}{Re_{df}^{0.5}} \\ &\text{if } Re_{df} = \frac{\rho_2 r_2 u_2}{\mu_2} \geqslant 3 \cdot 10^5 \quad K_f = \frac{0.102\,(\epsilon_b/b_2)^{0.1}}{Re_{df}^{0.2}}. \end{aligned} \tag{4.26}$$

- Recirculation loss (Δh_{rc}): The recirculation loss is due to flow reversal at the trailing edge of the impeller blade. This effect is generally considered negligible at the design point, but it becomes increasingly significant at lower flow rates. The equation by Oh et al.[56] is used to account for this loss as

$$\Delta h_{rc} = 8 \times 10^{-5} \,\text{sinh}(3.5\alpha_2^2) D_f^2 u_2^2, \tag{4.27}$$

  where D_f is calculated according to the equation (4.23).

- Seal leakage loss (Δh_{lk}): Some of the flow coming out from the impeller leaks through the clearance gaps and labyrinth seals to the lower pressure regions of the compressor, resulting in a leakage loss. Aungier [46] suggested the following empirical relation to access this loss as

$$\Delta h_{lk} = \frac{\dot{m}_{lk} u_{lk} u_2}{2\dot{m}}, \tag{4.28}$$

  where

$$U_{lk} = 0.861 \sqrt{\frac{2\Delta P_{lk}}{\rho_2}}, \tag{4.29}$$

$$\Delta P_{lk} = \frac{\dot{m}(r_2 c_{2\theta} - r_{1s} c_{1s,\theta})}{0.25 N_{b,eff} L_{hyd} (r_{1s} + r_2)} (b_1 + b_2), \tag{4.30}$$

  and

$$\dot{m}_{lk} = \rho_2 U_{lk} N_b \varepsilon_t L_{hyd}. \tag{4.31}$$

  In the above equations, $u_{lk}, \dot{m}_{lk}$ and ΔP_{lk} are the velocity in the clearance gap, leakage mass flowrate and the pressure difference associated with the leakage, respectively.

4.6. Off design model

Given the geometry and inlet conditions, the compressor performance for varied mass flow and rotational speeds can be estimated using the loss models and exit conditions across each station as shown in figure 4.9.

The performance of the compressor can be written as

$$\text{Compressor performance } (\eta_{tt}, \beta_{tt}) = f(\dot{m}, N_{rpm}, P_{01}, T_{01}, \text{Geometry}). \tag{4.32}$$

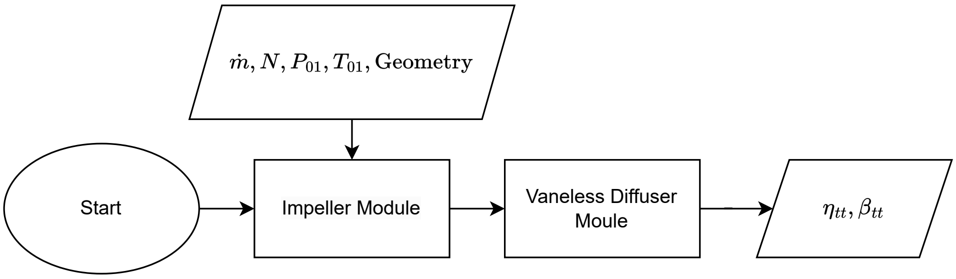
$\dot{m}, N, P_{01}, T_{01}$, Geometry
Start
Impeller Module
Vaneless Diffuser Moule
η_{tt}, β_{tt}

Figure 4.9: Compressor off-design calculation procedure.

4.6.1. Impeller inlet

Given the inlet conditions, the initial step involves iterating for the static conditions, as depicted in figure 4.10. Upon determining the static conditions, the rothalpy at the inlet is computed, and the analysis then proceeds to the subsequent block.

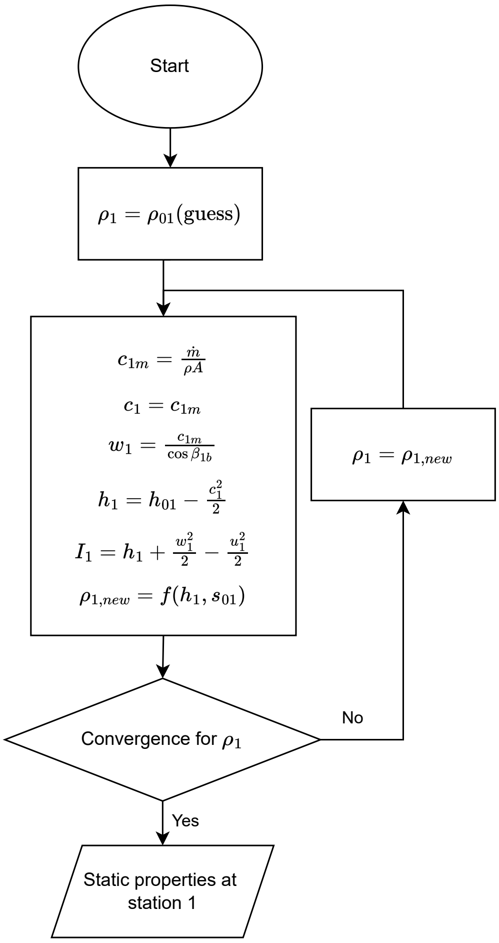
Start
$\rho_1 = \rho_{01}$(guess)
$c_{1m} = \frac{\dot{m}}{\rho A}$
$c_1 = c_{1m}$
$w_1 = \frac{c_{1m}}{\cos \beta_{1b}}$
$h_1 = h_{01} - \frac{c_1^2}{2}$
$I_1 = h_1 + \frac{w_1^2}{2} - \frac{u_1^2}{2}$
$\rho_{1,new} = f(h_1, s_{01})$
$\rho_1 = \rho_{1,new}$
Convergence for ρ_1
No
Yes
Static properties at station 1

Figure 4.10: Evaluation of static properties at impeller inlet.

4.6.2. Impeller outlet

The rotor analysis block follows the procedure in figure 4.11. To initialise the calculation procedure, an initial guess is made for the total-to-total pressure ratio (PR_{tt}) and total-to-total efficiency (η_{tt}) to estimate the compressor outlet state. As the blade angle β_{2b} is known, the ideal velocity triangle without slip can be constructed. Then, using the relation for slip in equa-

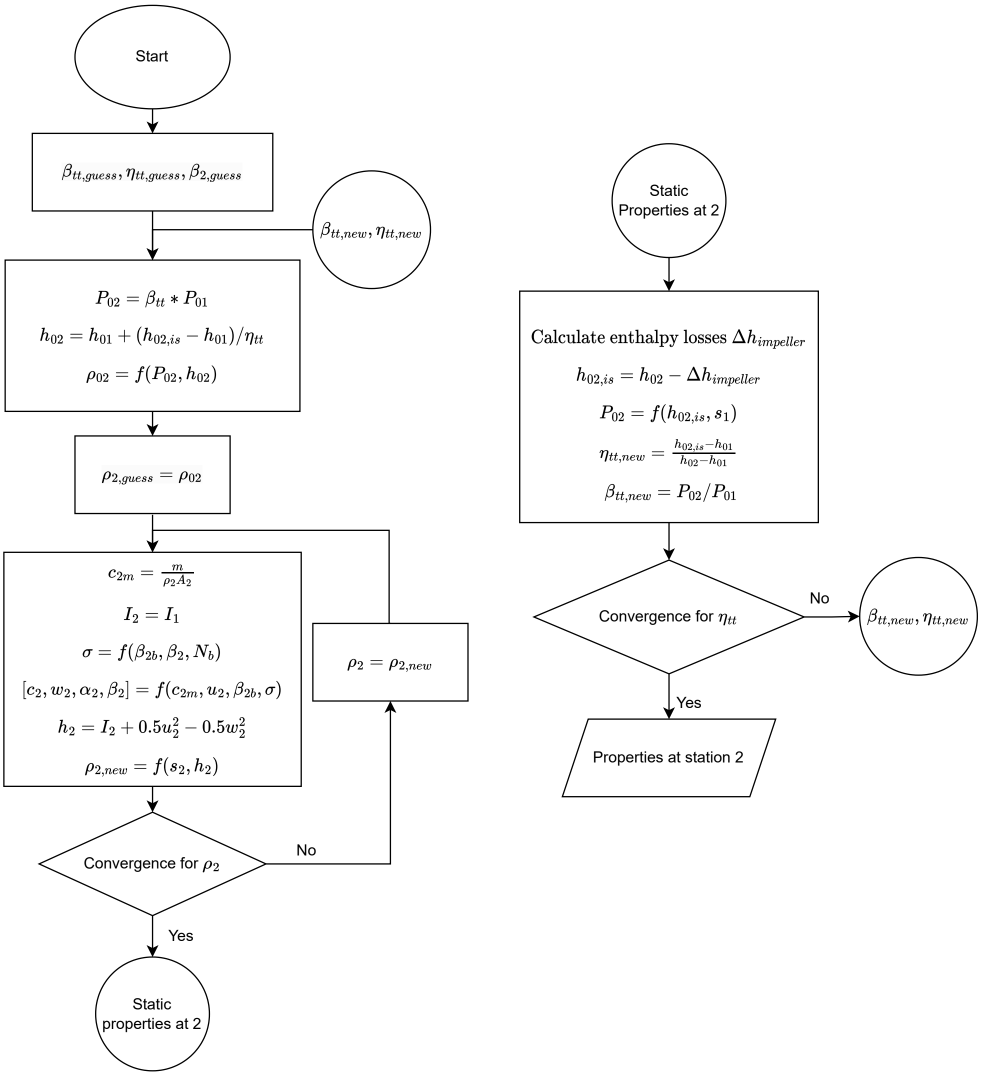
Start
$\beta_{tt,guess}, \eta_{tt,guess}, \beta_{2,guess}$
$\beta_{tt,new}, \eta_{tt,new}$
$P_{02} = \beta_{tt} * P_{01}$
$h_{02} = h_{01} + (h_{02,is} - h_{01})/\eta_{tt}$
$\rho_{02} = f(P_{02}, h_{02})$
$\rho_{2,guess} = \rho_{02}$
$c_{2m} = \frac{m}{\rho_2 A_2}$
$I_2 = I_1$
$\sigma = f(\beta_{2b}, \beta_2, N_b)$
$[c_2, w_2, \alpha_2, \beta_2] = f(c_{2m}, u_2, \beta_{2b}, \sigma)$
$h_2 = I_2 + 0.5u_2^2 - 0.5w_2^2$
$\rho_{2,new} = f(s_2, h_2)$
$\rho_2 = \rho_{2,new}$
Convergence for ρ_2
No
Yes
Static properties at 2
Static Properties at 2
Calculate enthalpy losses $\Delta h_{impeller}$
$h_{02,is} = h_{02} - \Delta h_{impeller}$
$P_{02} = f(h_{02,is}, s_1)$
$\eta_{tt,new} = \frac{h_{02,is} - h_{01}}{h_{02} - h_{01}}$
$\beta_{tt,new} = P_{02}/P_{01}$
Convergence for η_{tt}
No
$\beta_{tt,new}, \eta_{tt,new}$
Yes
Properties at station 2

Figure 4.11: Evaluation of properties at impeller outlet.

tion (4.3), the actual velocity triangle can be determined. Once the outlet velocity triangle is evaluated, the outlet static enthalpy h_2 can be determined. Now employing the loss relations from section 4.5, the guess values for P_{2t} and η_{tt} can be updated. Upon convergence of the impeller block, the analysis advances to the vaneless diffuser block.

4.6.3. Vaneless diffuser section

The flow within the vaneless space is primarily influenced by viscous effects and diffusion losses. To model this region, Stanitz [67] proposed the following set of one-dimensional governing equations that describe the compressible flow in this vaneless region.

- Continuity equation:

$$\frac{1}{\rho}\frac{d\rho}{dr} + \frac{1}{c_m}\frac{dc_m}{dr} + \frac{1}{b}\frac{db}{dr} + \frac{1}{r} = 0. \tag{4.33}$$

- Momentum equation in the meridional direction:

$$c_m\frac{dc_m}{dr} - \frac{c_\theta^2}{r} + c_f\frac{c^2\cos(\alpha)}{b} + \frac{1}{\rho}\frac{dp}{dr} = 0. \tag{4.34}$$

- Momentum equation in the tangential direction:

$$c_m \frac{dc_\theta}{dr} + \frac{c_m c_\theta}{r} + c_f \frac{c^2 \sin(\alpha)}{b} = 0. \tag{4.35}$$

- Conservation of total energy:

$$\frac{dh}{dr} + c_m \frac{dc_m}{dr} + c_\theta \frac{dc_\theta}{dr} = 0. \tag{4.36}$$

In these equations, c_f represents the friction factor, estimated by Japikse [42] as

$$c_f = k_{vl} \left(\frac{1.8 \cdot 10^5}{Re} \right)^{0.2}, \tag{4.37}$$

where k_{vl} is an empirical constant ranging from 0.005 to 0.02.

In the set of equations, there are four unknown variables, namely, $\rho, c_m, c_\theta,$ and p, while the value of h can be found using the equation of state, as $h = f(p, \rho)$. In order to solve the equation of state using Coolprop, the enthalpy is instead calculated as a function of its gradients with respect to pressure and density at each initial radial position as

$$dh = \left.\frac{\partial h}{\partial \rho}\right|_p d\rho + \left.\frac{\partial h}{\partial p}\right|_\rho dp. \tag{4.38}$$

As a result equation (4.36) can be now reformulated as

$$\left.\frac{\partial h}{\partial \rho}\right|_p \frac{d\rho}{dr} + \left.\frac{\partial h}{\partial p}\right|_\rho \frac{dp}{dr} + c_m \frac{dc_m}{dr} + c_\theta \frac{dc_\theta}{dr} = 0. \tag{4.39}$$

In order to solve this system of equations numerically, Agromayor et al. [68] expressed these equations in the matrix form as

$$A \frac{dU}{dr} = S, \tag{4.40}$$

where U is the solution vector, A is the coefficient matrix, and S is the source term vector, defined as

$$A = \begin{bmatrix} \frac{1}{c_m} & 0 & \frac{1}{\rho} & 0 \\ c_m & 0 & 0 & \frac{1}{\rho} \\ 0 & c_m & 0 & 0 \\ c_m & c_\theta & \left.\frac{\partial h}{\partial \rho}\right|_p & \left.\frac{\partial h}{\partial p}\right|_\rho \end{bmatrix}, \quad U = \begin{bmatrix} c_m \\ c_\theta \\ \rho \\ p \end{bmatrix}, \text{ and } S = \begin{bmatrix} \frac{-1}{b}\frac{db}{dr} - \frac{1}{r} \\ \frac{c_\theta^2}{r} - \frac{c_f c^2 \cos(\alpha)}{b} \\ \frac{-c_m c_\theta}{r} - \frac{c_f c^2 \sin(\alpha)}{b} \\ 0 \end{bmatrix}.$$

The vector $\frac{dU}{dr}$ can now be solved over small radial increments dr, from the outlet of the impeller to the exit of the vaneless space, using the ode45 solver from MATLAB [69].

4.6.4. Model validation

The validation of the meanline model against experimental data would test whether the modelling strategy and the loss models chosen are suitable to predict the compressor performance. However, achieving an exact match with experimental data might be challenging due to the semi-empirical nature of the loss models and errors related to experimental conditions and data recording.

For the model validation, cases from open literature have been chosen, where all geometric data and off-design performance maps were available. The first case chosen is the impeller 'O' by Eckardt [53, 54, 55], where a vaneless compressor is tested using air as the working fluid. The second case, an impeller by Schiffman and Favart [50, 51], was taken, where a vaneless compressor was tested with refrigerant R134a.

Table 4.1: Validation cases for centrifugal compressor.

Case	Pressure ratio	Working fluid
Eckardt impeller 'O'	1.5-2.5	Air
Schiffmann impeller	1.6-3.3	R134a

As mentioned in section 4.5, the loss models described are semi-empirical in nature. Thus, tuning parameters are used to improve the model's data fit. In the mixing loss equation (4.24), the values of ε_{max} and ε_{max} values are adjusted as the wake fraction is unknown apriori. Additionally, from equation (4.37), the value of k_{vl} in the vaneless diffuser has no definite relation and is thus used as a tuning parameter based on the range suggested by Japiske [42]. For validating the two compressor cases, the tuning parameters were arrived at using trial and error and are listed in table 4.2.

Table 4.2: Tuning parameters used for the validation cases.

Case	k_{vl}	$\varepsilon_{w,low}$	$\varepsilon_{w,choke}$
Eckardt Impeller 'O'	0.005	0.365	0.45
Schiffmann Impeller	0.011	0.365	0.5

Based on the inputs provided in table A.1, the off-design meanline model was utilized to generate performance charts by varying mass flowrate over different rotational speeds for the Eckardt and Schiffmann impellers as shown in figures 4.12 and 4.13 respectively. While running the off-design meanline code for the validation study, the following observations were made:

- Based on the loss distribution plots observed in both validation cases, some notable trends emerge. At lower mass flowrates, the recirculation losses dominate due to the high to higher values of α_2. At high mass flowrates, the mixing and disk friction losses exhibit a sharp increase in magnitude as they approach the onset of choking, displaying an exponential growth pattern. This introduces a considerable degree of variation in the total impeller loss across successive iterations in the context of the flowchart in figure 4.11, finally leading to an unconverged solution and the model's failure in the vicinity of the choking region. **This is a limitation of the meanline model developed in this work.**
- In the mixing loss model, the primary step involves estimating the choking point, which is used to set the flow rate corresponding to $\varepsilon_{wake,max}$. To generate the plots in figures

4.12 and 4.13, as the meanline model struggled to perform near the choke point, the maximum mass flowrate that still allowed a viable solution was utilized to establish the value of $\varepsilon_{wake,max}$.

- In the case of the Eckardt impeller in figure 4.12, there appears to be a good match between the model prediction and the experimental results, with a slight deviation at low speeds.
- In the case of the Schiffmann impeller 4.13, the model seems to capture the trend of the pressure ratio and efficiency curve. However, in this case, the solution was very sensitive to the tuning parameters and could not accurately predict the choking point. This led to a considerable deviation in the model prediction, leading to an overestimation of the efficiency, especially at high speeds.

Overall, these results show that the loss modelling approach used is suitable, and the same can be used for the design of compressors in the proceeding section.

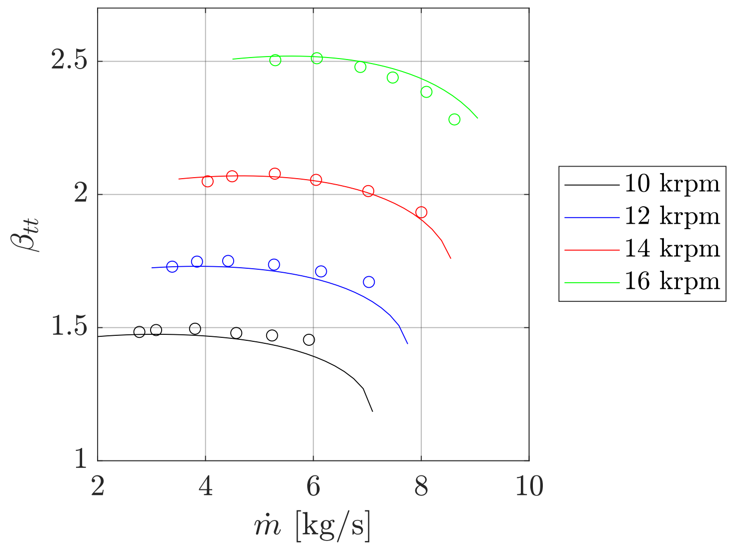

(a) Total-to-total pressure ratio vs mass flowrate. The experimental data is represented by circles, while the compressor model prediction is shown as a line.

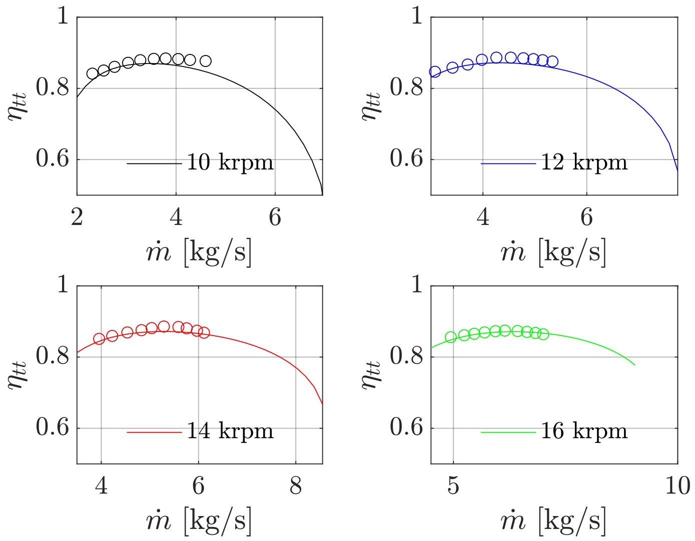

(b) Total-to-total efficiency vs mass flowrate. The experimental data is represented by circles, while the compressor model prediction is shown as a line.

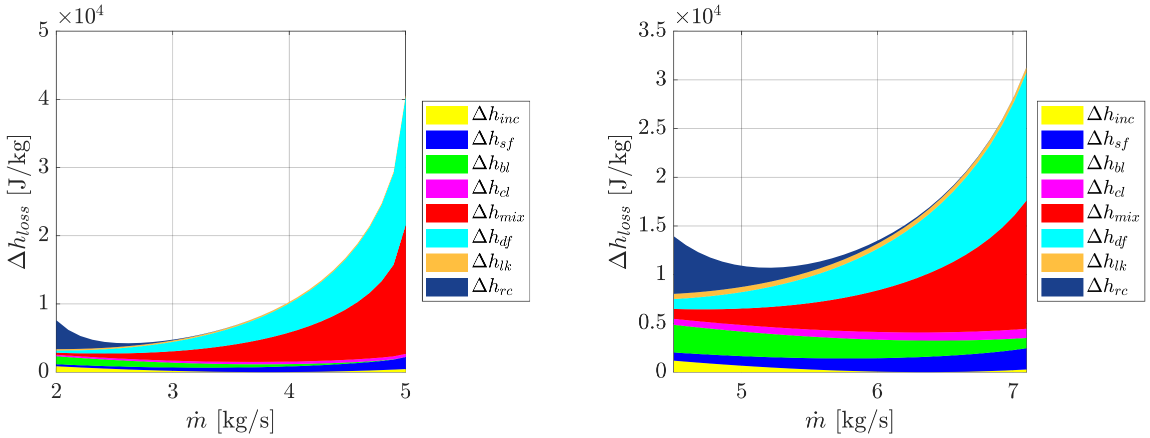

(c) Loss distribution for 10 krpm.

(d) Loss distribution for 16 krpm.

Figure 4.12: Comparison of meanline model vs experimental data of the Eckardt 'O' impeller

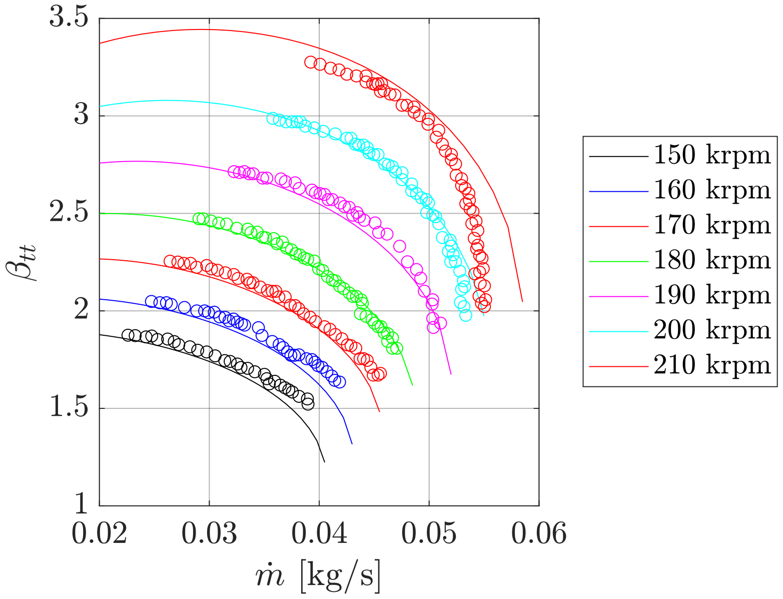

(a) Total-to-total pressure ratio vs mass flowrate. The experimental data is represented by circles, while the compressor model prediction is shown as a line.

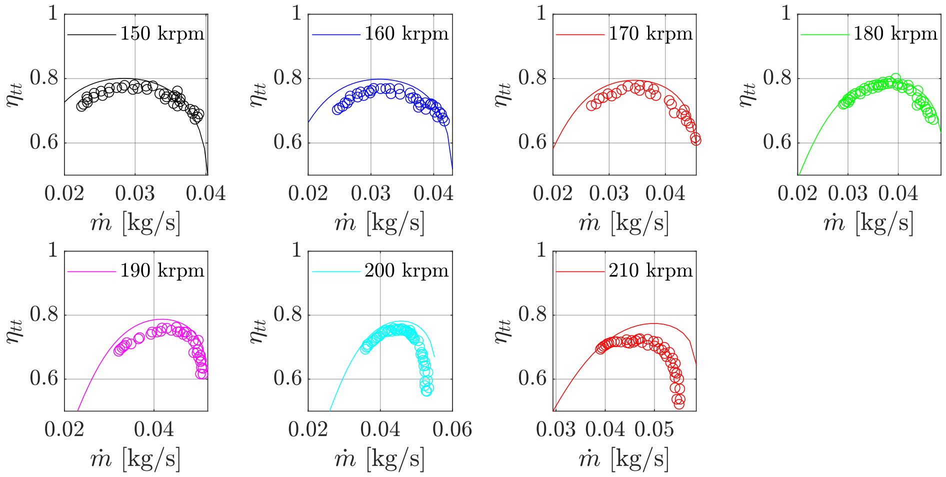

(b) Total-to-total efficiency vs mass flowrate. The experimental data is represented by circles, while the compressor model prediction is shown as a line.

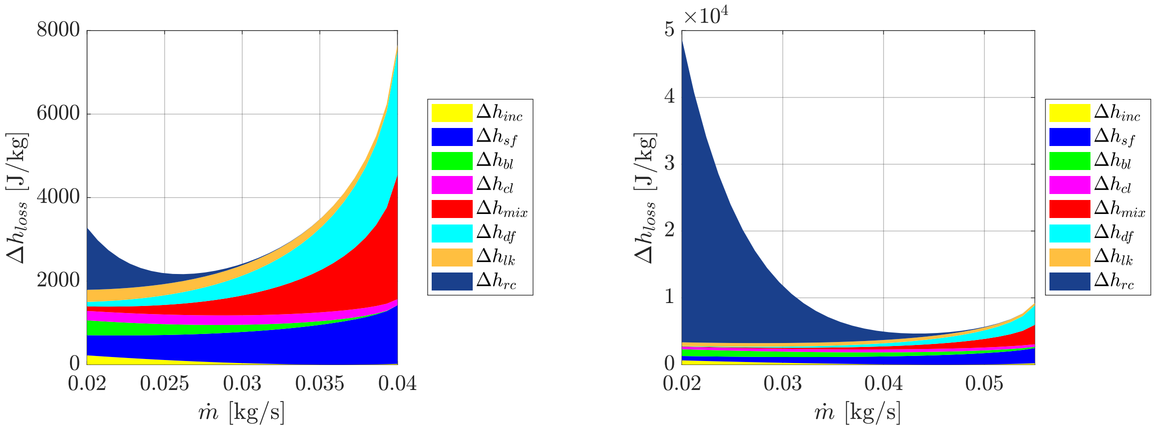

(c) 150 krpm case.

(d) 200 krpm case.

Figure 4.13: Comparison of meanline model vs experimental data of the Schiffmann impeller

4.7. Compressor meanline design model

The compressor design methodology is depicted in the flowchart provided below, and it is based on the works of Gambini and Vellini. [23], Giuffre et al, [38], Braembussche [47] and Meroni et al. [52].

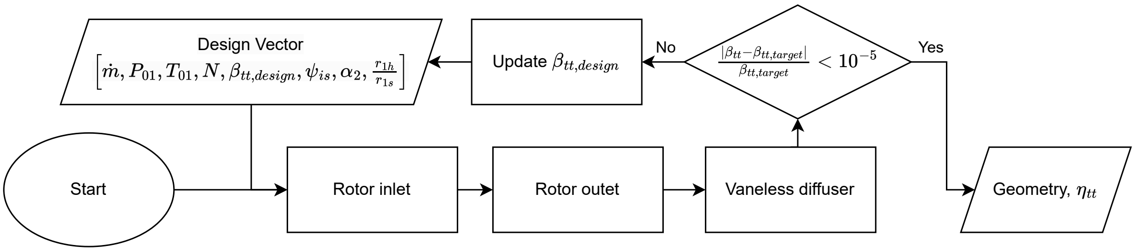
Design Vector
$\left[\dot{m}, P_{01}, T_{01}, N, \beta_{tt,design}, \psi_{is}, \alpha_2, \frac{r_{1h}}{r_{1s}}\right]$
Update $\beta_{tt,design}$
No
$\frac{|\beta_{tt}-\beta_{tt,target}|}{\beta_{tt,target}} < 10^{-5}$
Yes
Start
Rotor inlet
Rotor outlet
Vaneless diffuser
Geometry, η_{tt}

Figure 4.14: Compressor meanline design procedure.

Table 4.3 notes the inputs needed for the compressor design, using which a design vector can be formulated as shown in equation 4.41.

$$\textbf{Design Vector} = \left[\dot{m}, P_{01}, T_{01}, \beta_{tt,design}, N, \psi_{is}, \alpha_2, \frac{r_{1h}}{r_{1s}}\right] \tag{4.41}$$

Table 4.3: Input parameters for centrifugal compressor [23].

Parameter	Symbol	Unit	Range
Isentropic work coefficient	ψ_{is}	-	0.5-0.6
Hub to tip diameter ratio	r_{1h}/r_{1s}	-	0.2-0.7
Rotor outlet absolute flow angle	α_2	deg	65-80

4.7.1. Design of inlet section

The main design consideration in the rotor's inlet velocity triangle is the shroud radius [22]. From the inlet velocity triangle depicted in figure 4.3, it can be seen that at the tip, the blade speed, $\bar{u}$ and relative velocity $\bar{w}$ reach their maximum values. Now, for a given rotational speed and flow rate:

- If the shroud radius r_{1s} is too large, it results in a high u_{1s}, and consequently, a high value of w_{1s}.
- Conversely, if r_{1s} were too small, it increases the meridional velocity c_{1m}, which also increases w_{1s}.

Therefore, an optimal value of r_{1s} exists that minimizes the relative velocity and, consequently, the relative Mach number [22]. In this context, the approach put forth by Van den Braembussche [47] is adopted, wherein the radius ratio remains fixed, and the reduction of the Mach number is achieved by varying the inlet velocity, as demonstrated in figure 4.15. This approach guides the design of the compressor's inlet section, as outlined in figure 4.16.

4.7.2. Design of the rotor outlet

The design for the impeller continues according to figure 4.17. Here using the design pressure ratio and a guess value of the total to total efficiency (η_{tt}), the exit velocity triangle can be determined.

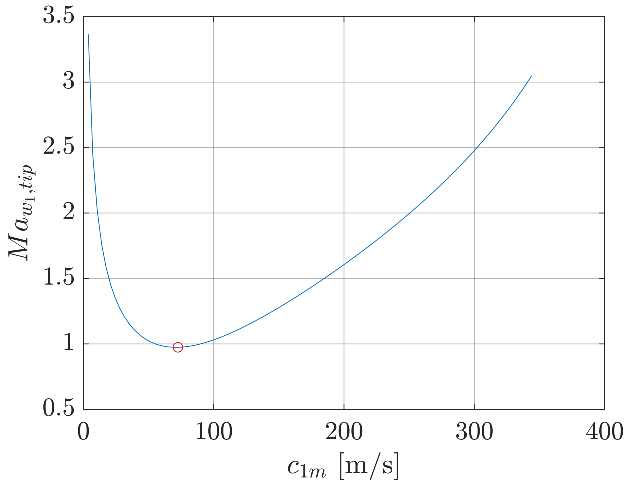

Figure 4.15: Variation of inlet tip Mach number vs meridional velocity. The red dot shows the selection point for minimisation.

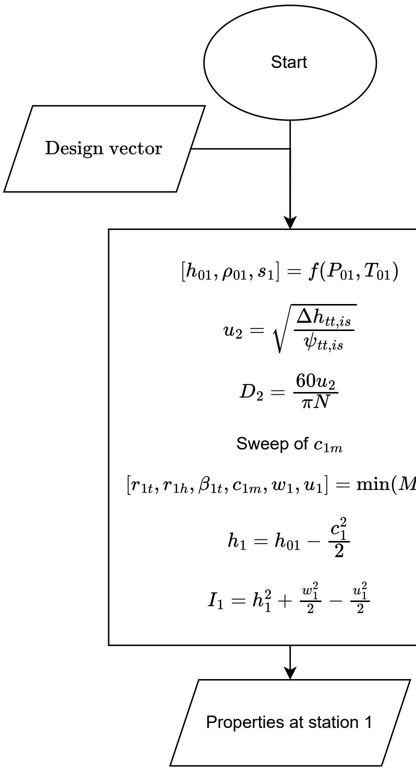
Start
Design vector
$[h_{01}, \rho_{01}, s_1] = f(P_{01}, T_{01})$
$u_2 = \sqrt{\frac{\Delta h_{tt,is}}{\psi_{tt,is}}}$
$D_2 = \frac{60u_2}{\pi N}$
Sweep of c_{1m}
$[r_{1t}, r_{1h}, \beta_{1t}, c_{1m}, w_1, u_1] = \min(Ma_{w_1})$
$h_1 = h_{01} - \frac{c_1^2}{2}$
$I_1 = h_1^2 + \frac{w_1^2}{2} - \frac{u_1^2}{2}$
Properties at station 1

Figure 4.16: Design procedure for compressor inlet.

The number of blades is an important parameter as it affects the slip in the compressor and the blockage effects. To find the number of blades, Meroni [52] and Gambini [23] use the empirical relation by Xu et al. [70] as

$$N_b = 12.03 + 2.544\beta_{tt}. \tag{4.42}$$

As the outlet velocity triangle is set, the blade angle β_{2b} that would lead to this velocity triangle is found using Wiesener's relation for slip as shown in equation (4.3). As the slip is a function

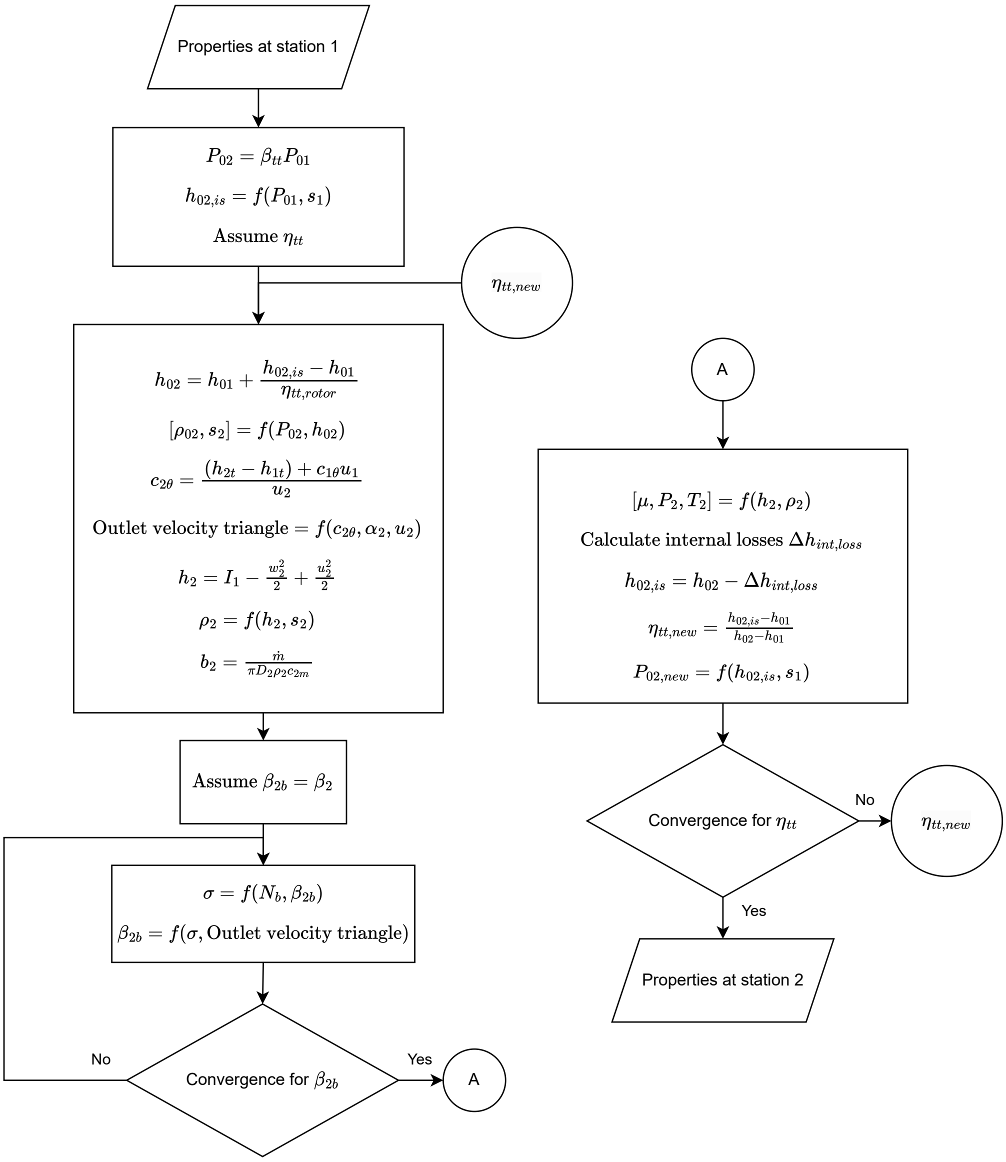
Properties at station 1
$P_{02} = \beta_{tt} P_{01}$
$h_{02,is} = f(P_{01}, s_1)$
Assume η_{tt}
$\eta_{tt,new}$
$h_{02} = h_{01} + \frac{h_{02,is} - h_{01}}{\eta_{tt,rotor}}$
$[\rho_{02}, s_2] = f(P_{02}, h_{02})$
$c_{2\theta} = \frac{(h_{2t} - h_{1t}) + c_{1\theta} u_1}{u_2}$
Outlet velocity triangle $= f(c_{2\theta}, \alpha_2, u_2)$
$h_2 = I_1 - \frac{w_2^2}{2} + \frac{u_2^2}{2}$
$\rho_2 = f(h_2, s_2)$
$b_2 = \frac{\dot{m}}{\pi D_2 \rho_2 c_{2m}}$
Assume $\beta_{2b} = \beta_2$
$\sigma = f(N_b, \beta_{2b})$
$\beta_{2b} = f(\sigma,$ Outlet velocity triangle$)$
No
Convergence for β_{2b}
Yes
A
A
$[\mu, P_2, T_2] = f(h_2, \rho_2)$
Calculate internal losses $\Delta h_{int,loss}$
$h_{02,is} = h_{02} - \Delta h_{int,loss}$
$\eta_{tt,new} = \frac{h_{02,is} - h_{01}}{h_{02} - h_{01}}$
$P_{02,new} = f(h_{02,is}, s_1)$
Convergence for η_{tt}
No
$\eta_{tt,new}$
Yes
Properties at station 2

Figure 4.17: Design procedure for compressor outlet.

of the blade angle, an iterative procedure is followed to find β_{2b}. However, following this procedure, the blade angle is 'adjusted' to meet the required velocity triangle, which may even lead to forward-swept blades, making the compressor operation unstable [43]. Following the steps in section B, a relationship between β_{2b} and the design inputs is arrived at as

$$\tan(\beta_{2b}) = \tan(\alpha_2) \left(\frac{\eta_{tt}}{\psi_{is}} - 1 \right) \left(1 - \frac{\cos(\beta_{2b})}{\left(1 - \frac{\psi_{is}}{\eta_{tt}}\right) N_b^{0.7}} \right). \tag{4.43}$$

This equation can be visualised as shown in figure 4.18 for a guess value of efficiency, and the number of blades from equation (4.42). Using this figure, a suitable choice of design inputs can be made to ensure backswept blades.

The remaining geometric quantities are determined from empirical relations. Aungier's relation [46] is used to determine the impeller length L_a as

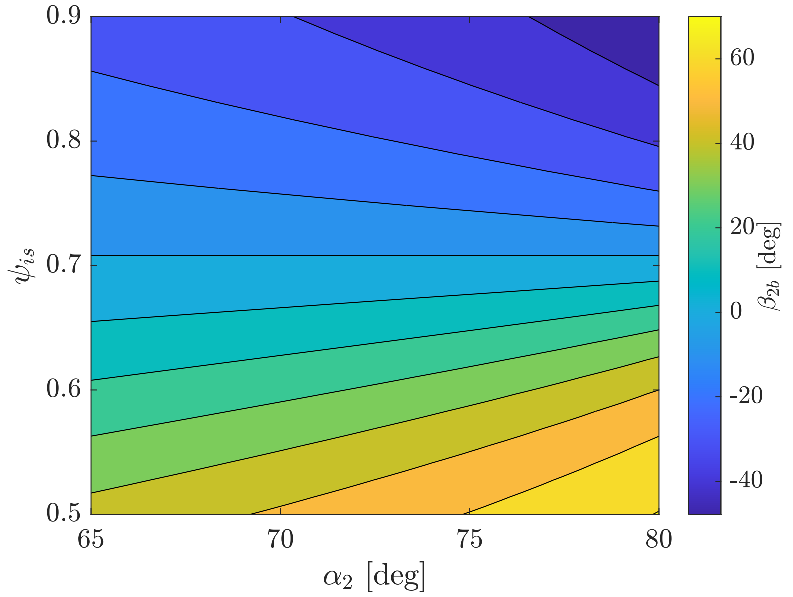

Figure 4.18: β_{2b} values for $\eta_{tt} = 80$% and N_b= 22.

$$L_a = D_2 \left[0.014 + \frac{0.023 r_2}{r_{1h}} + 1.58 \frac{c_{1m}}{u_2 r_2} (r_{1t}^2 - r_{1h}^2) \right]. \tag{4.44}$$

The values for blade thickness (t_b) and the impeller clearances (ϵ) are taken from guidelines by Gambini and Vellini [23] and are given as

$$t_b = 0.01 D_2, \tag{4.45}$$

and

$$\epsilon_{b,t} = 0.05 b_2. \tag{4.46}$$

With all the geometric parameters now defined for the rotor, the losses can be evaluated, and the analysis proceeds as shown in figure 4.17.

4.7.3. Design of the vaneless diffuser

As shown in the diagram 4.2, the vaneless diffuser is the space between stations 2 and 3. Its primary function is to smooth out the flow from the impeller exit and increase the static pressure through diffusion. Regarding its length, if the vaneless space is too small, insufficient pressure recovery takes place. Conversely, the frictional losses would be considerable if the vaneless region is too large. The diameter of the vaneless diffuser section is given by the following relation by Aungier [46]

$$D_3 = D_2 \left(1 + \frac{90^\circ - \alpha_3}{360^\circ} + \frac{Ma_2^2}{15} \right) \tag{4.47}$$

where,

$$\begin{aligned} \alpha_3 &= 72^\circ + \frac{\alpha_2 - 72^\circ}{4} && \text{if} \quad \alpha_2 \geq 72^\circ, \\ \alpha_3 &= 72^\circ && \text{if} \quad \alpha_2 < 72^\circ. \end{aligned} \tag{4.48}$$

The outlet with b_3 is assumed to equal the impeller outlet width. In some instances, a pinch ($b_3 < b_2$) is given at the vaneless diffuser to prevent the onset of stalling. Once the geometry is specified, the vaneless diffuser equation is solved as shown in section 4.6.3. At the end of the diffuser, the total and static conditions are determined. In an ideal case without losses, the total pressure at the outlet would be the same, but due to losses, $P_{03} < P_{02}$. Hence, the design pressure ratio is increased to account for this loss and achieve the compressor's target pressure ratio.

5

Radial inflow turbine

Typically, radial turbines are utilized in the range of a few kilowatts to a few megawatts and can handle high expansion ratios per stage up to 6 [30], and even up to 100 in case of organic Rankine cycles [71]. As mentioned in previous chapters, these turbines are robust and cost-effective, making them ideal for low-volume flowrate applications. Radial inflow turbines can also maintain high efficiency levels at off-design conditions by using variable stator vanes, a desired feature for PTES systems. However, organic fluids, such as R1233zd(E), have a low speed of sound characteristics, which can cause supersonic conditions in the stator and rotor. This poses a challenge in the design of such machines. The following sections present a one-dimensional meanline approach for the radial inflow turbine.

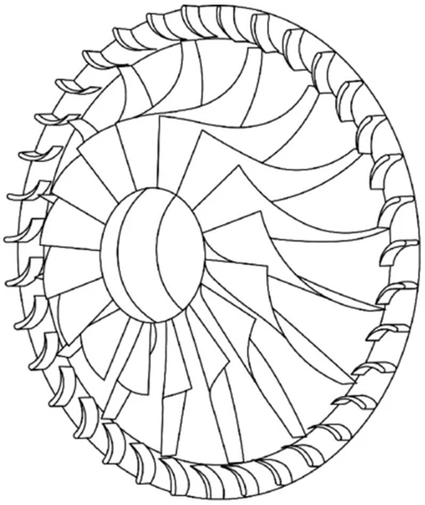

Figure 5.1: Radial inflow turbine [23].

5.1. Turbine stations

The radial inflow turbine consists mainly of a casing, stator vanes, a rotor, and a diffuser tube. Pressurised fluid entering the volute is distributed across the stator blades. The stators are designed such that the relative flow velocity is optimal at the rotor inlet for minimal losses. The rotor blades then guide the fluid radially inward from the rotor inlet to turn 90°to an outlet in the axial direction. In this work, the casing and diffuser tube sections are not considered. From figure 5.2, the turbine stations are

- 1-3: Nozzle section
- 3-4: Interspace region
- 4-6: Rotor section

Stations 2 and 5 are the intermediate stations for the nozzle and rotor throats respectively and are not considered in this analysis.

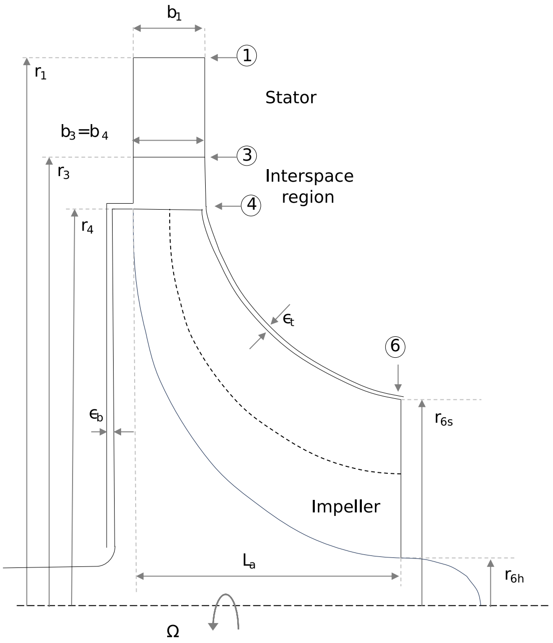
b_1
①
r_1
Stator
$b_3=b_4$
③
r_3
Interspace region
④
r_4
ϵ_t
⑥
ϵ_b
r_{6s}
Impeller
L_a
r_{6h}
Ω

Figure 5.2: Radial inflow turbine stations and naming convention for this thesis.

5.2. Velocity triangles

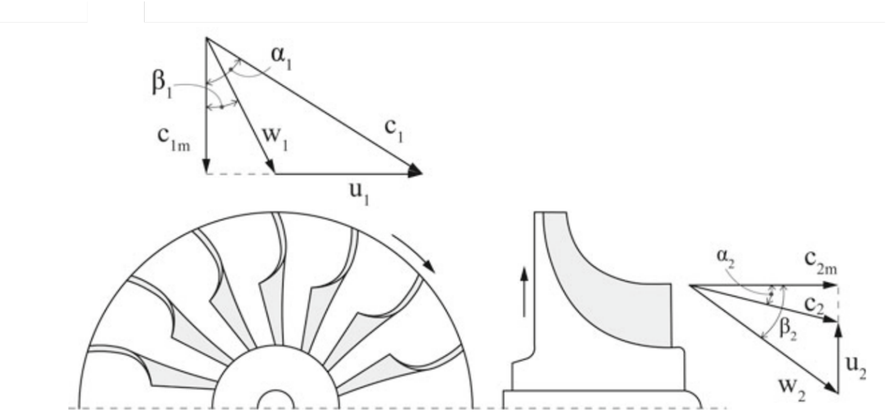
α_1
β_1
c_{1m}
w_1
c_1
u_1
α_2
c_{2m}
c_2
β_2
u_2
w_2

Figure 5.3: Velocity triangles at rotor inlet and outlet [23]. Here, subscripts 1 and 2 refer to the rotor inlet and exit, respectively

Figure 5.3 shows the inlet and outlet velocity triangles for the turbine. Following the same naming convention as the figure, from the Euler equation, the work across the turbine stage is due to the large difference in the peripheral velocities at the inlet and outlet and is given by

$$\Delta W = h_{01} - h_{02} = u_1 c_{\theta 1} - u_2 c_{\theta 2} = \frac{1}{2}\left[u_1^2 - u_2^2) - (w_1^2 - w_2^2) + (c_1^2 - c_2^2)\right] \tag{5.1}$$

From a similar derivation as equation 4.8, the rothalpy of the turbine is given as

$$I = h_1 + \frac{1}{2}(w_1^2 - u_1^2) = h_2 + \frac{1}{2}(w_2^2 - u_2^2) \tag{5.2}$$

The Mollier diagram for the turbine is given in figure 5.4. Across the nozzle and interspace sections, the total enthalpy stays constant. In the rotor section, as shown in equation 5.2, the rothalpy remains constant. For RITs, the spouting velocity is often used as a design parameter. It is defined as the velocity that is associated with an isentropic enthalpy drop from the turbine inlet stagnation pressure p_0 to the exit static pressure p_2 [22], and is given by

$$c_s = 2(h_{0t} - h_{2is}). \tag{5.3}$$

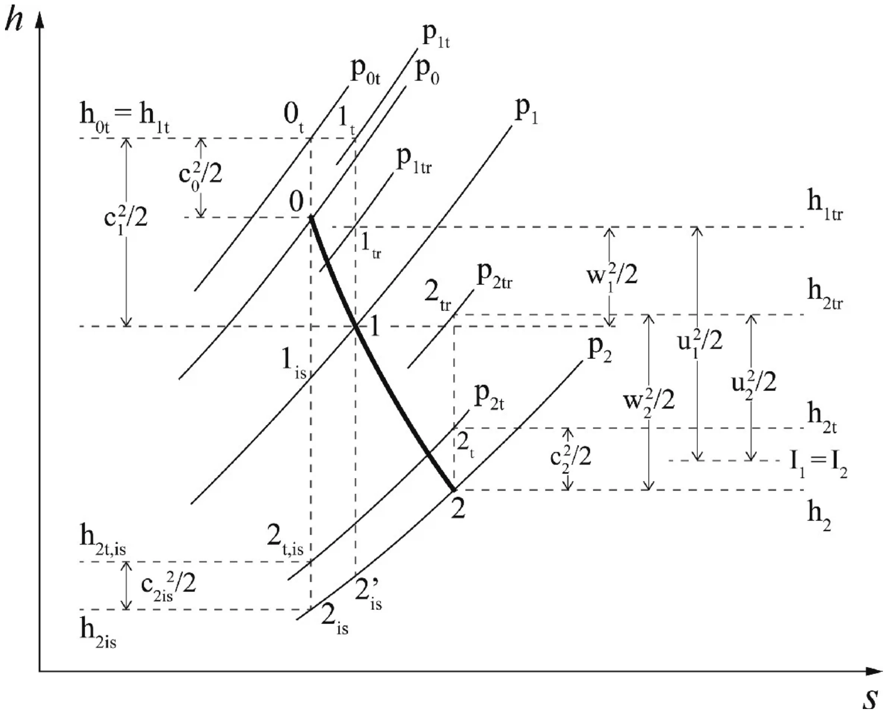

Figure 5.4: Mollier diagram for radial infow turbines [23].

5.3. Turbine performance characteristics

At off-design characteristic of a turbine can be seen in figure 5.5. At high-pressure ratios, choking conditions can be reached at either the stator or rotor imposing a maximum mass flow rate through the turbine, which is independent of the rotational speed [29].

5.4. Meanline models in literature

Bahamonde et al. [72] in their work describe an integrated approach, combining the cycle performance and the meanline design of the turbine. An in-house meanline tool called 'zTurbo' was used to evaluate design spaces for axial, radial inward flow and radial outflow turbines, based on input conditions and constraints from the thermodynamic cycle. In particular, their

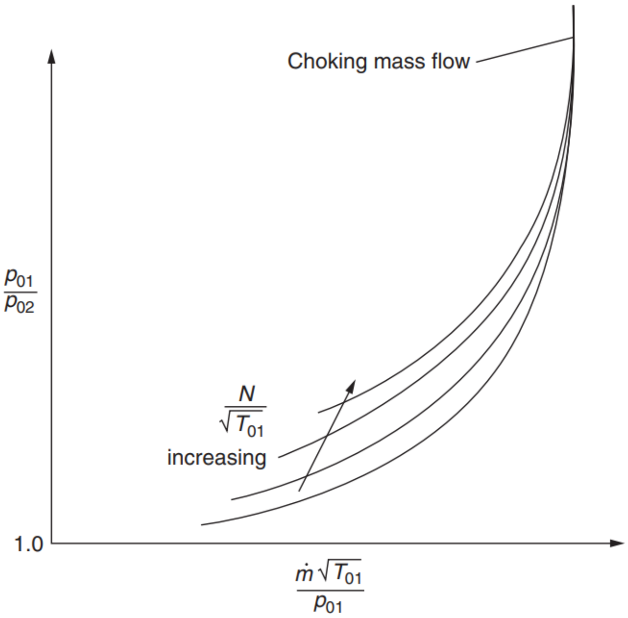

Figure 5.5: Performance map of a high speed turbine [22].

method dealt with high-pressure ratios of 72, and high temperature (sub and supercritical conditions for a 10kW test rig. The optimisation was then carried out to obtain maximum system efficiency and the turbine efficiency is a result of the meanline design. The loss models used were mentioned, but no description of the design methodology of the radial inflow turbine was given. The authors also note that most of the loss models used were developed using turbines operating with fluids whose thermodynamic state was close to the ideal gas assumption and with low expansion ratios. Under high-temperature conditions, the validity of the loss correlations was uncertain and further CFD and tests could be used to calibrate these models for high-temperature cases.

Mernoi et al [31] presented a meanline approach for radial turbines operating at high-pressure ratios (up to 5.8). The authors presented an approach for the design and off-design modelling and validated the same against experimental results. Experimental data of six RITs from the literature was used to calibrate the loss models used to match the meanline model and experimental data, and an optimisation-based calibration method to redefine the loss models. Two additional experimental cases were used to assess the validity of the calibration done. Meroni also considered the nozzle losses in detail and modelled the stator space and nozzle rotor interspace separately.

Lio et al. [73] presented a mean-line model of a radial turbine for an ORC system using R245fa as a working fluid. The authors gave a detailed overview of the design and off-design procedure followed based on loss correlations by Aungier [74]. The authors also provide a breakdown of the various loss contributions at different specific speeds and speed ratios ν_s (defined as the ratio of rotor inlet peripheral velocity u_2 to spouting velocity c_s). Usually, the speed ratio is taken as 0.7 as it leads to a minimisation of losses [22]. In addition, performance maps were generated showing the effect of specific speed and speed ratio on the efficiency. Regarding the design choices, the authors note that a specific speed of 0.4 is optimal, and for high expansion ratios, as in the case of ORCs, the $\nu_s = 0.6$ leads to a minimisation of losses.

Schustera et al. [75] Presented an approach for optimisation of sub and transcritical ORCs for design and off-design cases using a meanline model. The results were validated against two experimental cases from the literature and also using CFD results. The authors also give an approach for varying the nozzle vane positions to extend the operating range and improve performance at off-design conditions. An optimisation was done using a MATLAB optimiser 'fmincon' [76] to find the optimal set of design parameters for the best total to total isentropic efficiency. Although high-pressure ratios have been found in the literature, the authors note that pressure ratios above 4 can lead to supersonic conditions at the nozzle. Addressing these conditions often demands unconventional design methods, especially since such high-pressure ratios can result in efficiency reductions due to significant nozzle losses. They also state that multiple turbine stages are also useful for extending the cycle pressure ratios. From the point of a PTES system, this could take place if there is a variation in the storage or ambient temperatures.

5.5. Loss models

In literature, many loss models and combinations are available. Similar to the compressor case, these losses can be expressed in terms of pressure losses or static enthalpy losses. Again, enthalpy-based loss models are favoured as they are more commonly encountered in literature as done by Meroni et al [31] and Manfredi et al [77]. Aungier [74] presented a set of pressure-based loss for turbines as well, and the same has been implemented in the works of Lio et al. [73] for the development of their meanline tool. In this work, the loss model combination used by Meroni [31] is used, as a good fit with experimental data was found.

5.5.1. Rotor loss models

The losses taking place in the rotor are illustrated in figure 5.6 and are given as follows:

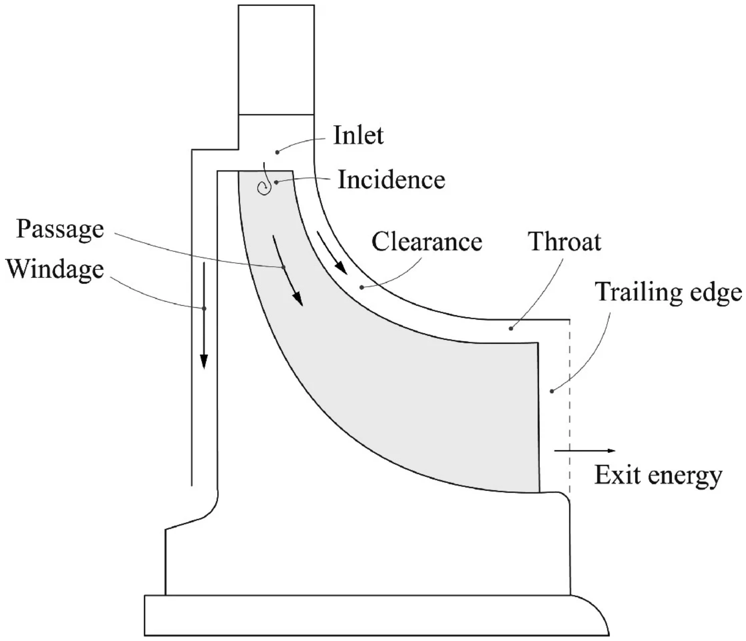

Figure 5.6: Rotor losses in a radial turbine [23].

- Incidence loss (Δh_{inc}): Occurs due to the difference between the inlet relative flow angle and the optimal flow angle. The flow angle for optimum efficiency is significantly different from zero incidence [22], and can be up to 20°- 40°higher than the rotor blade angle [78]. As shown in figure 5.7. There is some incidence angle that provides optimum flow conditions.

This effect can be explained using the relative eddy concept, similar to the case of 'slip' in centrifugal compressors. Considering the case where the rotor rotates at an angular velocity Ω, and assuming that the fluid entering is irrotational, the fluid will gain a counter-rotating vortex, or a relative eddy opposite to the rotor, in order to conserve its irrotational state [22].

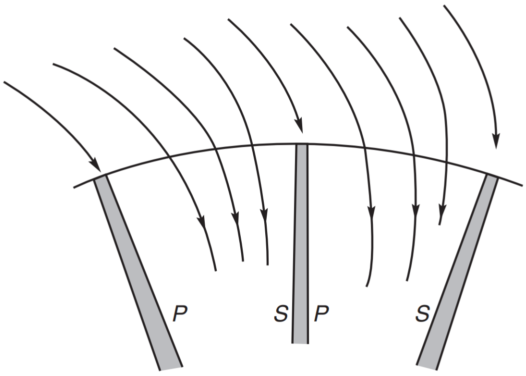

Figure 5.7: Optimal inflow conditions at the rotor inlet ("p" denotes the pressure surface, and "s" represents the suction surface) [22].

.

At off-design conditions, the incidence loss can become quite significant. The relation by Wasserbauer and Glassman [79] is used for the evaluation of these losses as:

$$\Delta h_{\text{inc}} = \frac{w_4^2}{2}\sin^2\left(\beta_4 - \beta_{4,\text{ opt}}\right), \tag{5.4}$$

where,

$$\tan\beta_{4,opt} = \frac{0.63\pi u_4}{N_{b,rotor}c_{4m}}. \tag{5.5}$$

- Passage loss ($\Delta h_{passage}$): Represents the loss generated as the flow passes through the rotor blade passage. It takes into account secondary flow effects, frictional losses generated due to viscosity, and losses occurring due to flow separation [78]. The loss relation by Whitfield and Baines [49] is used to evaluate this loss as

$$\Delta h_{passage,rotor} = K_p\left(\left(\frac{L_{hyd,R}}{D_{hyd,R}}\right) + 0.68\left(1 - \left(\frac{D_{6,mid}}{D_4}\right)^2\right)\frac{\cos\beta_{6b,mid}}{(b_6/c_r)}\right)\frac{w_4^2 + w_{6,mid}^2}{2} \tag{5.6}$$

where,

$$\begin{aligned} K_p &= 0.11 \quad \text{, if } \frac{D_4 - D_{6t}}{2b_6} \geq 0.2, \\ K_p &= 0.22 \quad \text{, if } \frac{D_4 - D_{6t}}{2b_6} < 0.2, \end{aligned} \tag{5.7}$$

and c_r is the rotor blade chord approximated as

$$c_r = \frac{N_b}{\cos(\tan^{-1}(0.5(\beta_{4b} + \beta_{6,mid})))}. \tag{5.8}$$

The hydraulic length is defined using the relation by Gambini [23] as:

$$L_{hyd,rotor} = \frac{\pi}{8}(2L_a - b_4 + D_4 - D_{6t} + b_6). \tag{5.9}$$

For the hydraulic diameter, the relation by Gambini [23] was used:

$$D_{hyd,rotor} = \frac{O_4 b_4}{O_4 + b_4} + \frac{O_6 b_6}{O_6 + b_6}, \tag{5.10}$$

where,

$$O_4 = \frac{\pi D_4}{N_{b,r}} \cos \beta_{4b}, \tag{5.11}$$

and

$$O_6 = \frac{piD_{6,mid}}{N_{b,r}} \cos \beta_{6b,mid}. \tag{5.12}$$

- Trailing edge loss ($\Delta h_{te,rotor}$): These losses primarily occur because of the creation of wakes and the subsequent mixing processes that occur downstream of the blade's trailing edge. The relation by Glassman [80] has been used as:

$$\Delta h_{te,rotor} = \frac{1}{2} w_{6,mid}^2 \left(\frac{N_{b,rotor} t_{te}}{\pi D_{6,mid} \cos \beta_{6,mid}} \right)^2 \left(1 + \frac{\gamma_6 - 1}{2} Ma_6^2 \right)^{\frac{\gamma_6}{1-\gamma_6}}. \tag{5.13}$$

- Clearance loss (Δh_{cl}): Loss due to the mixing of flows in the mechanical clearance between the rotor blades and casing. The relation by Baines [81] is used as

$$\Delta h_{cl} = \frac{u_4^3 N_{b,rotor}}{8\pi} \left(K_a \epsilon_a C_a + K_r \epsilon_r C_r + K_{a,r} \sqrt{\epsilon_a C_a \epsilon_r C_r} \right), \tag{5.14}$$

where

$$C_a = \frac{\left(1 - \frac{D_{6t}}{D_4}\right)}{c_{4m} b_4}, \tag{5.15}$$

and

$$C_r = 2\frac{D_{6t}}{D_4} \left(\frac{L_a - b_4}{c_{6m} D_{6,mid} b_6} \right). \tag{5.16}$$

Also, the coefficients K_a, K_r, and $K_{a,r}$ are equal to 0.4, 0.75 and -0.3, respectively.

- Windage loss ($\Delta h_{windage}$): They represent losses due to disc friction similar to that of centrifugal compressors, and the same relation by Daily and Nece [66] as shown in equation (4.26)
- Exit energy loss (Δh_{exit}): This loss is associated with the kinetic energy at the outlet of the rotor and is given as

$$\Delta h_{exit} = \frac{1}{2} c_6^2. \tag{5.17}$$

5.5.2. Stator loss models

In a similar manner to the rotor, the passage and trailing edge losses in the stator section are given by the following relations:

- Nozzle passage loss: The relation by Rodgers [82] is used as:

$$\Delta h_{passage,stator} = \frac{0.05}{Re_3^{0.2}}\left(\frac{3\tan\alpha_3}{S_{3,s}/C_s} + \frac{S_{3,s}\cos\alpha_3}{b_3}\right)\frac{c_3^2}{2}, \tag{5.18}$$

where

$$C_s = \frac{D_1 - D_3}{2\cos(0.5\alpha_1)}, \tag{5.19}$$

and

$$S_{3,s} = \frac{\pi D_1}{N_{b,s}}. \tag{5.20}$$

- Nozzle trailing edge loss: the relation by Glassman [80] is used as:

$$\Delta h_{te,stator} = \frac{c_3^2}{2}\left(\frac{N_{b,s}t_3}{2\pi r_3\cos\alpha_3}\right)^2\left(1 + \frac{\gamma_3 - 1}{2}Ma_3^2\right)^{\frac{\gamma_3}{1-\gamma_3}} \tag{5.21}$$

5.6. Off design model

The meanline methodology presented in this section is based on the works of Gambini and Vellini [23], Moustapha[78], and Meroni [31]. In a similar manner to the compressor, the performance of the turbine can be obtained for a set of operational parameters and geometry as

$$\text{Turbine performance } (\eta_{ts}, \beta_{ts}) = f(\dot{m}, N, P_{01}, T_{01}, \text{Geometry}). \tag{5.22}$$

Using the loss models from section 5.5, the solution procedure for estimating the performance follows the figure 5.8. The following sections explain the solution procedure in each module.

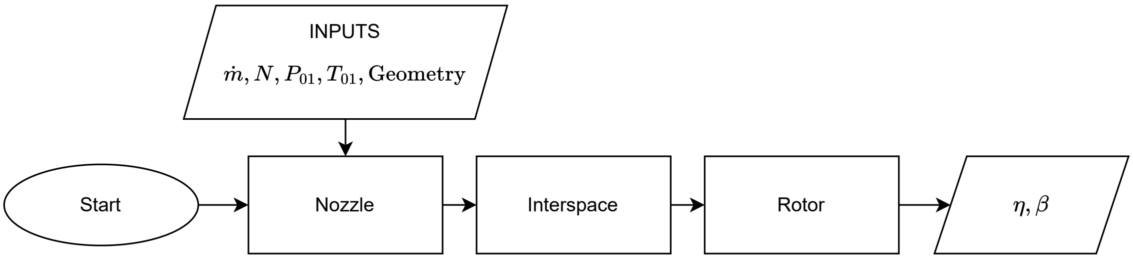

Figure 5.8: Turbine off-design flowchart.

5.6.1. Nozzle section

The solution procedure for the nozzle section is shown in figure 5.9. Given the geometry and stagnation thermodynamic conditions at the inlet, the first step for the nozzle section involves evaluating the inlet's static thermodynamic properties as shown in figure 5.9a. For the nozzle exit conditions, a guess value is made for the exit density, and it is assumed that the flow follows the blade angle without deviation.

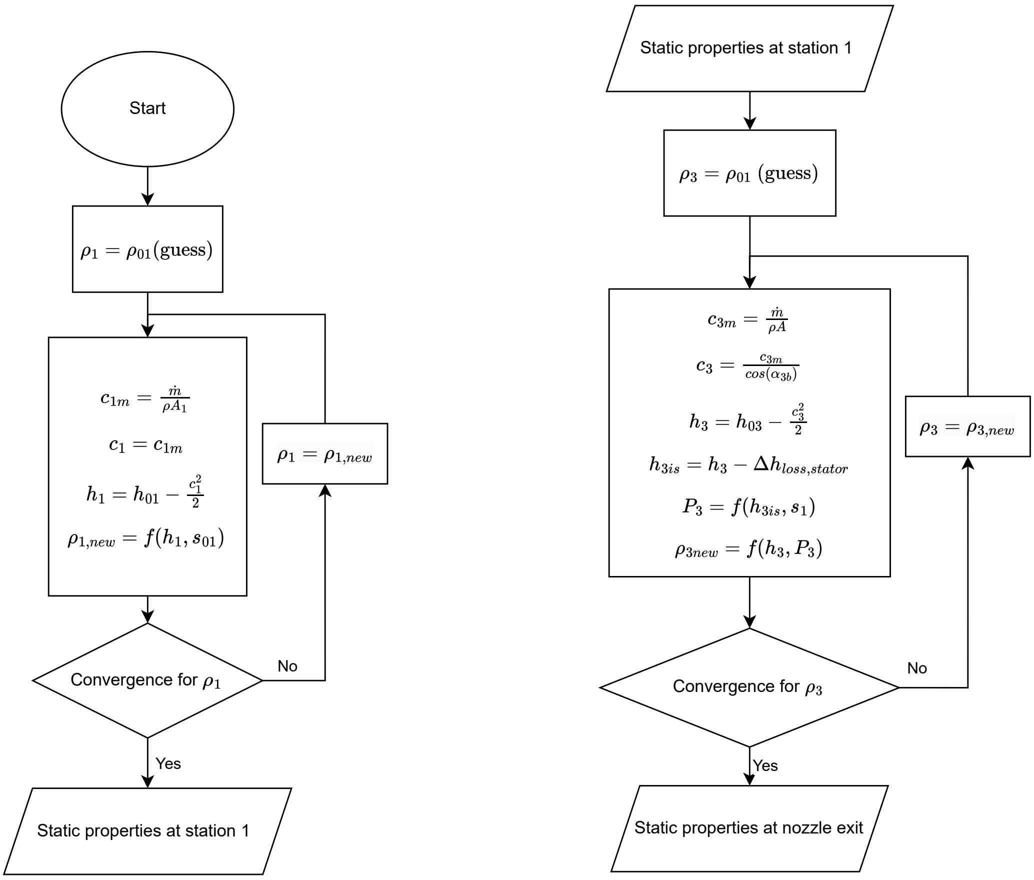
Start
$\rho_1 = \rho_{01}$(guess)
$c_{1m} = \frac{\dot{m}}{\rho A_1}$
$c_1 = c_{1m}$
$h_1 = h_{01} - \frac{c_1^2}{2}$
$\rho_{1,new} = f(h_1, s_{01})$
$\rho_1 = \rho_{1,new}$
Convergence for ρ_1
No
Yes
Static properties at station 1
Static properties at station 1
$\rho_3 = \rho_{01}$ (guess)
$c_{3m} = \frac{\dot{m}}{\rho A}$
$c_3 = \frac{c_{3m}}{cos(\alpha_{3b})}$
$h_3 = h_{03} - \frac{c_3^2}{2}$
$h_{3is} = h_3 - \Delta h_{loss,stator}$
$P_3 = f(h_{3is}, s_1)$
$\rho_{3new} = f(h_3, P_3)$
$\rho_3 = \rho_{3,new}$
Convergence for ρ_3
No
Yes
Static properties at nozzle exit

(a) Evaluation of nozzle inlet conditions.

(b) Evaluation of nozzle exit conditions.

Figure 5.9: Evaluation of thermodynamic properties in the nozzle section

5.6.2. Interspace region

The region between the rotor and nozzle, known as the interspace region, is often neglected, and the outlet conditions from the nozzle are assumed to represent the inlet conditions for the rotor, as adopted by Dixon and Hall[22] and Gambini and Vellini[23]. For modelling the flow within this interspace region, Whitfield [49] provided the following set of equations.

- Conservation of mass:

$$\dot{m} = \rho_4 c_4 \cos \alpha_4 2\pi r_4 b_4. \tag{5.23}$$

- Conservation of energy:

$$h_{04} = h_4 + \frac{c_4^2}{2}, \tag{5.24}$$

  and

$$h_4 = h(p_4, s_3) + \Delta h_{interspace}. \tag{5.25}$$

- Conservation of angular momentum:

$$\frac{c_3 \sin \alpha_3}{c_4 \sin \alpha_4} = \frac{r_4}{r_3} + \frac{2\pi \left(r_3^2 - r_3 r_4\right) c_f \rho_4 c_4 \sin \alpha_4}{\dot{m}}, \tag{5.26}$$

  where c_f is a friction factor coefficient and is evaluated similarly to that of the compressor's vaneless space, according to equation (4.37).

The above set of equations has four unknowns, namely α_4, ρ_4, p_4 and c_4. The enthalpy h is evaluated from the equation of state as $h = f(p, \rho)$. The solution procedure for the interspace region is carried out as outlined in the flowchart in figure 5.10. Achieving convergence requires an iterative approach and is initialised with a guess value for ρ_4 and α_4. First, these equations are solved under an isentropic assumption, disregarding losses and setting the friction coefficient to zero. After convergence is reached under these conditions, the isentropic results serve as initial guesses for solving the set of equations, considering losses and frictional effects.

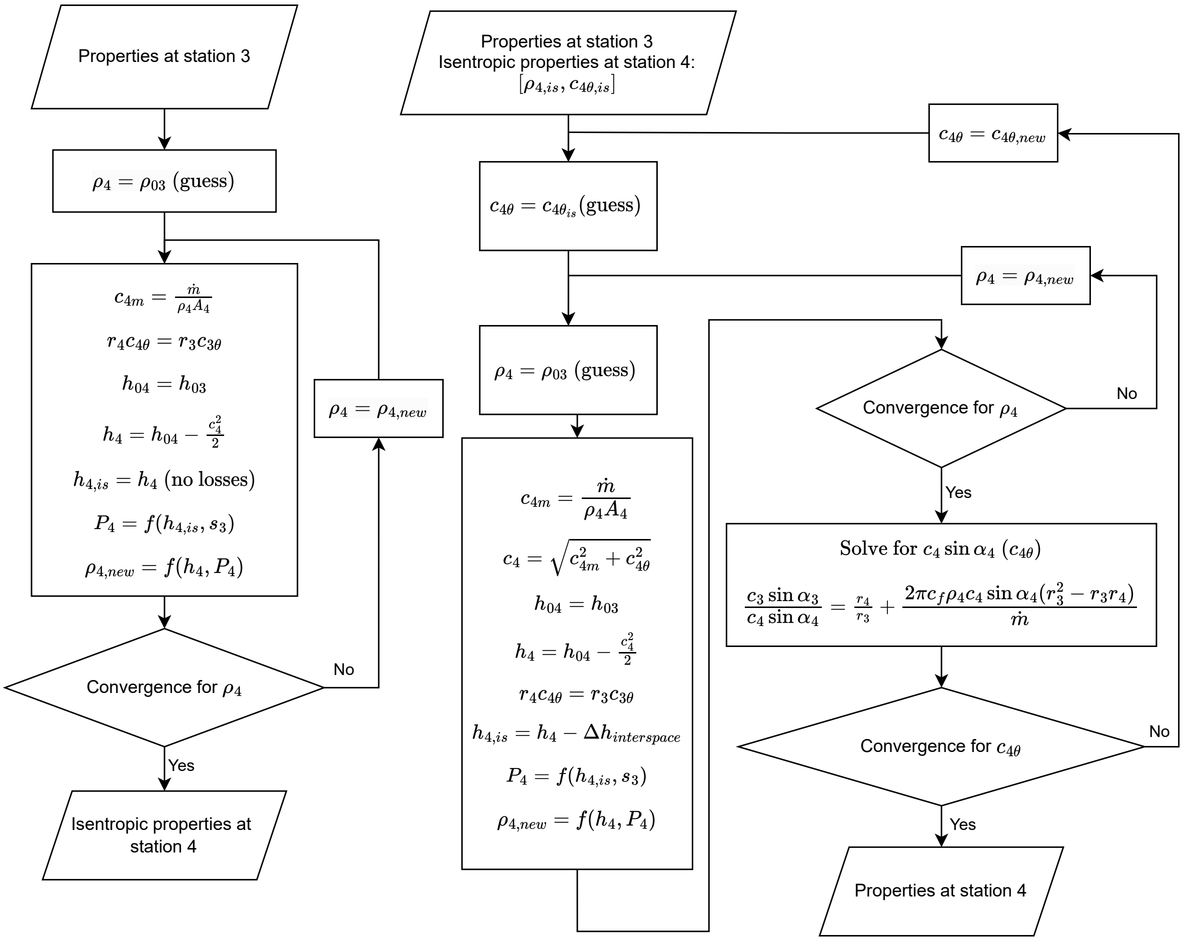
Properties at station 3
$\rho_4 = \rho_{03}$ (guess)
$c_{4m} = \frac{\dot{m}}{\rho_4 A_4}$
$r_4 c_{4\theta} = r_3 c_{3\theta}$
$h_{04} = h_{03}$
$h_4 = h_{04} - \frac{c_4^2}{2}$
$h_{4,is} = h_4$ (no losses)
$P_4 = f(h_{4,is}, s_3)$
$\rho_{4,new} = f(h_4, P_4)$
$\rho_4 = \rho_{4,new}$
Convergence for ρ_4
No
Yes
Isentropic properties at station 4
Properties at station 3
Isentropic properties at station 4:
$[\rho_{4,is}, c_{4\theta,is}]$
$c_{4\theta} = c_{4\theta,new}$
$c_{4\theta} = c_{4\theta_{is}}$(guess)
$\rho_4 = \rho_{4,new}$
$\rho_4 = \rho_{03}$ (guess)
$c_{4m} = \frac{\dot{m}}{\rho_4 A_4}$
$c_4 = \sqrt{c_{4m}^2 + c_{4\theta}^2}$
$h_{04} = h_{03}$
$h_4 = h_{04} - \frac{c_4^2}{2}$
$r_4 c_{4\theta} = r_3 c_{3\theta}$
$h_{4,is} = h_4 - \Delta h_{interspace}$
$P_4 = f(h_{4,is}, s_3)$
$\rho_{4,new} = f(h_4, P_4)$
Convergence for ρ_4
No
Yes
Solve for $c_4 \sin\alpha_4$ ($c_{4\theta}$)
$\frac{c_3 \sin\alpha_3}{c_4 \sin\alpha_4} = \frac{r_4}{r_3} + \frac{2\pi c_f \rho_4 c_4 \sin\alpha_4 (r_3^2 - r_3 r_4)}{\dot{m}}$
Convergence for $c_{4\theta}$
No
Yes
Properties at station 4

Figure 5.10: Evaluation of properties in the interspace region.

5.6.3. Rotor section

The procedure for the rotor section is outlined in figure 5.11. To evaluate the properties of the rotor exit, guess estimates are made for the efficiency and pressure ratio is made, which are updated after the evaluation of the rotor losses. Also, at the rotor exit, it is assumed that the flow follows the blade angle.

5.7. Validation case

For the validation of the meanline code, the McLallin radial turbine [83] operating with air was chosen, as all geometric details of the turbine and off-design performance data were available. Similarly to the compressor case, the friction factor coefficient, denoted as k_{vl}, was treated as a tuning parameter, and a value of $k_{vl} = 0.1$ was utilized. Following the off-design procedure and using the model inputs from table A.2, figure 5.12 was generated. From these results, the

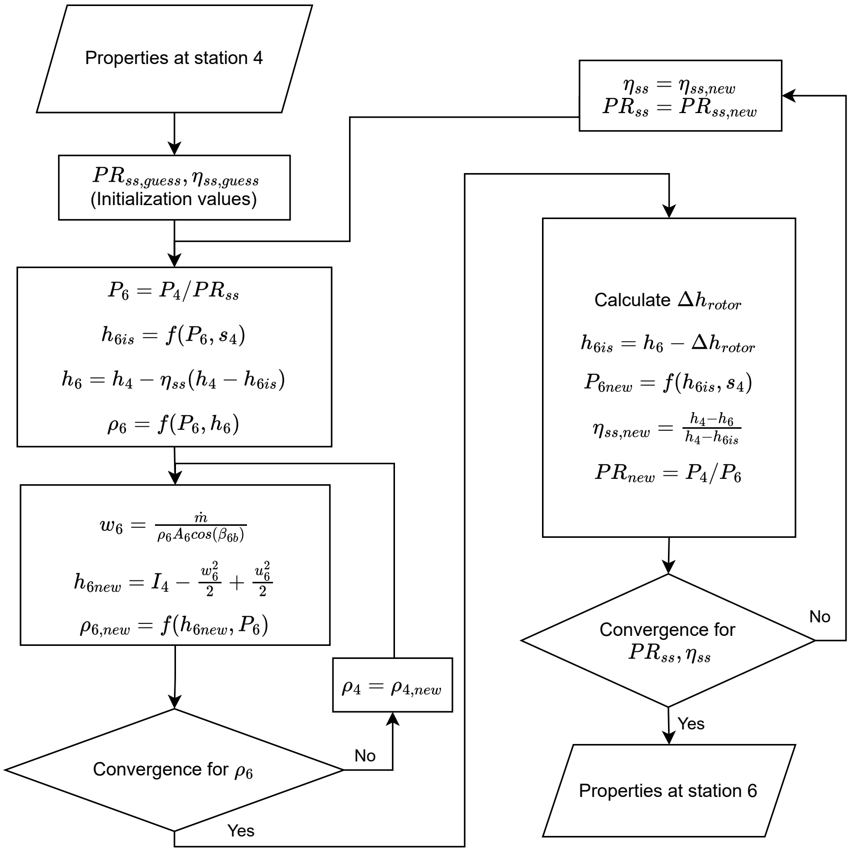
Properties at station 4
$PR_{ss,guess}, \eta_{ss,guess}$
(Initialization values)
$P_6 = P_4/PR_{ss}$
$h_{6is} = f(P_6, s_4)$
$h_6 = h_4 - \eta_{ss}(h_4 - h_{6is})$
$\rho_6 = f(P_6, h_6)$
$w_6 = \frac{\dot{m}}{\rho_6 A_6 cos(\beta_{6b})}$
$h_{6new} = I_4 - \frac{w_6^2}{2} + \frac{u_6^2}{2}$
$\rho_{6,new} = f(h_{6new}, P_6)$
$\rho_4 = \rho_{4,new}$
Convergence for ρ_6
No
Yes
$\eta_{ss} = \eta_{ss,new}$
$PR_{ss} = PR_{ss,new}$
Calculate Δh_{rotor}
$h_{6is} = h_6 - \Delta h_{rotor}$
$P_{6new} = f(h_{6is}, s_4)$
$\eta_{ss,new} = \frac{h_4 - h_6}{h_4 - h_{6is}}$
$PR_{new} = P_4/P_6$
Convergence for PR_{ss}, η_{ss}
No
Yes
Properties at station 6

Figure 5.11: Evaluation of properties at rotor exit.

following observations are made:

- Examining the loss breakdown figures 5.12c and 5.12d, it becomes apparent that the incidence loss significantly influences the shape of the loss total curve.
- Across all mass flowrate cases, the rotor passage loss appears to contribute to a substantial share of the total losses. Moreover, this loss increases exponentially near the onset of choking conditions. Due to the significant variations in the loss evaluation in this region, the meanline model fails to converge during its iteration procedures. From figure 5.12a, it can be seen that the model was able to perform close to the choking conditions but not after. **Hence, this is a limitation of the model developed in this work**.
- From the figures 5.12a and 5.12b, there seems to be a good agreement in the trend of the pressure ratio and efficiency with deviations taking place at low-pressure ratios. A possible reason for this deviation could be that the loss models were developed based on the data of low-pressure ratio turbines, as noted by Meroni [31]. Meroni later showed in his work that by tuning the loss models based on performance data from high-pressure turbines, a more suitable fit could be obtained.
- Near the onset of choking conditions at high flow rates, the assumption of the zero deviation angle becomes less accurate. This could be a possible reason for the model's deviation of the models in these conditions.

Overall, the model is able to reasonably predict both the trends and values from the validation case. Hence, the loss models and the performance modelling approach presented are deemed suitable and can be applied as routines in the design mode of the turbine.

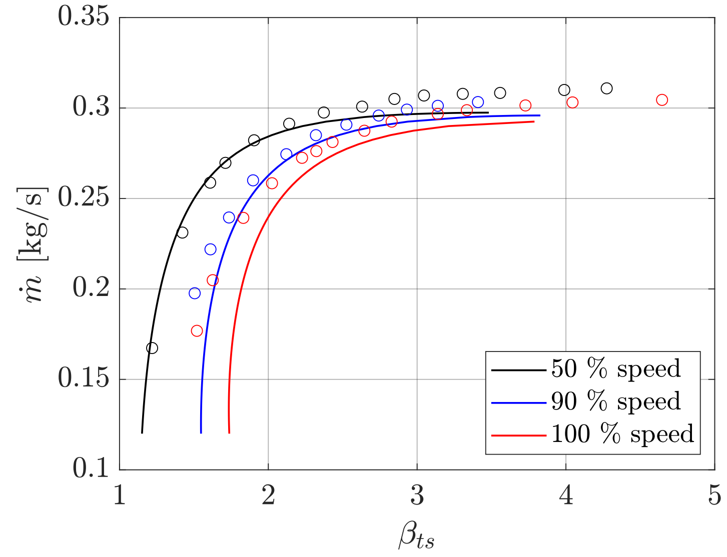

(a) Mass flowrate vs total to static pressure ratio. The experimental data is represented by circles, while the compressor model prediction is shown as a line.

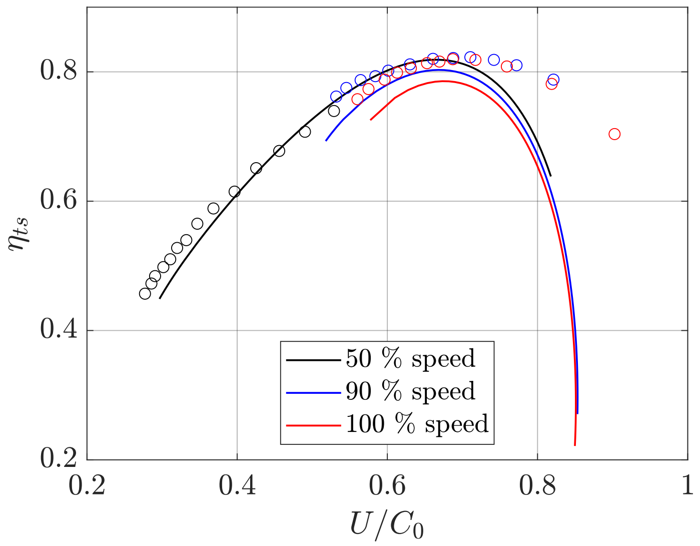

(b) Total-to-static efficiency vs U/C_O. The experimental data is represented by circles, while the compressor model prediction is shown as a line.

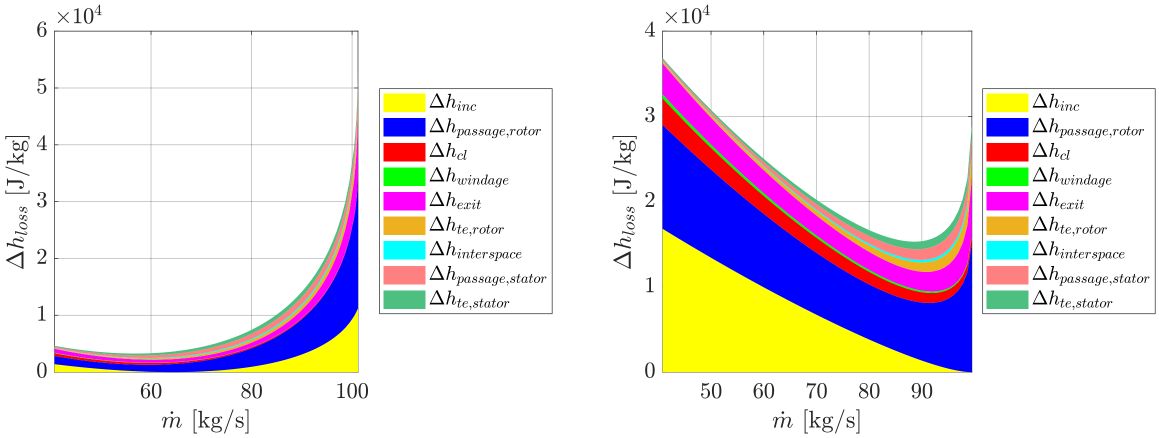

(c) Loss distribution for 50% speed case.

(d) Loss distribution for 100% speed case.

Figure 5.12: Comparison of meanline model vs experimental data of the McLallin turbine. In the graphs, the design speed is 33262 rpm.

5.8. Turbine meanline design model

The design methodology presented in this section is based on the works of Gambini and Vellini [23], Moustapha [78], and Meroni [31], and is carried out as shown in figure 5.13.

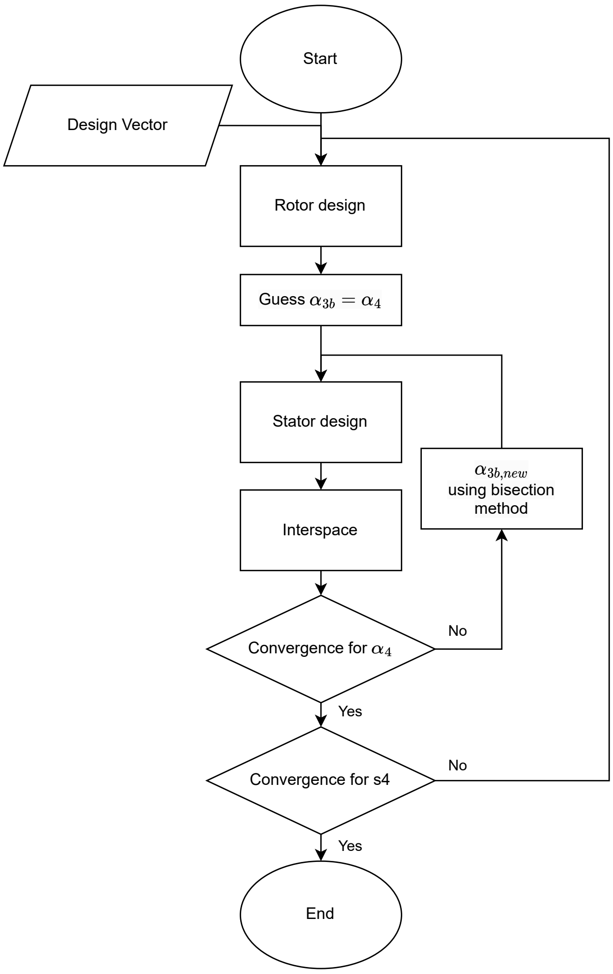
Start
Design Vector
Rotor design
Guess $\alpha_{3b} = \alpha_4$
Stator design
$\alpha_{3b,new}$ using bisection method
Interspace
Convergence for α_4
No
Yes
Convergence for s4
No
Yes
End

Figure 5.13: Flowchart for turbine design.

To conduct turbine design, the following inputs are used:

$$\textbf{Design Vector} = \left[\dot{m}, P_{01}, T_{01}, P_6, N, \psi, \phi, \xi, \frac{r_{6h}}{r_{6t}}\right]. \tag{5.27}$$

Furthermore, the recommended range for these design variables is outlined in table 5.1.

Table 5.1: Recommended range for input parameters for the radial inflow turbine [23, 78].

Parameter	Symbol	Unit	Range
Work coefficient	ψ	-	0.8-1.0
Flow coefficient	ϕ	-	0.2-0.3
Meridional velocity ratio	ξ	-	1
Rotor hub to tip ratio	$\frac{r_{6h}}{r_{6t}}$	-	<0.4

5.8.1. Rotor design

The design of the turbine begins with the rotor and follows the procedure as shown in figure 5.14. A starting assumption is made of the conditions of the stator exit using a guess of the entropy s_4. Using a suitable set of design variables, the inlet velocity triangle can be constructed. The outlet velocity triangle is constructed using ξ and the hub-to-tip ratio.

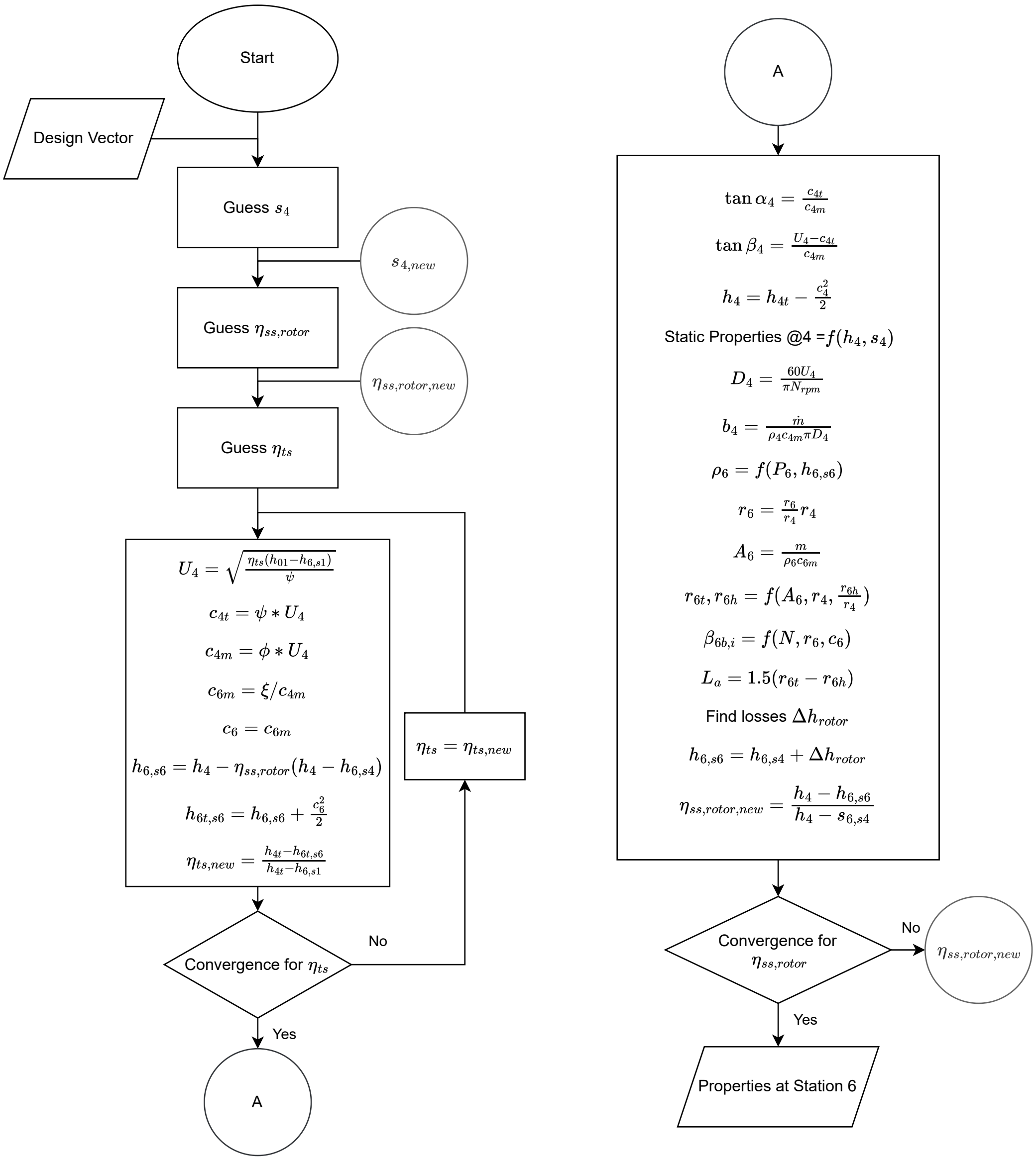
Start
Design Vector
Guess s_4
$s_{4,new}$
Guess $\eta_{ss,rotor}$
$\eta_{ss,rotor,new}$
Guess η_{ts}
$U_4 = \sqrt{\frac{\eta_{ts}(h_{01}-h_{6,s1})}{\psi}}$
$c_{4t} = \psi * U_4$
$c_{4m} = \phi * U_4$
$c_{6m} = \xi / c_{4m}$
$c_6 = c_{6m}$
$h_{6,s6} = h_4 - \eta_{ss,rotor}(h_4 - h_{6,s4})$
$h_{6t,s6} = h_{6,s6} + \frac{c_6^2}{2}$
$\eta_{ts,new} = \frac{h_{4t}-h_{6t,s6}}{h_{4t}-h_{6,s1}}$
$\eta_{ts} = \eta_{ts,new}$
Convergence for η_{ts}
No
Yes
A
A
$\tan\alpha_4 = \frac{c_{4t}}{c_{4m}}$
$\tan\beta_4 = \frac{U_4 - c_{4t}}{c_{4m}}$
$h_4 = h_{4t} - \frac{c_4^2}{2}$
Static Properties @4 = $f(h_4, s_4)$
$D_4 = \frac{60U_4}{\pi N_{rpm}}$
$b_4 = \frac{\dot{m}}{\rho_4 c_{4m} \pi D_4}$
$\rho_6 = f(P_6, h_{6,s6})$
$r_6 = \frac{r_6}{r_4} r_4$
$A_6 = \frac{m}{\rho_6 c_{6m}}$
$r_{6t}, r_{6h} = f(A_6, r_4, \frac{r_{6h}}{r_4})$
$\beta_{6b,i} = f(N, r_6, c_6)$
$L_a = 1.5(r_{6t} - r_{6h})$
Find losses Δh_{rotor}
$h_{6,s6} = h_{6,s4} + \Delta h_{rotor}$
$\eta_{ss,rotor,new} = \frac{h_4 - h_{6,s6}}{h_4 - s_{6,s4}}$
Convergence for $\eta_{ss,rotor}$
No
$\eta_{ss,rotor,new}$
Yes
Properties at Station 6

Figure 5.14: Flowchart for turbine rotor design.

Similar to the compressor case, the remaining geometric values, are determined using the following empirical relations as given in the textbook of Gambini and Vellini [23].

- The number of blades is given as:

$$N_{b,rotor} = \text{int}\left(\frac{\pi(100 - \alpha_4)\tan\alpha_4}{30}\right) \tag{5.28}$$

- The rotor axial length is calculated as

$$L_a = 1.5b_6. \tag{5.29}$$

- The blade thickness is given by
$$t_b = 0.01 D_4, \tag{5.30}$$
- Rotor clearances are approximated as
$$\epsilon_{b,t} = 0.05 b_4 \tag{5.31}$$

Once the rotor geometry is defined, the losses are evaluated, and the efficiency updates are made until convergence is reached. The analysis then proceeds to the stator section.

5.8.2. Stator design

As the rotor inlet velocity triangle is defined, the stator must be designed such that this triangle can arrive at the stator exit as shown in figure 5.15.

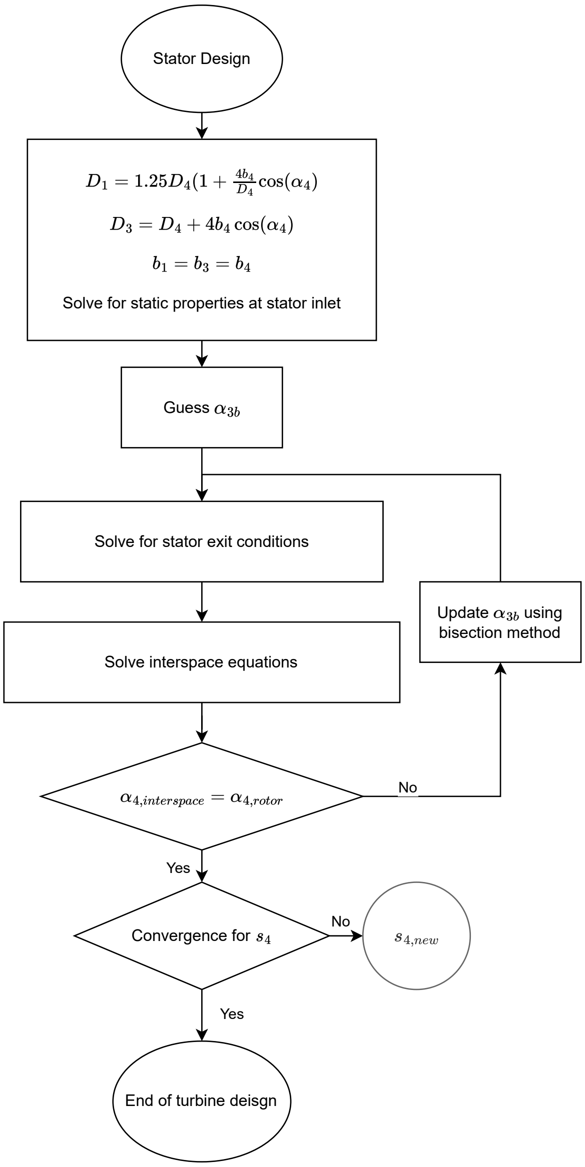
Stator Design
$D_1 = 1.25D_4(1 + \frac{4b_4}{D_4}\cos(\alpha_4)$
$D_3 = D_4 + 4b_4\cos(\alpha_4)$
$b_1 = b_3 = b_4$
Solve for static properties at stator inlet
Guess α_{3b}
Solve for stator exit conditions
Update α_{3b} using bisection method
Solve interspace equations
$\alpha_{4,interspace} = \alpha_{4,rotor}$
No
Yes
Convergence for s_4
No
$s_{4,new}$
Yes
End of turbine deisgn

Figure 5.15: Flowchart for turbine stator design.

The dimensions of the stator are calculated using the following equations as compiled by Gambini and Vellini [23]

- Nozzle inlet diameter:

$$D_1 = 1.25D_4\left(1 + 4\frac{b_4}{D_4}\cos\alpha_4\right). \tag{5.32}$$

- Nozzle exit diameter:

$$D_3 = D_1 + 4b_4\cos\alpha_4. \tag{5.33}$$

- Number of stator blades:

$$N_{b,stator} = \text{int}\left(\frac{2.5\pi D_3\cos(\alpha_3/2)}{D_1 - D_3}\right) \tag{5.34}$$

Additionally, it is assumed that the width of the turbine is the same as the rotor inlet for simplicity.

$$b_1 = b_3 = b_4. \tag{5.35}$$

The remaining variable is the stator blade angle α_{3b}. In general cases, the blade angle is assumed to be the same as the rotor inlet velocity triangle [23]; hence, this can be used as a guess value for the solution. The stator exit angle is found using a bisection method by checking for a range of α_{3b} values. The static density was matched for the convergence criteria, as it was most sensitive to the different values of α_{3b}. On the convergence of α_{3b}, the entropy of the stator exit is used to update rotor inlet conditions till convergence.

6

Design case for 100kW PTES system

6.1. PTES system design

To develop a PTES system with a power output of 100 kW, the methodology outlined by Radi [2] is used. Table 6.1 illustrates the input and output parameters of the model. These input values were taken from the work by Gautam [10]. The working fluid employed in this system is R1233zd(E), while sunflower oil was chosen as the sensible storage medium, again as done by Gautam [10]. To size the system, the compressor power was adjusted accordingly to attain a turbine power output of 100 kW.

Table 6.1: PTES model inputs and results using R1233zd(E) as a working fluid.

Model Inputs				Model Outputs			
Waste heat temperature	T_{source}	80	°C	Compressor flowrate	$\dot{m}_{compressor}$	3.70	kg/s
Ambient temperature	$T_{ambient}$	15	°C	Compressor pressure ratio	$\beta_{compressor}$	8.75	-
Storage temperature	$T_{storage}$	190	°C	Compressor inlet pressure	$P_{in,compressor}$	5.52	bar
Pinch across heat exchanger	ΔT_{pinch}	2	°C	Compressor inlet temperature	$T_{in,compressor}$	78.00	°C
Heat pump superheat	$\Delta T_{HP,superheat}$	5	°C	Turbine flowrate	$\dot{m}_{turbine}$	1.83	kg/s
Heat engine superheat	$\Delta T_{HE,superheat}$	15	°C	Turbine pressure ratio	$\beta_{turbine}$	20.32	-
Heat engine subcool	$\Delta T_{subcool}$	5	°C	Turbine inlet pressure	$P_{in,turbine}$	23.66	bar
Compressor efficiency	$\eta_{compressor}$	80	%	Turbine inlet temperature	$T_{in,turbine}$	156.74	°C
Turbine efficiency	$\eta_{turbine}$	88	%	Turbine output power	$W_{turbine}$	100.03	kW
Pump efficiency	η_{pump}	80	%	Pump input power	$W_{turbine}$	4.04	kW
Charging duration	t_{ch}	8	hours	Heat pump COP	COP	4.76	-
Discharging duration	t_{disch}	12	hours	Heat engine efficiency	η_{HE}	18.35	%
Compressor input power	$W_{compressor}$	164.70	kW	Round trip efficiency	η_{RTE}	87.43	%

The resulting temperature-entropy and temperature-energy plots from the PTES model are shown in figure 6.1.

6.2. Turbomachinery for 100 kW case

From the PTES analysis, the requirements for the turbomachinery in the 100 kW system are presented in table 6.1. To select the number of stages, Gambini and Vellini [23] suggested an approach based on the optimal specific speed ranges as illustrated in figures 6.2a and 6.2b.

In both instances, using an axial-type configuration is not advisable. Achieving the desired pressure ratios with this configuration would require multiple stages and lie outside the optimal specific speed range. Additionally, based on rough sizing estimates, the blade's resulting blade height in all the stages is below 3 cm which can lead to high clearance losses.

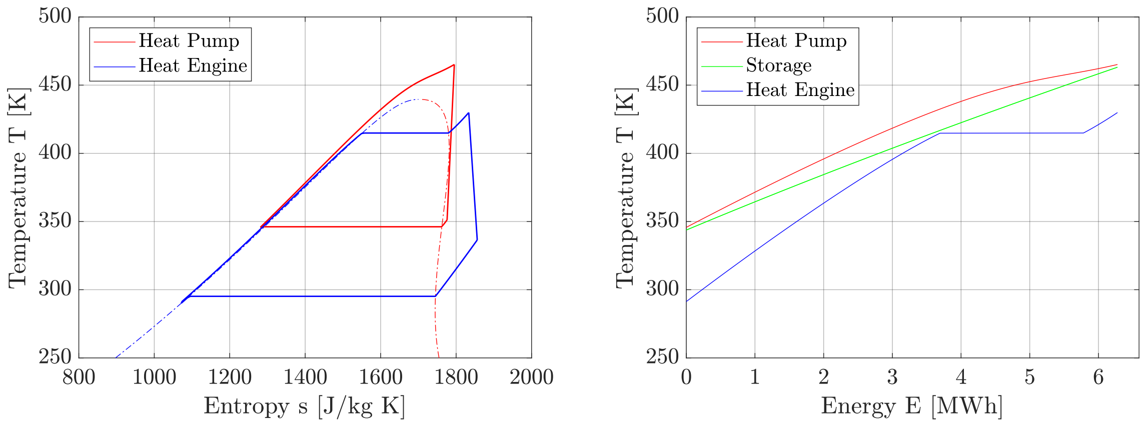

(a) T-s diagram.

(b) T-E diagram.

Figure 6.1: PTES cycle based on inputs from table 6.1 with R1233zd(E) as the working fluid.

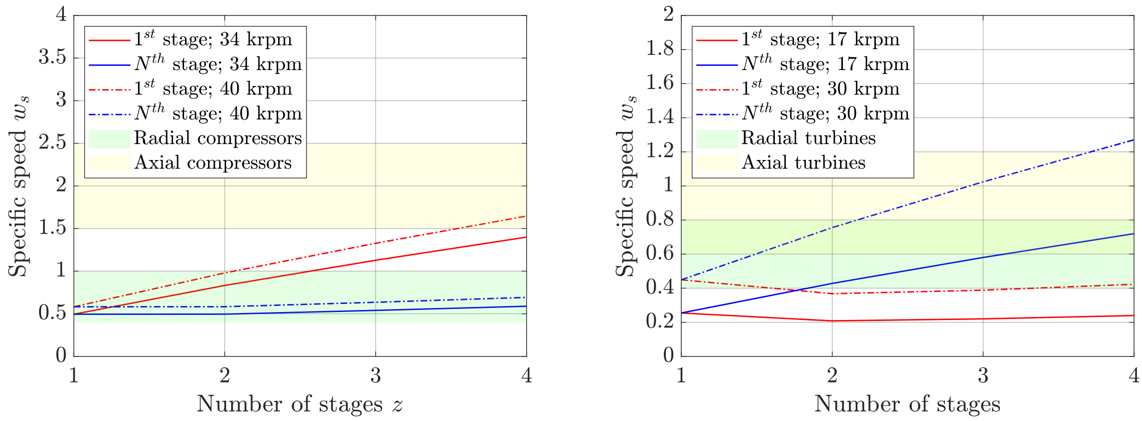

(a) Selection study for compressor.

(b) Selection study for turbine.

Figure 6.2: Specific speed versus the number of stages for the turbine based on inputs from table 6.1. The shaded areas represent the optimal range of specific speeds.

From figure 6.2, a 2-stage configuration appears to be a suitable choice for the compressor based on the specific speed. Radial turbines can operate for expansion ratios up to 6, even up to 100 [31]. Therefore, selecting a single-stage turbine is acceptable, but this leads to supersonic conditions at the design point for the optimal range for flow and work coefficients. As a result, a two-stage radial turbine is selected. Regarding the operating speed, although 30 krpm is within the optimal range for both turbine stages, operating at such speeds results in a design with rotor tip ratios greater than one, rendering it unfeasible. A reduced speed of 17 krpm is chosen for the design case instead. Using work coefficient relations given by Gambini and Vellini [23], an initial sizing of the compressor and turbine rotors showed that the peripheral speeds stay below 300 m/s [29]. Table 6.2 summarises the final turbomachinery selection details.

6.3. Compressor section

6.3.1. Compressor design

Based on the inputs from tables 6.1 and 6.2, the compressor design is carried out according to the methodology in section 4.7. For the compressor design, the following design decisions

Table 6.2: Preliminary turbomachinery selection results based on specific speed.

Turbomachine	Centrifugal compressor		Radial inflow turbine	
Number of stages	2		2	
Rotational speed [rpm]	34000		17000	
Stage	First stage	Last stage	First stage	Last stage
Specific speed [-]	0.83	0.50	0.21	0.43
Rotor diameter [mm]	111	105	150.9	174.3
Peripheral speed [m/s]	197.7	186.9	134.3	155.1

and assumptions were made.

- The design variables were chosen based on the prescribed ranges given in table 6.3 through trial and error. There are seven decision variables for the two-stage compressor with the same rotational speed, and an optimisation would need to be carried out to obtain a better outcome of the results. However, this activity is not in the scope of this work.

Table 6.3: Design variables for the compressor design

	ϕ_{is}	α_2 [deg]	$\frac{r_{1h}}{r_{1t}}$	N [rpm]
Stage 1	0.6	75	0.6	34000
Stage 2	0.6	71	0.6	34000

- The pressure ratio was equally divided across the stages for simplicity. However, this may not be the optimal choice. In a later work, Guiffre [84] carried out a study for a two-stage compressor setup where the pressure ratio split was also considered an optimisation variable. This was considered as the second stage handles a significantly smaller volumetric flow rate. Consequently, the relative clearances, roughness, and blockage become significant, adversely affecting the compressor's performance.
- The blade thickness and clearances are taken as fixed values
- A constant width of the vaneless section is used for the case of simplicity.
- At design condition, the wake fraction ε_{wake} is assumed as a constant 0.5, similar to the Schiffmann impeller. Hence, during the off-design procedure, a constant value of ε_{wake} was also taken for consistency with the design point performance. This approach differs from what was employed in the validation scenarios. This is because the proximity to the choke point during the design procedure is uncertain. To address this assumption, insights from higher fidelity models, like CFD, might be necessary.
- The value of k_{vl} for the vaneless friction factor coefficient is assumed to be 0.011, the same as the value used for modelling the Schiffmann impeller. Again, this assumption would need initial tuning from a higher fidelity model.

Based on these inputs, the outcomes of the compressor design are presented in table 6.4. The results show that the blade heights at the second stage rotor exit are small, of the order of a millimetre. This can be attributed to the relatively low volume flow rates at the exit.

6.3.2. Compressor performance

From the performance charts in figure 6.3, the following can be inferred:

Table 6.4: Results for compressor design.

Parameter	Stage 1	Stage 2
$D_{1,tip}$ [mm]	64.5	41.3
$D_{1,hub}$ [mm]	38.7	24.8
$\beta_{1b,hub}$ [deg]	44.2	40.9
$\beta_{1b,hub}$ [deg]	58.4	55.3
D_2 [mm]	110.3	104.6
b_2 [mm]	5.7	1.30
β_{2b} [deg]	64.1	57.4
D_3 [mm]	122.1	119.5
b_3 [mm]	5.7	1.3
L_a [mm]	33.1	31.4
ϵ_b [mm]	0.1	0.1
ϵ_a [mm]	0.1	0.1
ϵ_r [mm]	0.1	0.1
t_1 [mm]	0.5	0.5
t_2 [mm]	0.5	0.5
N_b	25	25
η_{tt} [%]	83%	74%
$Ma_{w_1,hub}$	0.71	0.55
Ma_{w_2}	0.65	0.84

- The design point of the second stage is very close to choking and leaves little room to increase the flow rates at off-design conditions. Moreover, the overall efficiency at the design point is 77.7%, which is less than the assumption of 80% used in the PTES model. A better choice of design inputs through an optimisation study may lead to a more suitable design point performance.
- Due to the ratio of b_2/r_2 of the first stage, the stall limits the operating range of the compressor. A suitable pinch could be applied to delay stall inception [47]. Alternatively, the value of α_2 in the design vector can be reduced.
- From figure 6.3e, it can be seen the minimum operating mass flow rate for stable compressor performance is determined by the first stage stall at lower speeds and second stage surge at higher speeds.
- Regarding the efficiencies plots, the tuning parameters assumed would significantly affect the efficiency prediction and can lead to better or worse conditions. Hence, they would need tuning from higher fidelity models or experimental cases dealing with similar operating conditions. Additionally, the clearances chosen affect the leakage and recirculation losses. As this is fixed on the lower end, more relaxed clearances for other practical considerations, say machining limitations, may lead to worse efficiencies.

6.4. Turbine section

6.4.1. Turbine design

Based on the inputs from tables 6.1 and 6.2, the turbine design is carried out according to the methodology in section 5.8. For the turbine design, the following design decisions and assumptions were made:

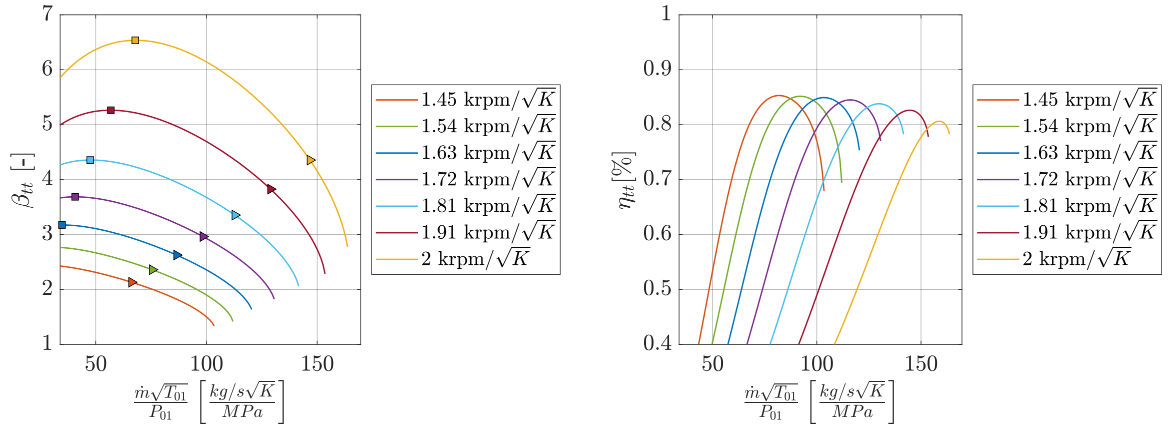

(a) Stage 1: β_{tt} vs $\frac{\dot{m}\sqrt{T_{01}}}{P_{01}}$.

(b) Stage 1: η_{tt} vs $\frac{\dot{m}\sqrt{T_{01}}}{P_{01}}$.

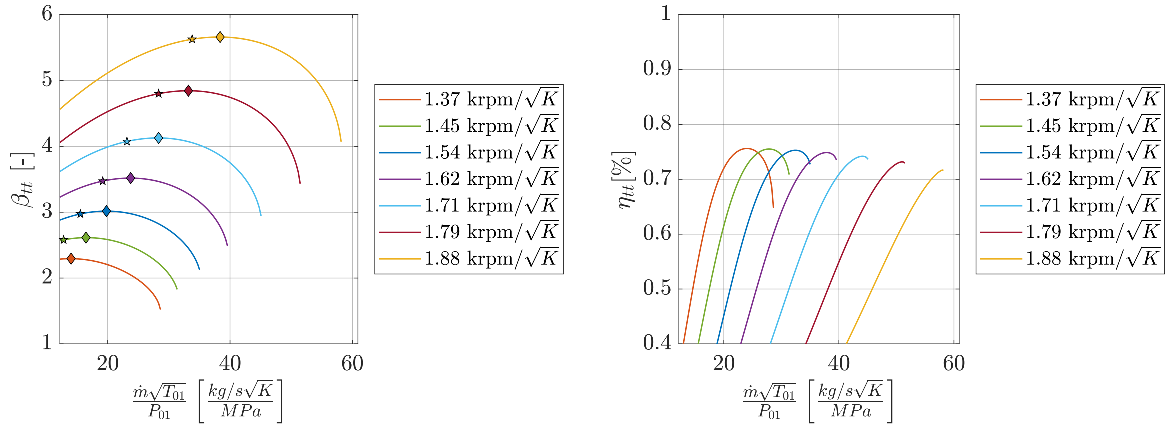

(c) Stage 2: β_{tt} vs $\frac{\dot{m}\sqrt{T_{01}}}{P_{01}}$.

(d) Stage 2: η_{tt} vs $\frac{\dot{m}\sqrt{T_{01}}}{P_{01}}$.

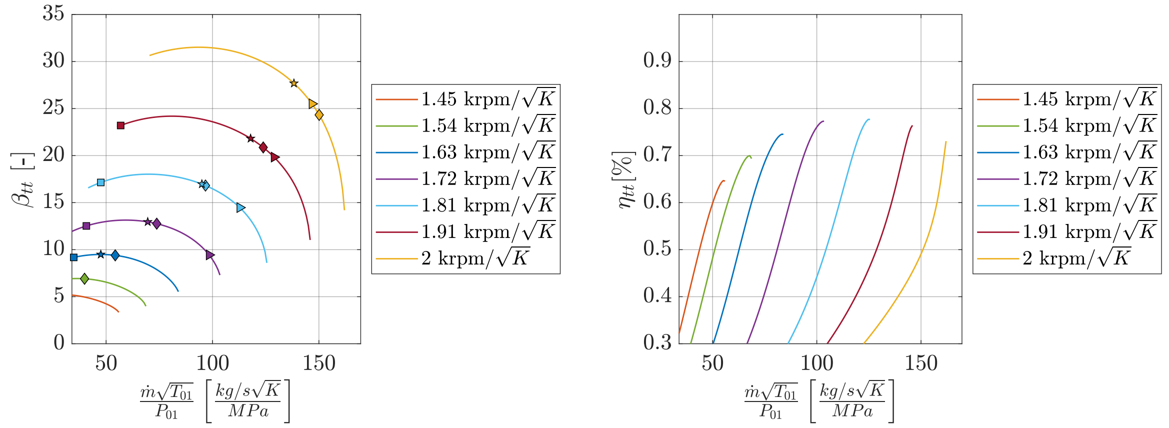

(e) Overall: β_{tt} vs $\frac{\dot{m}\sqrt{T_{01}}}{P_{01}}$.

(f) Overall: η_{tt} vs $\frac{\dot{m}\sqrt{T_{01}}}{P_{01}}$.

Figure 6.3: Performance charts for a two-stage compressor configuration. The surge points for the first and second stages are marked by squares and diamonds. The rotating stall points are shown as triangles and stars for the first and second stages, respectively

- Similar to the compressor case, the input parameters for the turbine are chosen based on trial and error as shown in table 6.5. The work coefficient was chosen below the optimal range, as the design code was unable to converge on a solution for higher values. There are nine decision variables for the two-stage turbine, and an optimisation study would need to be carried out to obtain a better design outcome, which is not in the scope of this work.

Table 6.5: Design variables for the turbine design

	ψ	ϕ	$\frac{r_{6h}}{r_{6t}}$	ξ	N [rpm]
Stage 1	0.7	0.2	0.4	1	17000
Stage 2	0.6	0.2	0.4	1	17000

- At the exit of the turbine, the fluid velocity is assumed to be 10 m/s to determine the static pressure. Additionally, as the turbine deals with total to static pressure ratios, the split was made such that the first stage was designed to square root the required pressure ratio. The total pressure from the first stage and the final static pressure at the evaporator exit were then used as the design case for the second stage.
- The blade thickness, clearances, and roughness values were taken as fixed values.
- The height of the stator vanes is taken as the rotor inlet height for simplicity.
- Regarding the loss modelling, the value of k_{vl} is taken as 0.005, like in the case of the McLallin turbine.
- The flow is assumed to follow the blade angle at the stator and rotor exits, with no flow deviation. Consequently, the performance prediction at a high Mach number may differ from those achieved using higher fidelity models.
- The rotor inlet blade angle is chosen to be radial, as the blade angle does not affect the incidence loss relation used. Radial blades are often used in cases where high temperatures are involved and to reduce the stress on the blades. However, a non-radial blade may lead to better efficiency [78], but this would require an alternate modelling approach.

Based on these inputs, the outcomes of the turbine design are presented in table 6.6. The results show that small blade heights are obtained as part of the design process as the density at the turbine inlet is relatively high.

6.4.2. Turbine performance

From the performance graphs, the following can be observed.

- From figures 6.4a and 6.4c, the mass flow rate of the turbines converges near the onset of choking conditions. In the first stage, all the speed lines converge to the same mass flow case, indicating that the stator is choked first. In the second stage, there is a variation of the choking flow rate with speed, indicating that the rotor is choked first for the given inlet conditions.
- The pressure ratio curves in figure 6.4a show an increase at low mass flowrates. The reason for this behaviour is due to the incidence loss at these operating points.
- The overall total-to-static efficiency at the design point is 70%, which is much less than the 88 % assumed in the case of the PTES model.

Table 6.6: Results for turbine design.

Parameter	Stage 1	Stage 2
D_1 [mm]	248.1	275.7
b_1 [mm]	1.1	4.1
α_{1b} [mm]	0	0
D_3 [mm]	198.4	220.5
b_3 [mm]	1.1	4.1
α_{3b} [mm]	74.2	71.9
D_4 [mm]	197.2	215.4
b_4 [mm]	1.1	4.1
β_{4b} [deg]	0	0
$D_{6,tip}$ [mm]	64.1	113.5
$D_{6,hub}$ [mm]	36.5	39.8
b_6 [mm]	13.8	36.8
$\beta_{6b,hub}$ [deg]	42.8	42.8
$\beta_{6b,hub}$ [deg]	58.4	69.2
L_a [mm]	20.7	55.2
$\epsilon_a, \epsilon_b, \epsilon_r$ [mm]	0.1	0.1
t_1, t_3, t_4, t_6 [mm]	1	1
$N_{b,stator}$	25	25
$N_{b,rotor}$	10	9
η_{ts} [%]	70%	67%
Ma_{w4}	0.47	0.57
Ma_{c4}	0.96	0.81
Ma_{w6}	0.38	0.52

- Similar to the compressor case, The values of the roughness, clearances, blade thickness and the value of k_{vl} can influence the turbine's efficiency.

6.5. Off design characteristics of the PTES system

In the PTES model, the storage temperature at the inlet and exit are fixed, and hence, the charging and discharging cycles can be decoupled and investigated separately. Under different mass flow cases, the compressor and turbine performance vary leading to the off-design characteristic of the PTES system. The following sections discuss to analyse the PTES system charging and discharging cycles coupled with the turbomachinery meanline models.

6.5.1. PTES charging

To study the off-design charging performance, it is important to ensure that the condenser for the heat pump cycle is suitably sized, such that the pitch point for the charging cycle is reached at the condenser exit. Given the same waste heat temperature is the same, the inlet conditions of the compressor will remain unchanged. Operating the compressor under different mass flowrates and speeds results in altered outlet conditions, as per the overall performance curves. Conducting a sensitivity analysis of the compressor performance, the heat pump cycle will change as follows:

- For a pressure ratio higher than the design point, the temperature at the compressor outlet would increase as shown in figure 6.5, and the pinch point is hence no longer reached at the condenser inlet.

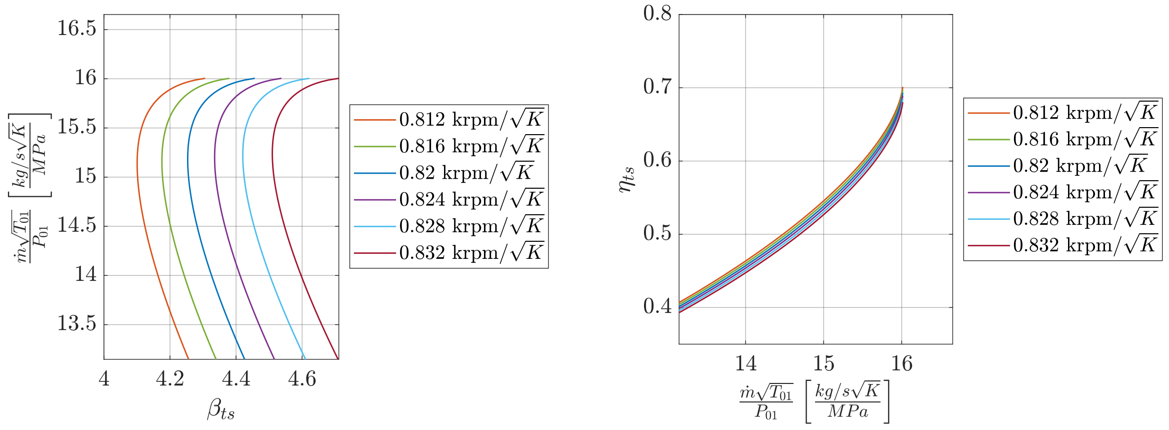

(a) Stage 1: $\frac{\dot{m}\sqrt{T_{01}}}{P_{01}}$ vs β_{ts}.

(b) Stage 1: η_{tt} vs $\frac{\dot{m}\sqrt{T_{01}}}{P_{01}}$.

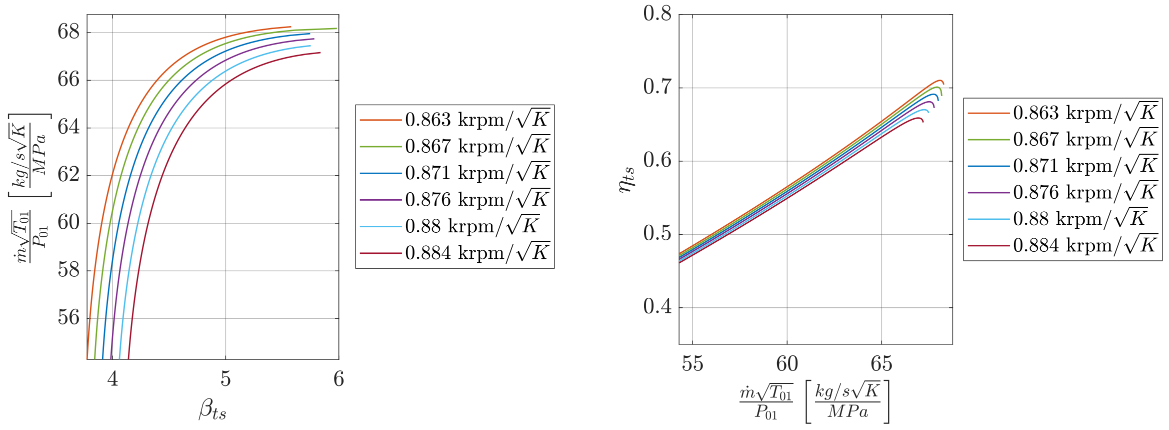

(c) Stage 2: $\frac{\dot{m}\sqrt{T_{01}}}{P_{01}}$ vs β_{ts}.

(d) Stage 2: η_{tt} vs $\frac{\dot{m}\sqrt{T_{01}}}{P_{01}}$.

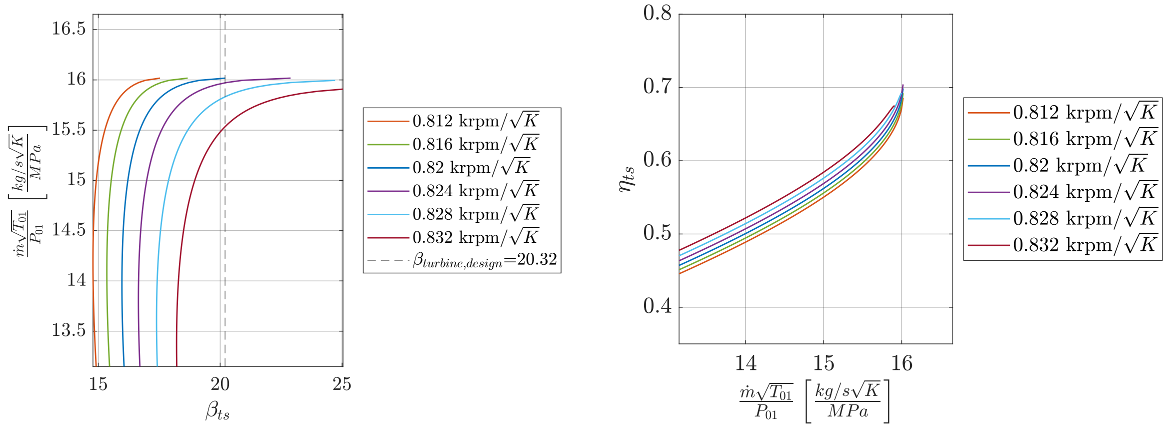

(e) Overall: $\frac{\dot{m}\sqrt{T_{01}}}{P_{01}}$ vs β_{ts}.

(f) Overall: η_{tt} vs $\frac{\dot{m}\sqrt{T_{01}}}{P_{01}}$.

Figure 6.4: Performance charts for a two-stage turbine configuration.

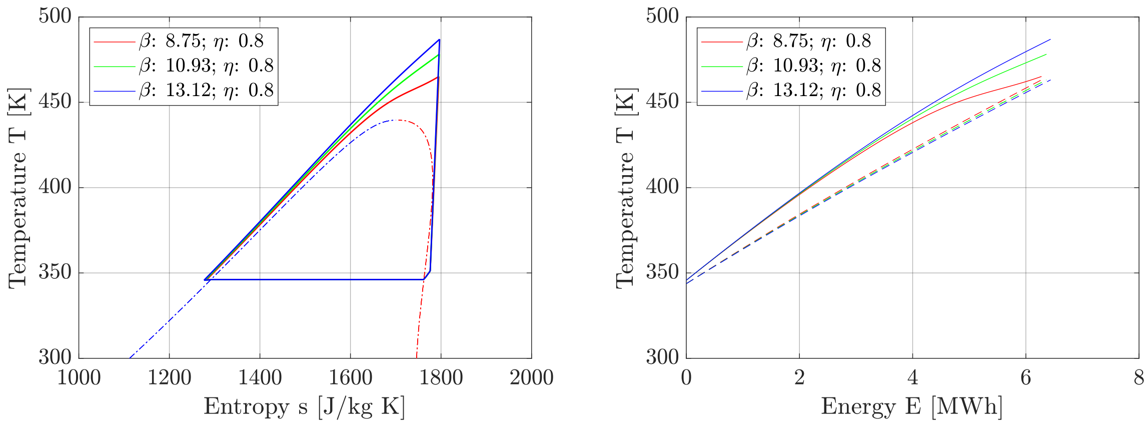

(a) T-s diagram for varied β. **(b)** T-E diagram for varied β.

Figure 6.5: Charging cycle behaviour for varied compressor pressure ratios.

- Similarly, for efficiencies lower than the assumed compressor design point efficiency, the outlet temperature also increases slightly as shown in figure 6.6

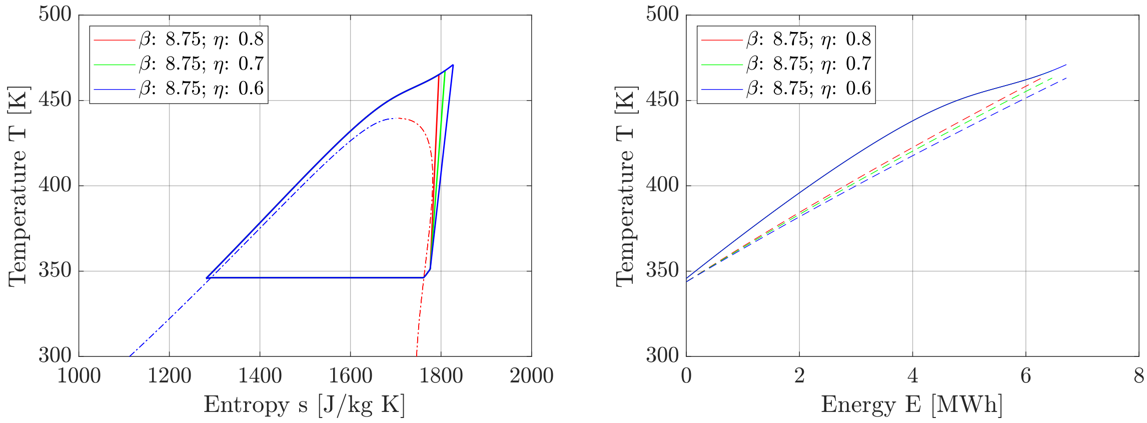

(a) T-s diagram for varied η. **(b)** T-E diagram for varied η.

Figure 6.6: Charging cycle behaviour for varied compressor efficiencies.

- To summarise, figure 6.7 shows a sensitivity study of the compressor parameters on the charging cycle COP.

Based on the results of the compressor design case, the overall pressure ratio and efficiency are now used as model inputs for the off-design PTES model. In order to maintain the same storage temperature, the outlet temperature of the compressor should at least be the same as the design case. Also, in order to satisfy the pinch criteria, the pressure ratio at the outlet must also at least be equal to the overall design pressure ratio. For the compressor inlet conditions from table 6.1 and the compressor's overall performance chart, figure 6.8 can be obtained. From this figure, the following observations can be made,

- With the outlet temperature constraint, operating at lower speeds than the design case means operating closer to the unstable region and also a penalty due to very low compressor efficiencies and COP.
- Operating at a rotational speed higher than the design case penalises the COP due to a higher compressor work.

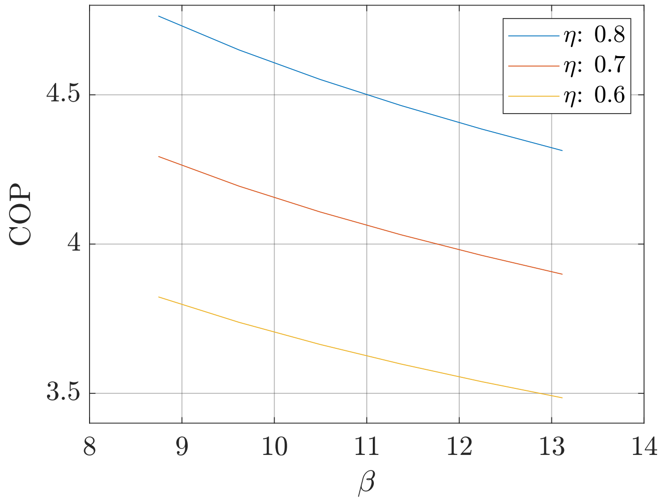

Figure 6.7: Variation of compressor pressure ratio and efficiency on the COP.

- Hence, for each speed case, there is a certain mass flowrate that maximises the COP.

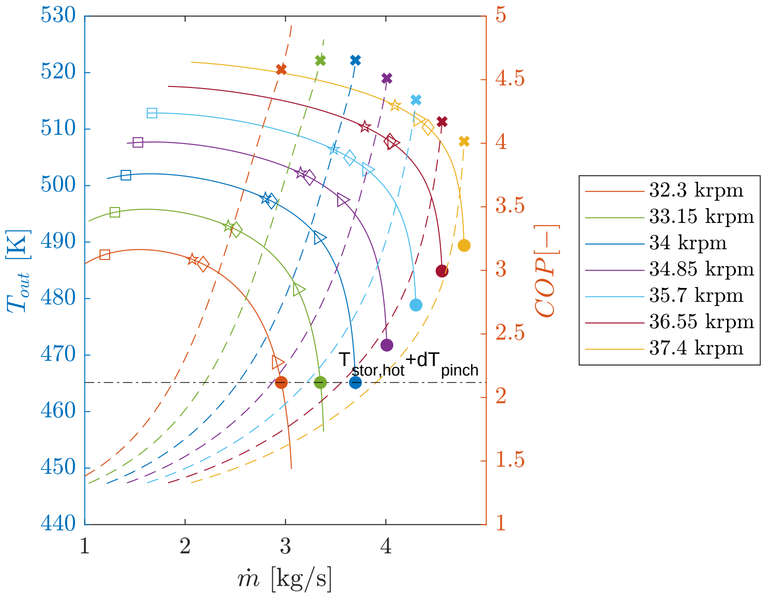

Figure 6.8: Compressor outlet temperature and COP for varying mass flow cases. The solid lines represent the compressor outlet temperature, and the dashed line represents the COP. Also, the squares and diamonds represent the surge points for compressor stages 1 and 2, respectively. The circles represent the optimal operating point for each speed, and the crosses mark the corresponding COP.

In the context of energy storage, different charging powers would mean varying the mass flow rate of the system. Hence plotting the selected operating points from the previous discussion, figure 6.8 can be plotted to understand the charging cycle behaviour. This shows that the best COP is at the design point of the compressor.

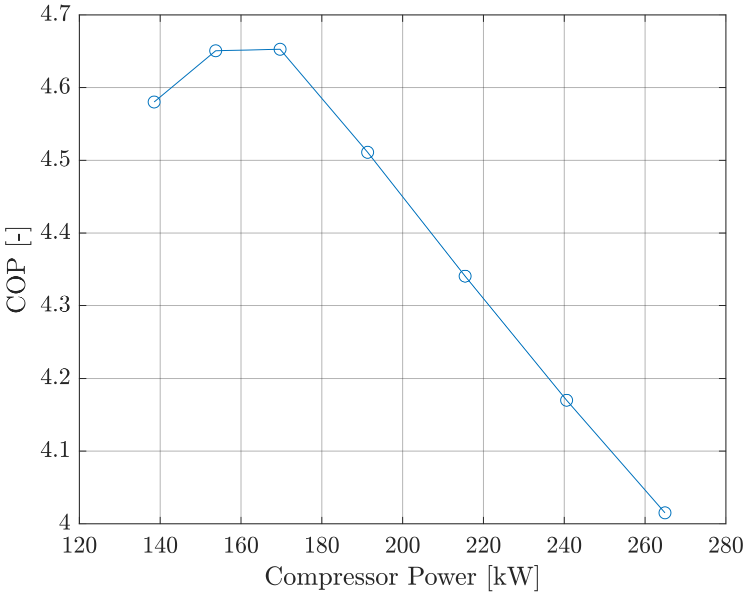

Figure 6.9: Compressor power vs COP

6.5.2. PTES discharging

Operating the compressor under different mass flowrates and speeds results in altered outlet conditions, as per the overall performance curves. Conducting a sensitivity analysis of the compressor performance, the heat pump cycle will change as follows:

In the case of the discharging cycle, the turbine pressure ratio and efficiency can vary depending on the mass flow rate and rotational speed of the operating point, leading to varied exit conditions. The discharging cycle behaviour in the PTES system is, however, less straightforward and is explained by the following sensitivity analysis.

- From figure 6.10a for the case of over-expanding from the design pressure ratio (as shown by the green line), the outlet of the turbine is lower than the saturation pressure of the condenser. This means that the condenser temperature is lower than the ambient, and an additional heat pump would be needed to reject heat to the ambient. In the case of under-expansion (blue line), the exit of the condenser would be at a higher temperature than the design condition. By varying the pump pressure such that the same turbine inlet conditions are met, the pinch condition is now violated. **Hence under off-design conditions, the same turbine pressure ratio must be maintained.**
- In the case of varied turbine efficiency, the heat input to the cycle remains the same, but the turbine power output would vary.

Now, based on the overall turbine performance results, and capping the pressure to the design point, figure 6.12 can be obtained to describe the discharging cycle for off-design conditions. By choosing the same pressure ratio, for an increased speed case, the corresponding mass flow decreases. Correlating these points on the turbine's overall efficiency graphs means that the efficiency decreases for higher-speed cases, explaining the trend shown.

Now, plotting the power corresponding to these selected operating points, figure 6.13 can be plotted, which shows maximum heat engine efficiency is achieved at the turbine's design point.

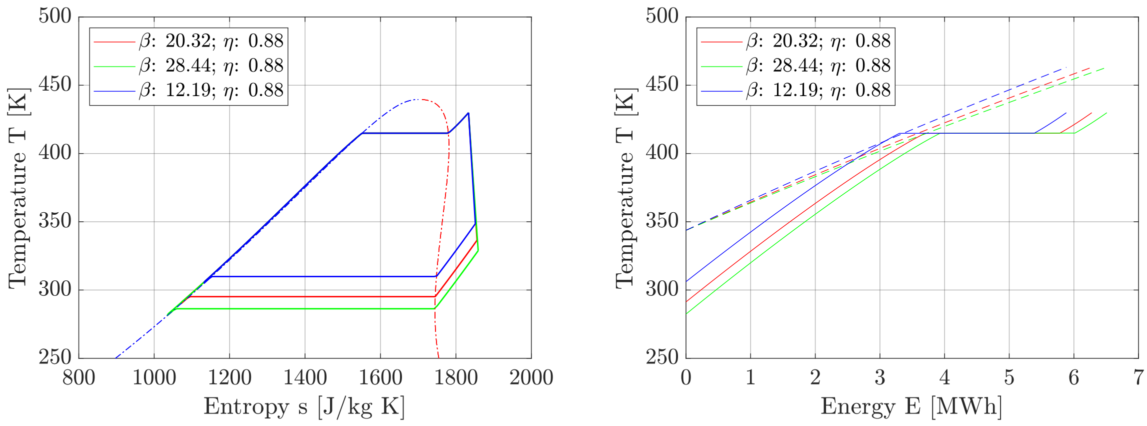

(a) T-s diagram for varied β. **(b)** T-E diagram for varied β.

Figure 6.10: Discharging cycle behaviour for varied turbine pressure ratios

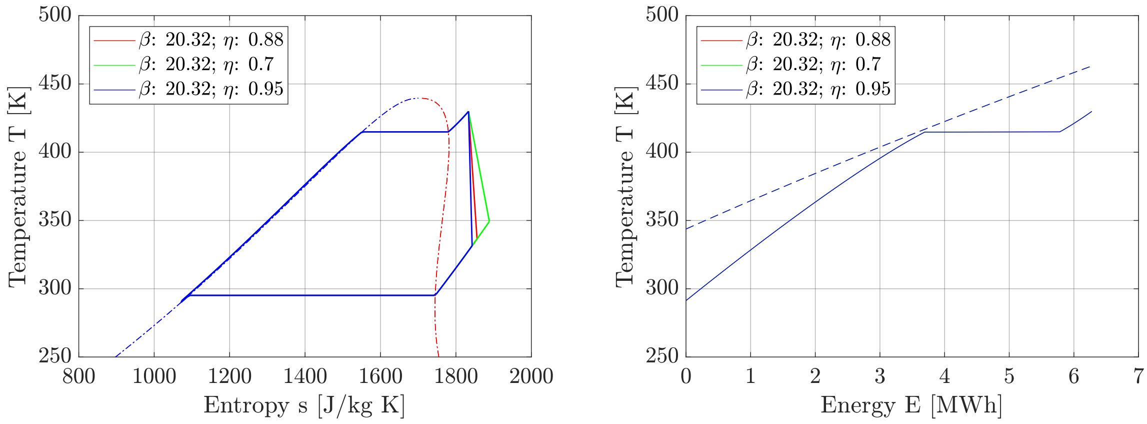

(a) T-s diagram for varied η. **(b)** T-E diagram for varied η.

Figure 6.11: Discharging cycle behaviour for varied turbine pressure ratios.

6.5.3. PTES round trip efficiency

To summarise the PTES system performance under off-design conditions, it is round trip efficiency can be calculated as follows:

$$RTE = \frac{W_{disch}}{W_{ch}} = \frac{P_{disch}t_{disch}}{P_{ch}t_{ch}}, \tag{6.1}$$

where W is work, and P is power.

For the heat pump cycle, the COP can be written as

$$COP = \frac{Q_{storage}}{W_{ch}} = \frac{Q_{storage}}{P_{ch}t_{ch}}, \tag{6.2}$$

which implies

$$P_{ch}t_{ch} = \frac{Q_{storage}}{COP}. \tag{6.3}$$

Similarly, the efficiency of the heat engine during discharging is given as

$$\eta_{HE} = \frac{W_{disch}}{Q_{storage}} = \frac{P_{disch}t_{disch}}{Q_{storage}}, \tag{6.4}$$

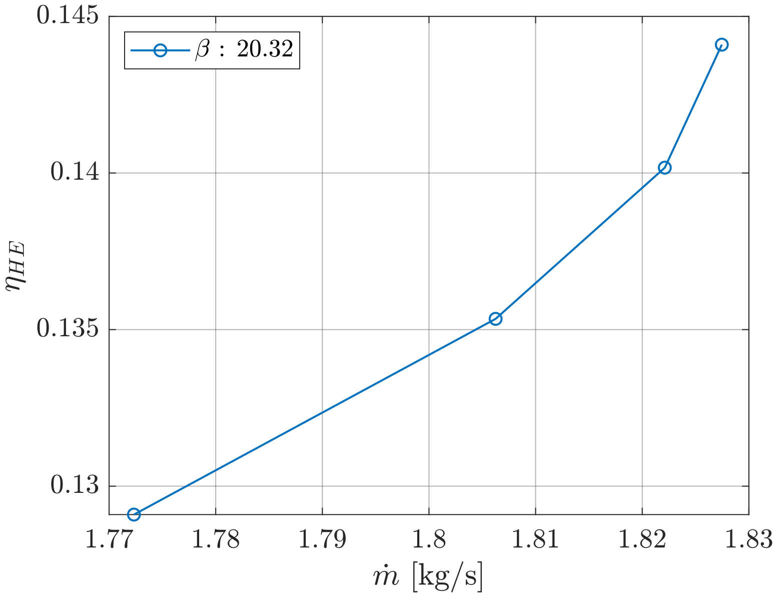

Figure 6.12: Dependence of the heat engine efficiency on the turbine mass flow rate.

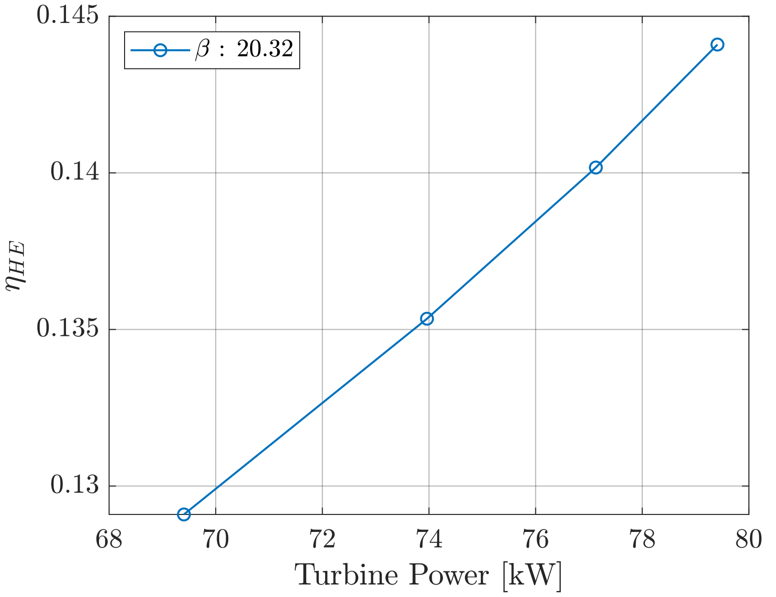

Figure 6.13: Turbine power vs η_{HE}.

and means,

$$P_{disch}t_{disch} = Q_{storage}\eta_{HE}. \tag{6.5}$$

Subsituting equations (6.3) and (6.5) in equation 6.1, the round trip efficiency can be rewritten as:

$$RTE = \frac{Q_{storage}\eta_{HE}COP}{Q_{storage}} = \eta_{HE}COP. \tag{6.6}$$

From figure 6.9, it is evident that different compressor powers correlate with specific values of COP. Similarly, turbine power is associated with heat engine efficiency.

In the storage system, the total energy capacity remains constant, as determined during the PTES design phase. When operating at varying power levels, for instance, in the charging case, the charging time will differ, as all other variables in equation 6.3 are known, and a similar conclusion can be drawn for the discharging cycle. Now, from equation 6.6, it can be seen that the round trip efficiency is solely a function of the COP and η_{HE} since the storage capacity remains constant. Therefore, by utilizing the data from figures 6.9 and 6.13, it is possible to determine the round-trip efficiency shown in figure 6.14. From this graph, the highest efficiency is reached at the design point.

Also, as turbomachinery efficiency assumptions differed from the results of the meanline models, a lower power output is reached at the turbine end. To reach a consistent model, the approach by Radi [2] could be followed, where at the PTES design stage, the meanline model efficiencies are used to update the PTES model iteratively till convergence.

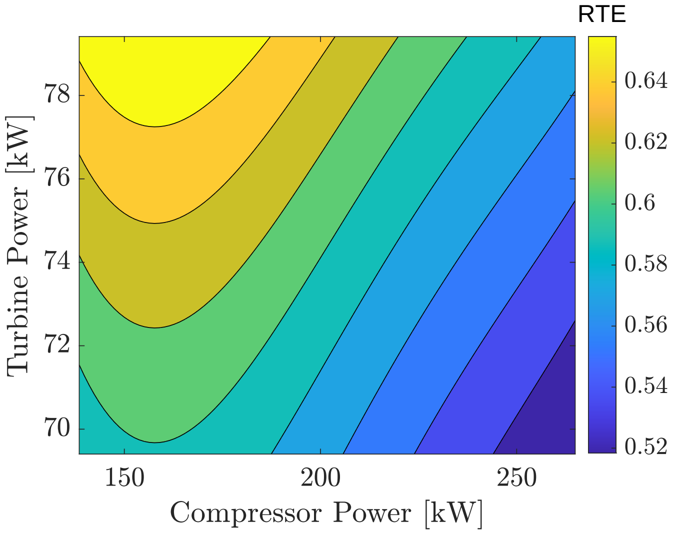

Figure 6.14: Variation of round trip efficiency for different charging and discharging power scenarios.

7

Conclusions and Recommendations

7.1. Conclusions

The main objective of this work was to develop meanline models for centrifugal compressors and radial inflow turbines and analyse their application within a PTES system.

For both the compressor and turbine meanline models, a generalised methodology was presented for design and off-design performance modes. At each station, flowcharts were used to outline the update procedures to solve for the thermodynamic state at the respective station exits. The accuracy of the meanline model significantly depends on the loss models employed. In this work, loss model combinations and relations were identified and used from recent literature. These relations can also be substituted for alternate relations by simply switching them out in the model. Furthermore, the use of pressure-based loss models can also be made by adjusting loss update steps.

In the performance mode, using the selected loss models, a fair agreement was found between the meanline model predictions and that of the experimental cases from open literature. Using the same performance modelling approach, a design procedure is presented based on guidelines from the literature. As shown from these validation cases, tuning parameters were used to obtain a suitable match with the experimental results. Most of the loss models developed in literature are semi-empirical in nature and were tuned with turbomachines of their time. These were often lower pressure ratio machines operating on ideal fluid like air [31]. Hence as these loss models are semi-empirical, insights from higher-fidelity models or close experimental cases would be needed to improve trust in these models to carry out design and performance studies.

For the PTES model, the design methodology proposed by Radi [2] was employed to design a conceptual 100 kW scale system. Given the importance of flexibility in grid-scale energy storage technologies, modifications were made to the model for off-design conditions. Sensitivity analyses were then done on the PTES system to show the response of the system to varied turbomachinery performances. Compressor and turbine systems were designed for a 100 kW PTES system, and their performance charts were used to understand the off-design PTES response. For the charging cycle, it was concluded that operating at the design point led to the best COP and operating at higher mass flow rates would result in a trade-off in COP. For the discharging cycle, operating at lower mass flow rates than the design point leads to decreased heat engine efficiency, which means operating at the design point is again optimal. However, it must be stressed that one of the model assumptions was that no flow deviation takes place from the blade angle, which does not hold at high Mach numbers. While the general trend would remain the same, the turbine model accuracy is low in this regime.

Overall these response figures could potentially be used as rough guidelines for decision-making on what operating point to use based on various power demand and supply scenarios over suitable timeframes.

In summary, using the methodology and insights presented in the work, preliminary estimates for a PTES system design, turbomachinery sizing and off-design performance charts can be generated quickly in the order of a few minutes. Hence multiple scenarios can be tested by structuring suitable optimisation problems before moving on to analyses from higher fidelity models.

7.2. Recommendations

The present work demonstrates a framework for making meanline models for a centrifugal compressor and radial inflow turbine and using them to understand the off-design performance for a 100 kW scale PTES system. In order to improve the accuracy and understanding of the system, the following recommendations are suggested for carrying out future work.

7.2.1. Compressor model

- As mentioned in previous chapters, tuning the loss models used in this thesis would need insight from higher fidelity models such as CFD or experimental data.
- Regarding the assumptions of fixed geometry, one could apply realistic clearances and roughness based on manufacturing limitations. Furthermore, blade thickness adjustments might be necessary to fulfil strength requirements.
- In this study, it was assumed that losses do not occur beyond the vaneless diffuser stage. Thus, further assessments related to the sizing and associated losses of the volute and return channels could be conducted.
- A study optimising the variables in the compressor design vector could be undertaken. The most straightforward optimisation objective could be the compressor's efficiency. As highlighted in previous literature review sections, optimising the pressure ratio split benefits subsequent compression stages [84]. Similarly, optimising the compressor's operating range can be pursued, as demonstrated in [38].

7.2.2. Turbine model

- Similar to the compressor case, the loss models used for the meanline models could be reviewed.
- The volute considered is not this work and could be added in the future.
- More realistic values for the blade thickness and clearances can be chosen.
- An optimisation study can be done for the variables present in the design vector.
- For each operating point, a stator blade angle exists that minimises the loss. Hence, an optimisation for the blade angle using the performance vector can be done to improve efficiencies at off-design conditions [75].

7.2.3. PTES Model

- The framework by Radi [2] could be used to choose the optimal fluids, storage temperatures, and storage sizes for the PTES model.

- To design the PTES models, guess efficiencies were made for the compressors and turbines. In the present study, the efficiencies resulting from the meanline designs varied from this initial assumption. Hence, integrating the compressor and turbine models as shown by Radi [2] could be done iteratively to converge on a consistent PTES design.
- Equipment sizing and models of the remaining equipment, such as heat exchangers, pumps, valves, etc., could be developed to model the pressure losses in the equipment and also give an idea of the static pressures at the turbine exit and aid in the development of a more accurate PTES system model.
- The present PTES system is based on a steady-state model for the design condition. For the off-design scenario, it is assumed that a sufficient timescale passes over which the system stabilises to the new operating point. A dynamic model could be developed for more insight into the transient response of the PTES system.

References

[1] *Renewables Data Explorer – Data Tools - IEA*. URL: `https://www.iea.org/data-and-statistics/data-tools/renewables-data-explorer`.

[2] Ali Al Radi. “Small Scale Pumped Thermal Energy Storage Modeling and Optimization”. In: (2023).

[3] *The Paris Agreement | UNFCCC*. URL: `https://unfccc.int/process-and-meetings/the-paris-agreement`.

[4] *Emissions – Global Energy and CO2 Status Report 2019 – Analysis - IEA*. URL: `https://www.iea.org/reports/global-energy-co2-status-report-2019/emissions`.

[5] Said Attia al Hagrey, Daniel Köhn, and Wolfgang Rabbel. “Geophysical assessments of renewable gas energy compressed in geologic pore storage reservoirs”. In: *SpringerPlus* 3 (1 May 2014), pp. 1–16. URL: `https://springerplus.springeropen.com/articles/10.1186/2193-1801-3-267`.

[6] *Grid-Scale Storage – Analysis - IEA*. URL: `https://www.iea.org/reports/grid-scale-storage`.

[7] Thomas Bowen et al. *USAID GRID-SCALE ENERGY STORAGE TECHNOLOGIES PRIMER*. URL: `www.nrel.gov/publications.`.

[8] Pau Farres Antunez. “Modelling and development of thermo-mechanical energy storage”. PhD thesis. Sept. 2018. DOI: `10.17863/CAM.38056`. URL: `https://www.repository.cam.ac.uk/handle/1810/290867`.

[9] W.D. Steinmann. “The CHEST (Compressed Heat Energy STorage) concept for facility scale thermo mechanical energy storage”. In: *Energy* 69 (2014), pp. 543–552. DOI: `https://doi.org/10.1016/j.energy.2014.03.049`.

[10] DIVYANSH GAUTAM. *Pumped Thermal Energy Storage: Thermodynamic Modelling And Optimization Of Waste Heat Integrated Rankine PTES System*. 2022. URL: `https://repository.tudelft.nl/islandora/object/uuid%5C%3Ab6f478c3-0335-4c48-91ff-616263c7617d`.

[11] Mehmet Mercangöz et al. “Electrothermal energy storage with transcritical CO2 cycles”. In: *Energy* 45 (1 2012), pp. 407–415. DOI: `10.1016/J.ENERGY.2012.03.013`.

[12] Antoine Koen, Pau Farres Antunez, and Alexander White. “A study of working fluids for transcritical pumped thermal energy storage cycles”. In: *2019 Offshore Energy and Storage Summit (OSES)*. IEEE. 2019, pp. 1–7.

[13] Olivier Dumont et al. “Carnot battery technology: A state-of-the-art review”. In: *Journal of Energy Storage* 32 (2020), p. 101756. DOI: `https://doi.org/10.1016/j.est.2020.101756`.

[14] Joshua McTigue. “Analysis and optimisation of thermal energy storage”. In: (Nov. 2016). DOI: `10.17863/CAM.7084`.

[15] Ting Liang et al. “Key components for Carnot Battery: Technology review, technical barriers and selection criteria”. In: *Renewable and Sustainable Energy Reviews* 163 (2022), p. 112478. DOI: `https://doi.org/10.1016/j.rser.2022.112478`.

[16] Max Albert et al. “Operation and performance of Brayton Pumped Thermal Energy Storage with additional latent storage”. In: *Applied Energy* 312 (2022), p. 118700. DOI: `https://doi.org/10.1016/j.apenergy.2022.118700`.

[17] Joshua Mctigue et al. “Pumped Thermal Electricity Storage with Supercritical CO 2 Cycles and Solar Heat Input Preprint”. In: (2019). URL: `www.nrel.gov/publications.`.

[18] Guido Francesco Frate, Lorenzo Ferrari, and Umberto Desideri. “Techno-Economic Comparison of Brayton Pumped Thermal Electricity Storage (PTES) Systems Based on Solid and Liquid Sensible Heat Storage”. In: *Energies 2022, Vol. 15, Page 9595* 15 (24 Dec. 2022), p. 9595. DOI: `10.3390/EN15249595`.

[19] Andreas V Olympios et al. “Progress and prospects of thermo-mechanical energy storage—a critical review”. In: *Progress in Energy* 3.2 (2021), p. 022001.

[20] Henning Jockenhöfer, Wolf-Dieter Steinmann, and Dan Bauer. “Detailed numerical investigation of a pumped thermal energy storage with low temperature heat integration”. In: *Energy* 145 (2018), pp. 665–676. DOI: `https://doi.org/10.1016/j.energy.2017.12.087`.

[21] Fuhaid Alshammari, Muhammad Usman, and Apostolos Pesyridis. “Expanders for Organic Rankine Cycle Technology”. In: *Organic Rankine Cycle Technology for Heat Recovery*. Ed. by Enhua Wang. Rijeka: IntechOpen, 2018. Chap. 3. DOI: `10.5772/intechopen.78720`.

[22] Sydney Lawrence Dixon and Cesare Hall. *Fluid mechanics and thermodynamics of turbomachinery*. Butterworth-Heinemann, 2013.

[23] Marco Gambini and Michela Vellini. *Turbomachinery: Fundamentals, Selection and Preliminary Design*. Springer Nature, 2020.

[24] O. E. Balje´. “A Study on Design Criteria and Matching of Turbomachines: Part A—Similarity Relations and Design Criteria of Turbines”. In: *Journal of Engineering for Power* 84.1 (Jan. 1962), pp. 83–102. DOI: `10.1115/1.3673386`.

[25] O. E. Balje´. “A Study on Design Criteria and Matching of Turbomachines: Part B—Compressor and Pump Performance and Matching of Turbocomponents”. In: *Journal of Engineering for Power* 84.1 (Jan. 1962), pp. 103–114. DOI: `10.1115/1.3673350`.

[26] Michael Casey, Christof Zwyssig, and Chris Robinson. “The Cordier Line for Mixed Flow Compressors”. In: Oct. 2010. DOI: `10.1115/GT2010-22549`.

[27] OE Balje. “Turbomachines: A guide to design, selection, and theory(Book)”. In: *New York, Wiley-Interscience, 1981. 521 p* (1981).

[28] Meherwan P Boyce. *Gas turbine engineering handbook*. Elsevier, 2011.

[29] Erik Dick and Dick. *Fundamentals of turbomachines*. Vol. 109. Springer, 2015.

[30] *Radial Turbine Aerodynamics*. URL: `http://www-g.eng.cam.ac.uk/whittle/current-research/hph/radial-otl/radial-otl.html`.

[31] Andrea Meroni et al. “A methodology for the preliminary design and performance prediction of high-pressure ratio radial-inflow turbines”. In: *Energy* 164 (2018), pp. 1062–1078. DOI: `https://doi.org/10.1016/j.energy.2018.09.045`.

[32] Ennio Macchi and Marco Astolfi. *Organic rankine cycle (ORC) power systems: technologies and applications*. Woodhead Publishing, 2016.

[33] Alexander White, Geoff Parks, and Christos N. Markides. “Thermodynamic analysis of pumped thermal electricity storage”. In: *Applied Thermal Engineering* 53.2 (2013). Includes Special Issue: PRO-TEM Special Issue, pp. 291–298. DOI: `https://doi.org/10.1016/j.applthermaleng.2012.03.030`.

[34] Guido Francesco Frate, Marco Antonelli, and Umberto Desideri. “A novel Pumped Thermal Electricity Storage (PTES) system with thermal integration”. In: *Applied Thermal Engineering* 121 (2017), pp. 1051–1058. DOI: `https://doi.org/10.1016/j.applthermaleng.2017.04.127`.

[35] Jorge Gonzalez-Gonzalez. “Modelling Axial Turbomachinery for Compressed Air Energy Storage”. In: (Feb. 2018). URL: `https://uwspace.uwaterloo.ca/handle/10012/13032`.

[36] PP FLETCHER Walsh. *P.[Gas Turbine Performance]*. 2004.

[37] David Japikse. “Centrifugal compressor design and performance(Book)”. In: *Wilder, VT: Concepts ETI, Inc, 1996.* (1996).

[38] Andrea Giuffre, Piero Colonna, and Matteo Pini. “The Effect of Size and Working Fluid on the Multi-Objective Design of High-Speed Centrifugal Compressors”. In: *International Journal of Refrigeration* 143 (2022), pp. 43–56. DOI: `https://doi.org/10.1016/j.ijrefrig.2022.06.023`.

[39] Benjamin Monje. “Design of supercritical carbon dioxide centrifugal compressors”. PhD thesis. June 2014.

[40] Carlo M. De Servi et al. “Design Method and Performance Prediction for Radial-Inflow Turbines of High-Temperature Mini-Organic Rankine Cycle Power Systems”. In: *Journal of Engineering for Gas Turbines and Power* 141.9 (Aug. 2019). 091021. DOI: `10.1115/1.4043973`.

[41] Ian H. Bell et al. “Pure and Pseudo-pure Fluid Thermophysical Property Evaluation and the Open-Source Thermophysical Property Library CoolProp”. In: *Industrial & Engineering Chemistry Research* 53.6 (2014). PMID: 24623957, pp. 2498–2508. DOI: `10.1021/ie4033999`.

[42] David Japikse and Nicholas C Baines. “Introduction to turbomachinery(Book)”. In: *Norwich, VT/Oxford, United Kingdom: Concepts ETI, Inc./Oxford University Press, 1994.* (1994).

[43] Michael Casey and Chris Robinson. *Radial Flow Turbocompressors*. Cambridge University Press, 2021.

[44] J. D. Stanitz. “Some Theoretical Aerodynamic Investigations of Impellers in Radial- and Mixed-Flow Centrifugal Compressors”. In: *Transactions of the American Society of Mechanical Engineers* 74.4 (July 2022), pp. 473–497. DOI: `10.1115/1.4015817`.

[45] F. J. Wiesner. “A Review of Slip Factors for Centrifugal Impellers”. In: *Journal of Engineering for Power* 89.4 (Oct. 1967), pp. 558–566. DOI: `10.1115/1.3616734`.

[46] H Ronald. “Centrifugal compressors: A strategy for aerodynamic design and analysis”. In: *American Society of Mechanical Engineers Press: New York, NY, USA* (2000).

[47] Rene Van den Braembussche. *Design and analysis of centrifugal compressors*. John Wiley & Sons, 2019.

[48] Yasutoshi Senoo and Yoshifumi Kinoshita. “Influence of Inlet Flow Conditions and Geometries of Centrifugal Vaneless Diffusers on Critical Flow Angle for Reverse Flow”. In: *Journal of Fluids Engineering* 99.1 (Mar. 1977), pp. 98–102. DOI: `10.1115/1.3448577`.

[49] A Whitfield and N C Baines. “Design of radial turbomachines”. In: (Jan. 1990). URL: `https://www.osti.gov/biblio/6550042`.

[50] J. Schiffmann and D. Favrat. “Experimental investigation of a direct driven radial compressor for domestic heat pumps”. In: *International Journal of Refrigeration* 32.8 (2009), pp. 1918–1928. DOI: `https://doi.org/10.1016/j.ijrefrig.2009.07.006`.

[51] J. Schiffmann and D. Favrat. “Design, experimental investigation and multi-objective optimization of a small-scale radial compressor for heat pump applications”. In: *Energy* 35.1 (2010), pp. 436–450. DOI: `https://doi.org/10.1016/j.energy.2009.10.010`.

[52] Andrea Meroni et al. “Design of centrifugal compressors for heat pump systems”. In: *Applied Energy* 232 (2018), pp. 139–156. DOI: `https://doi.org/10.1016/j.apenergy.2018.09.210`.

[53] D. Eckardt. “Instantaneous Measurements in the Jet-Wake Discharge Flow of a Centrifugal Compressor Impeller”. In: *Journal of Engineering for Power* 97.3 (July 1975), pp. 337–345. DOI: `10.1115/1.3445999`.

[54] D. Eckardt. “Detailed Flow Investigations Within a High-Speed Centrifugal Compressor Impeller”. In: *Journal of Fluids Engineering* 98.3 (Sept. 1976), pp. 390–399. DOI: `10.1115/1.3448334`.

[55] D. Eckardt. *Investigation of the jet-wake flow of a highly loaded centrifugal compressor impeller*. Tech. rep. 1978. URL: `https://ntrs.nasa.gov/citations/19780008108`.

[56] H W Oh, E S Yoon, and M K Chung. “An optimum set of loss models for performance prediction of centrifugal compressors”. In: *Proceedings of the Institution of Mechanical Engineers, Part A: Journal of Power and Energy* 211.4 (1997), pp. 331–338. DOI: `10.1243/0957650971537231`.

[57] Chaowei Zhang et al. “A method to select loss correlations for centrifugal compressor performance prediction”. In: *Aerospace Science and Technology* 93 (2019), p. 105335. ISSN: 1270-9638. DOI: `https://doi.org/10.1016/j.ast.2019.105335`.

[58] Stella Spazzoli. “Supercritical CO2 Power Cycle for Solar Applications”. Oct. 2014.

[59] BW Botha and A Moolman. “Determining the impact of the different losses on centrifugal compressor design”. In: *R&D J* 21.3 (2005), pp. 1–9.

[60] Sergio Sanz Solaesa. “Analytical prediction of turbocharger compressor performance: A comparison of loss models with numerical data”. Industriales, 2016.

[61] Michael R Galvas. *FORTRAN program for predicting off-design performance of centrifugal compressors*. 1973.

[62] Simone Parisi. “Modeling and simulation of a centrifugal compressor for automotive fuel cell applications”. In: (2020).

[63] W Jansen. “A method for calculating the flow in a centrifugal impeller when entropy gradient are present”. In: *Inst. Mech. Eng. Internal Aerodynamics* (1970).

[64] JE Coppage et al. *Study of supersonic radial compressors for refrigeration and pressurization systems*. Wright Air Development Center, 1956.

[65] J. P. Johnston and Jr. Dean R. C. “Losses in Vaneless Diffusers of Centrifugal Compressors and Pumps: Analysis, Experiment, and Design”. In: *Journal of Engineering for Power* 88.1 (Jan. 1966), pp. 49–60. DOI: `10.1115/1.3678477`.

[66] J. W. Daily and R. E. Nece. “Chamber Dimension Effects on Induced Flow and Frictional Resistance of Enclosed Rotating Disks”. In: *Journal of Basic Engineering* 82.1 (Mar. 1960), pp. 217–230. ISSN: 0021-9223. DOI: `10.1115/1.3662532`.

[67] John D Stanitz. *One-dimensional compressible flow in vaneless diffusers of radial-and mixed-flow centrifugal compressors, including effects of friction, heat transfer and area change*. Tech. rep. 1952.

[68] Roberto Agromayor, Bernhard Müller, and Lars O. Nord. “One-Dimensional Annular Diffuser Model for Preliminary Turbomachinery Design”. In: *International Journal of Turbomachinery, Propulsion and Power* 4.3 (2019). DOI: `10.3390/ijtpp4030031`.

[69] *MATLAB - MathWorks*. URL: `https://nl.mathworks.com/products/matlab.html`.

[70] Cheng Xu and Ryoichi S Amano. “Empirical Design Considerations for Industrial Centrifugal Compressors”. In: *International Journal of Rotating Machinery* 2012 (2012), p. 15. DOI: `10.1155/2012/184061`.

[71] G Persico and M Pini. “Fluid dynamic design of Organic Rankine Cycle turbines”. In: *Organic Rankine Cycle (ORC) Power Systems*. Elsevier, 2017, pp. 253–297.

[72] Sebastian Bahamonde et al. “Method for the Preliminary Fluid Dynamic Design of High-Temperature Mini-Organic Rankine Cycle Turbines”. In: *Journal of Engineering for Gas Turbines and Power* 139.8 (Mar. 2017). DOI: `10.1115/1.4035841`.

[73] Luca Da Lio, Giovanni Manente, and Andrea Lazzaretto. “A mean-line model to predict the design efficiency of radial inflow turbines in organic Rankine cycle (ORC) systems”. In: *Applied Energy* 205 (2017), pp. 187–209. DOI: `https://doi.org/10.1016/j.apenergy.2017.07.120`.

[74] Ronald H Aungier. “Turbine aerodynamics”. In: *ASME, New York* (2006).

[75] Sebastian Schuster, Christos N. Markides, and Alexander J. White. “Design and off-design optimisation of an organic Rankine cycle (ORC) system with an integrated radial turbine model”. In: *Applied Thermal Engineering* 174 (2020), p. 115192. DOI: `https://doi.org/10.1016/j.applthermaleng.2020.115192`.

[76] *Find minimum of constrained nonlinear multivariable function - MATLAB fmincon - MathWorks Benelux*. URL: `https://nl.mathworks.com/help/optim/ug/fmincon.html`.

[77] Marco Manfredi et al. “A Reduced-Order Model for the Preliminary Design of Small-Scale Radial Inflow Turbines”. In: June 2021. DOI: `10.1115/GT2021-59444`.

[78] H. Moustapha et al. *Axial and Radial Turbines*. Concepts NREC., 2003. ISBN: 9780933283183. URL: `https://books.google.nl/books?id=O%5C_X3zQEACAAJ`.

[79] Charles A Wasserbauer and Arthur J Glassman. *FORTRAN program for predicting off-design performance of radial-inflow turbines*. Tech. rep. 1975.

[80] Arthur J Glassman. *Enhanced analysis and users manual for radial-inflow turbine conceptual design code RTD*. Tech. rep. NASA, 1995.

[81] NC Baines. “A meanline prediction method for radial turbine efficiency”. In: (1998).

[82] Colin Rodgers. “Mainline performance prediction for radial inflow turbines”. In: *Von Karman Inst. for Fluid Dynamics, Small High Pressure Ratio Turbines 29 p(SEE N 88-14364 06-37)* (1987).

[83] *Experimental Performance and Analysis of 15.04-Centimeter-Tip-Diameter, Radial-Inflow Turbine with Work Factor of 1.126 and Thick Blading.* URL: `https://apps.dtic.mil/sti/citations/ADA091120`.

[84] Andrea Giuffre’, Piero Colonna, and Matteo Pini. “Design Optimization of a High-Speed Twin-Stage Compressor for Next-Gen Aircraft Environmental Control System”. In: *Journal of Engineering for Gas Turbines and Power* 145.3 (Dec. 2022), p. 031017. ISSN: 0742-4795. DOI: `10.1115/1.4056022`.

A

Data used for validation cases

A.1. Compressor Validation

Table A.1: Data of centrifugal compressors for validation cases.

Variable	Units	Eckardt O [53, 54, 55]	Schiffmann [38, 50]
Fluid	-	Air	R134a
T_{01}	K	288.15	283.15
P_{01}	bar	1.01	1.65
N	krpm	10-18	150-210
r_{1s}	mm	140	5.6
r_{1h}	mm	45	1
r_2	mm	200	10
r_3	mm	338	16.5
b_2	mm	26.7	1.2
b_3	mm	13.6	1
L_a	mm	130	7.7
$N_{b,full}$	-	20	9
$N_{b,split}$	-	0	9
β_{1s}	deg	-63	-60
β_{1h}	deg	-33	-20.5
β_{2b}	deg	0	-45
k_s	mm	0.01	0.01
$t_{b1,le}$	mm	2.5	0.2
$t_{b1,te}$	mm	1.25	0.2
ϵ_t	mm	0.372	0.05
ϵ_b	mm	0.372	0.2

A.2. Turbine Validation

Table A.2: Turbine data used for validation cases

Variable	Unit	McLallin et al. [83]
Fluid	-	Air
T_{01}	K	322.2
P_{01}	Pa	137900
N	rpm	9437-34602
b_1	m	0.0109
b_3	m	0.008
r_1	m	0.097
r_3	m	0.084
$N_{b,stator}$	-	29
t_{b3}	m	0.001
α_{3b}	deg	76
b_4	m	0.008
r_4	m	0.075
r_{6s}	m	0.047
r_{6h}	m	0.023
β_{4b}	deg	0
β_{6b}	deg	-58
$N_{b,rotor}$	-	12
t_6	m	0.004
L_a	m	0.04572
ϵ_a	m	0.0003
ϵ_r	m	0.0003
ϵ_b	m	0.0003

B

Steps to derive a relation for the compressor rotor blade angle

From the velocity triangle shown in figure 4.3, the meridional velocity at the impeller outlet is given as:

$$c_{2m} = \frac{c_{2\theta}}{\tan\alpha_2}. \tag{B.1}$$

Also, the work coefficient can be written as:

$$\psi = \frac{\Delta h}{u_2^2} = \frac{c_{2\theta}u_2}{u_2^2} = \frac{c_{2\theta}}{u_2}, \tag{B.2}$$

which implies

$$c_{2\theta} = u_2\psi. \tag{B.3}$$

Now, from the outlet velocity triangle, the relative flow angle is given as:

$$\tan\beta_2 = \frac{u_2 - c_{2\theta}}{c_{2m}}. \tag{B.4}$$

Substituting equations (B.1) and (B.3), β_2 can be written as

$$\tan\beta_2 = \frac{(u_2 - u_2\psi)\tan\alpha_2}{u_2\psi} = \frac{1-\psi}{\psi}\tan\alpha_2. \tag{B.5}$$

As $\psi_{is} = \eta_{tt}\psi$, equation (B.5) now becomes

$$\tan\beta_2 = \frac{(\eta_{tt} - \psi_{is})}{\psi_{is}}\tan\alpha_2 = \left(\frac{\eta_{tt}}{\psi_{is}} - 1\right)\tan\alpha_2. \tag{B.6}$$

From Wiesner's relation for slip [45],

$$\sigma = 1 - \frac{c_{2\theta,\infty} - c_{2\theta}}{c_{2m}} = 1 - \frac{\sqrt{\cos\beta_{2b}}}{N_b^{0.7}} \tag{B.7}$$

Rearranging this, an expression for $c_{2\theta,\infty}$ can be made as

$$c_{2\theta,\infty} = c_{2\theta} + \frac{u_2\sqrt{\cos\beta_{2b}}}{N_b^{0.7}}. \tag{B.8}$$

Now, taking the ratios of the relative flow angle and the rotor blade angle,

$$\frac{\tan\beta_{2b}}{\tan\beta_2} = \frac{u_2 - c_{2\theta\infty}}{u_2 - c_{2\theta}}. \tag{B.9}$$

Substituting equations (B.3) and (B.8), and rearranging, equation (B.9) becomes

$$\frac{\tan\beta_{2b}}{\tan\beta_2} = 1 - \frac{\sqrt{cos\beta_{2b}}}{(1-\frac{\psi}{\eta_{tt}})N_b^{0.7}}. \tag{B.10}$$

Finally, substituting equation (B.6), an implicit relation for the rotor blade angle is formulated as a function of the design variables.

$$\tan\beta_{2b} = \tan\alpha_2\left(\frac{\eta_{tt}}{\psi_{is}} - 1\right)\left(1 - \frac{\sqrt{cos\beta_{2b}}}{N_b^{0.7}\left(1-\frac{\psi_{is}}{\eta_{tt}}\right)}\right) \tag{B.11}$$

Using the relation by Xu et al. [70] for N_b, the blade angle can be plotted as a function of the design variables for different efficiency levels as shown in figure B.1.

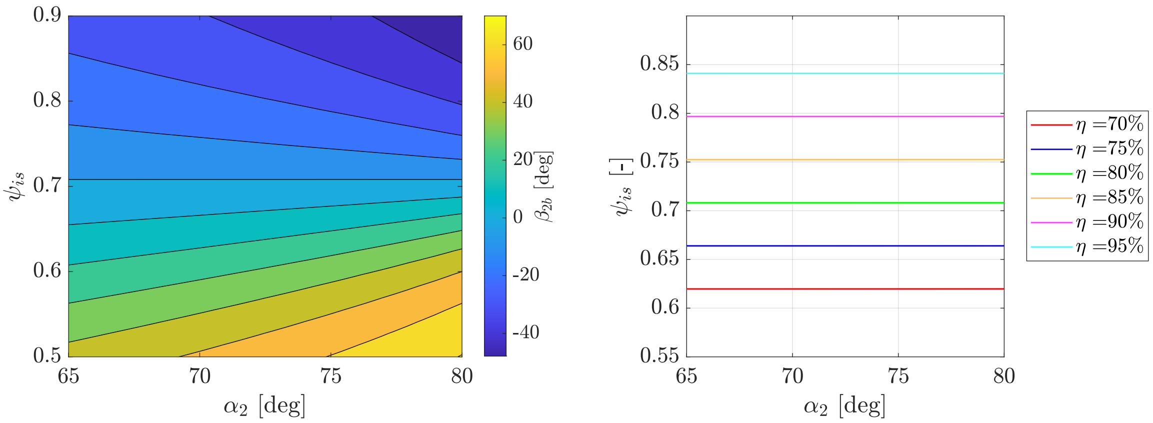

(a) Variation of β_{2b} for η_{tt}=80% and N_b=22.

(b) Contours of β_{2b}=0 for N_b =22 for varied η_{tt}.

Figure B.1: Parametric analysis rotor blade angle according to equation B.11.

C

Discrepancies in literature

Over the course of this thesis, a few inconsistencies were found in the literature. These most probably are errors are unintentional and could have crept over the course of editing. While it's not practical to scrutinize every piece of literature cited in this thesis, the primary works referenced are examined for discrepancies.

The following list details some of these inconsistencies that I came across. I do apologise if there is an error in my judgment, and I hope that future readers will find this list beneficial.

C.1. Compressor meanline model

- Slip factor relation: The slip factor used in Gambini's textbook [23] is misapplied. On reaching out to the author, the same was confirmed. While the relation of Wiesner [45] used is correct, the definition of the slip velocity triangle, and hence slip was inconsistent with the slip factor relation. Like most confusions in engineering, this crept up because of the European and American definitions of slip used in literature, as shown in [42].
- Skin friction loss: In Gambini's textbook [23], the relation for the hydraulic length of the skin friction loss, the averaging of the mean rotor blade angle is incorrectly used in comparison to the relation by Jansen [63].
- The geometry data and inlet conditions of the Schiffmann impeller present in Meroni's work [52], is incorrect, and gave large deviations when attempting to validate the experimental case. These were probably typographical errors in the work, as a good fit was found during their validation case. The work by Giuffre [38] presents the correct set of inputs for the model, as they were obtained from the original author.

C.2. Turbine meanline model

- In the work by Meroni [31], the validation of the Mclallin turbine, the speed cases were incorrectly labelled as 50%, 70% and 100%. According to the original results by Mclallin [83] these should have instead been labelled as 100%, 90% and 50%.
- In the work of Gambini [23], for the passage loss equation, the hydraulic length is used in place of the rotor chord.